Opto-Electronic Advances

Review

2022, Vol. 5, No. 4

DOI: 10.29026/oea.2022.200098

Graphene-empowered dynamic metasurfaces and metadevices

Chao Zeng[1], Hua Lu[1], Dong Mao[1], Yueqing Du[1], He Hua[1], Wei Zhao[2]* and Jianlin Zhao[1]*

Metasurfaces, with extremely exotic capabilities to manipulate electromagnetic (EM) waves, have derived a plethora of advanced metadevices with intriguing functionalities. Tremendous endeavors have been mainly devoted to the static metasurfaces and metadevices, where the functionalities cannot be actively tuned *in situ* post-fabrication. Due to the intrinsic advantage of active tunability by external stimulus, graphene has been successively demonstrated as a favorable candidate to empower metasurfaces with remarkably dynamic tunability, and their recent advances are propelling the EM wave manipulations to a new height: from static to dynamic. Here, we review the recent progress on dynamic metasurfaces and metadevices enabled by graphene with the focus on electrically-controlled dynamic manipulation of the EM waves covering the mid-infrared, terahertz, and microwave regimes. The fundamentals of graphene, including basic material properties and plasmons, are first discussed. Then, graphene-empowered dynamic metasurfaces and metadevices are divided into two categories, i.e., metasurfaces with building blocks of structured graphene and hybrid metasurfaces integrated with graphene, and their recent advances in dynamic spectrum manipulation, wavefront shaping, polarization control, and frequency conversion in near/far fields and global/local ways are elaborated. In the end, we summarize the progress, outline the remaining challenges, and prospect the potential future developments.

Keywords: metasurface; dynamic metasurface; graphene; graphene plasmons; light field manipulation; electromagnetic wave manipulation

Zeng C, Lu H, Mao D, Du YQ, Hua H et al. Graphene-empowered dynamic metasurfaces and metadevices. *Opto-Electron Adv* **5**, 200098 (2022).

Introduction

Metasurfaces, artificial subwavelength structured interfaces, exhibit unprecedented capabilities to manipulate electromagnetic (EM) waves ranging from visible to terahertz (THz) and microwave frequencies[1–8]. By precisely managing the geometric size, orientation, and arrangement of each metaatom in metasurfaces, one can control the amplitude, phase, polarization, and/or frequency of EM waves on demand[9–14]. In the past decade, this fascinating area has undergone rapid developments, and a plethora of advanced metadevices with outstanding functionalities have been exploited including diffraction-limited focusing[15–21], holography[22–26], structured light generation[27–29], orbital-angular momentum multiplexing/demultiplexing[30,31], and dispersion engineering[32–35]. It is noteworthy that besides the intriguing functionalities, the natural instinct to miniaturize traditional devices and systems is the ultimate motive force to the development of metasurfaces and metadevices in terms of engineering and industrial applications[36]. In pace with increasingly

[1]MOE Key Laboratory of Material Physics and Chemistry under Extraordinary Conditions, and Shaanxi Key Laboratory of Optical Information Technology, School of Physical Science and Technology, Northwestern Polytechnical University, Xi'an 710129, China; [2]State Key Laboratory of Transient Optics and Photonics, Xi'an Institute of Optics and Precision Mechanics, Chinese Academy of Sciences, Xi'an 710119, China.
*Correspondence: W Zhao, E-mail: weiz@opt.ac.cn; JL Zhao, E-mail: jlzhao@nwpu.edu.cn
Received: 26 December 2020; Accepted: 21 March 2021; Published online: 25 April 2022

powerful micro/nano-fabrication technologies[37–41], various functionalized metasurfaces have been integrated on fiber facets[42], and into semiconductor[43], solid-state[44] as well as fiber lasers[45], infusing new life and capabilities into the traditional nanodevices. Currently, multi-functional and multi-dimensional metasurfaces are arousing a period of revolution in both traditional and emerging application fields[46–48], such as integrated photonics[49,50], nonlinear optics[51,52], next-generation communications[53,54], artificial intelligences[55,56], and quantum technologies[57,58].

Due to the passive nature of building blocks in general made of metals and/or dielectrics, however, aforementioned metasurfaces and metadevices mainly work at static, which means their functionalities cannot be actively tuned *in situ* after fabrication. There is no doubt, such static feature leads to a fall-off in the functionality of dynamical manipulations and seriously impedes their application scenarios, where dynamic EM wave manipulations are highly desired[59–63], for example, varifocal lens[64], dynamic holography[65], and beam steering in LiDAR system[66]. Motivated by those significant requirements, scientists have struggled for years to improve the dynamical tunability of metasurfaces, and introducing active materials or components into the passive metasurfaces has been proposed as the first thought strategy. Up to now, various active materials and components such as transparent conducting oxides[67–69], phase-change materials[70–73], 2D materials (particularly graphene)[74–79], varactor diodes[80–83], elastic materials[84–86], and micro-electro-mechanical system[87–89], have been demonstrated theoretically and experimentally to empower the active tunability to metasurfaces and metadevices by applying external thermal, electrical, optical, and mechanical stimulus, giving rise to a new direction, i.e., dynamic (e.g. tunable, reconfigurable, programable, intelligent, and digital coding) metasurfaces and metadevices[90–96]. It should be noted that although previous researches provide a major source of inspiration for dynamic metasurfaces and metadevices, each type of active materials and components holds a set of unique characteristics, provides encouraging opportunities, and also suffers from different limitations as well as challenges. Several excellent review articles published in recent years have focused on this area to discuss the aforementioned issues[97–101]. However, a comprehensive review on graphene-based dynamic metasurfaces and metadevices is still absent, which are of equal and even more significance due to the extraordinary properties of graphene.

Recent years have witnessed the explosive developments of 2D materials-based electronics and photonics with increasing maturity of preparation and fabrication techniques[102–115]. Although the family of 2D materials goes from strength to strength, graphene is recognized all the time as one of the most powerful 2D materials due to its intrinsic advantages of active tunability by external stimulus (especially by electrical basis)[116], enhanced wave-matter interactions[117], ultrabroadband response[118], and CMOS-compatibility[113]. Currently, the combination of the two exciting research fields, i.e., 2D materials and metasurfaces, is propelling the metasurfaces and metadevices to new heights: multifunctionality together with tunability. Thereinto, graphene has been so far the most attractive candidate to exploit dynamic metasurfaces and metadevices with different mechanisms, configurations, and functionalities in the mid-infrared (MIR), THz, and microwave regimes, which can be categorized into two classes: metasurfaces with building blocks of structured graphene and hybrid metasurfaces integrated with graphene[74–79,119–127]. The former is called graphene plasmonic metasurfaces and the latter graphene-hybrid metasurfaces (as shown in Fig. 1). Considering the rapid advances of this overlapped field, this review is devoted to the dynamic metasurfaces and metadevices enabled by graphene with an emphasis primarily on electrically-controlled EM wave manipulations in the MIR, THz, and microwave regimes. In Section *Fundamentals of graphene*, the basic material properties of graphene and plasmons in graphene are introduced, and further the theoretical and numerical models of graphene plasmons are discussed in detail. Then, the state-of-the-art advancements in graphene plasmonic metasurfaces and graphene-hybrid metasurfaces for dynamic spectrum manipulation, wavefront shaping, polarization control, and frequency conversion in near/far fields and global/local ways are highlighted in Sections *Metasurfaces with building blocks of structured graphene* and *Hybrid metasurfaces integrated with graphene*. In the end, Section *Conclusion and outlook* summarizes the progresses, concludes the remaining challenges, and outlooks the potential future developments.

Fundamentals of graphene

In 2004, Novoselov and Geim et al. successfully prepared the single-layer graphene from highly oriented pyrolytic graphite by mechanical exfoliation and demon-

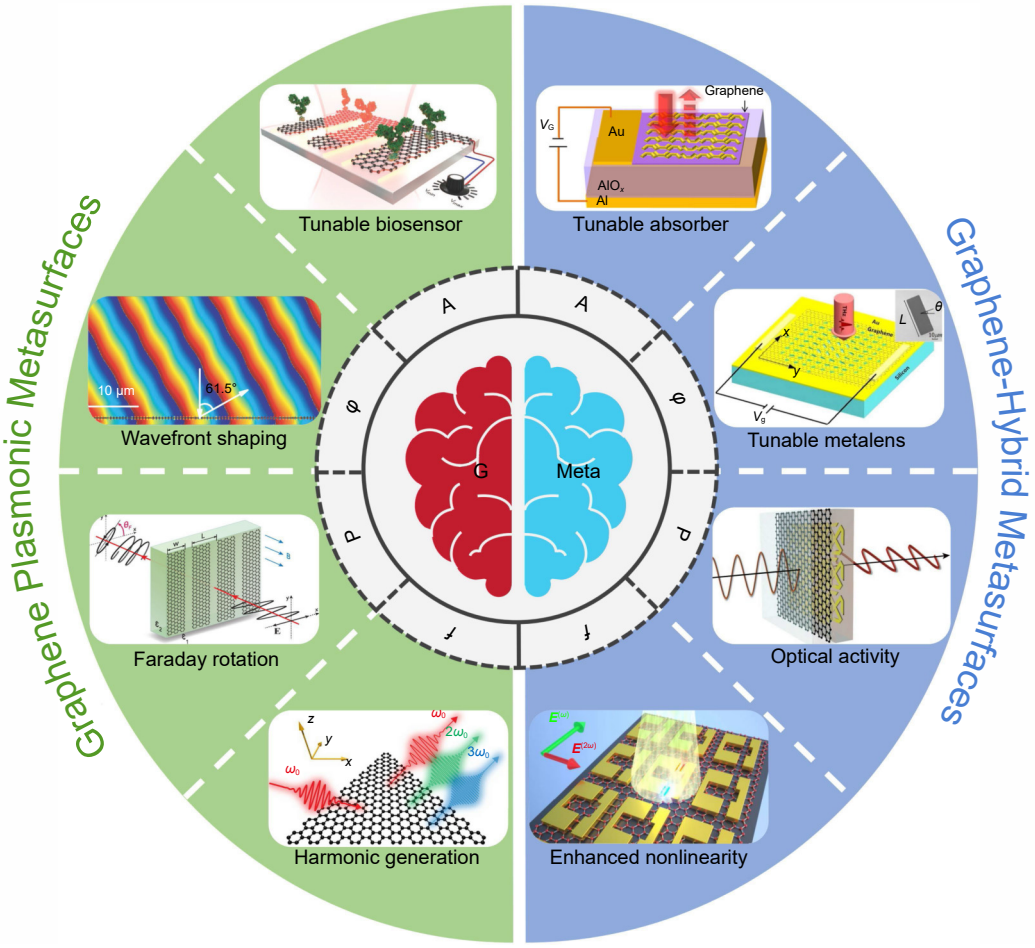

Fig. 1 | Overview of state-of-the-art selected functionalities of dynamic metasurfaces and metadevices empowered by graphene. According to the different operation mechanisms, graphene-empowered dynamic metasurfaces are here divided into two classes: graphene plasmonic metasurfaces and graphene-hybrid metasurfaces, each of which holds half the sky. The abbreviations of G and Meta represent graphene and metasurface, and the symbols of *A*, *φ*, *P*, and *f* stand for the amplitude, phase, polarization, and frequency of EM waves respectively.

strated a field-effect transistor using high-quality few-layer graphene, which lifted the curtain of research on 2D materials[128–131]. The Nobel Prize for Physics in 2010 publicized widely this powerful one-atomic-thick material and also the simple preparation method of mechanical exfoliation, providing the easy access to prepare high-quality graphene, which is now the most popular method, particularly in the photonics and optoelectronics. Since then, 2D materials with the structure and properties similar to graphene, such as black phosphorus (BP)[132–134] and transition metal dichalcogenides (TMDCs)[135–137], began to gather increasing attention of scientists in the multidisciplinary field, especially in the photonic and optoelectronic community due to their exceptional electrical and optical properties[108,138]. Although the family of 2D materials is rather plentiful, due to the easy preparation of remarkably high-quality graphene, flexibly electrical tunability, and CMOS-compatible with silicon photonics, graphene is still one of the most powerful 2D materials for developing high-performance nanodevices including metadevices, where the qualities of 2D materials are critically important, for instance, the mobility, conductivity, defect, size, and layer number[114,139,140]. In this Section, we centre upon graphene to discuss its basic material properties and plasmon mode, and provide the theoretical and numerical models of graphene plasmons. It should be noted that graphene in general represents the single-layer graphene throughout this review if there is no special description.

Basic material properties of graphene

It is well-known that due to its unique electronic structure, graphene has been hailed as a wonderful material with distinctive properties, which provide new solutions to integrated electronics and photonics with the compact footprint, remarkably electrical tunability,

broadband and high-speed operation.

(i) One-atomic-scale thickness. Graphene is a single-layer atomic crystal of hexagonally-arranged sp^2-hybridized carbon atoms with the lattice constant of ~0.142 nm[128]. As shown in Fig. 2(a), the thickness of single-layer graphene is one-atomic-scale with the value of ~0.334 nm theoretically and ~0.4 nm experimentally, and the continuous size of high-quality graphene sheet can be up to a macroscopic scale (~100 μm) by using micromechanical exfoliation, which is sufficient for most researches in photonics and optoelectronics[130,141]. For the purpose of integration with electronic and photonic platforms, the one-atomic-scale thickness as well as macroscopic-scale size of graphene make it more compatible with CMOS processing at the wafer scale.

(ii) Ultra-high intrinsic carrier mobility. The linear energy-momentum dispersion near the Dirac point renders electrons in graphene travelling at a constant velocity of 3×10^6 m/s (only 100 times smaller than the light speed, defined as the Fermi velocity), which means the carrier mobility can be ultra-high and thus graphene is an excellent conductor of electricity. It should be pointed out that the mobility can also remain high even when the carrier density is zero at the Dirac point, which is quietly different from semiconductors where carriers become immobile at low density. Although the environment (particular the substrate) significantly affects the mobility of graphene in practice, the experimentally measured mobility is still high enough, for example, ~4×10^4 $cm^2V^{-1}s^{-1}$ on SiO_2 substrate (Fig. 2(b))[142], ~1.4×10^5 $cm^2V^{-1}s^{-1}$ encapsulated within hexagonal boron nitride (*h*BN) layers[143], and ~2×10^5 $cm^2V^{-1}s^{-1}$ in suspended graphene (Fig. 2(c))[144]. This implies that graphene-based electronics and optoelectronics have the potential to operate at speed of a few hundred GHz and even to THz, for example, graphene-based modulators[145–147] and photodetectors[148–150].

(iii) Tunable and broadband responses. Due to the unique electronic band structure that conic-shaped conduction band and valence band meet at the Dirac point, the optical conductance of pristine graphene is frequency-independent and only determined by its fine-structure constant $\alpha=e^2/\hbar c\approx1/137$ (here e is the electron charge, $\hbar$ the reduced Planck's constant, and c the light speed in the vacuum), which directly results in a frequency-independent optical absorption $A=\pi\alpha\sim2.3\%$

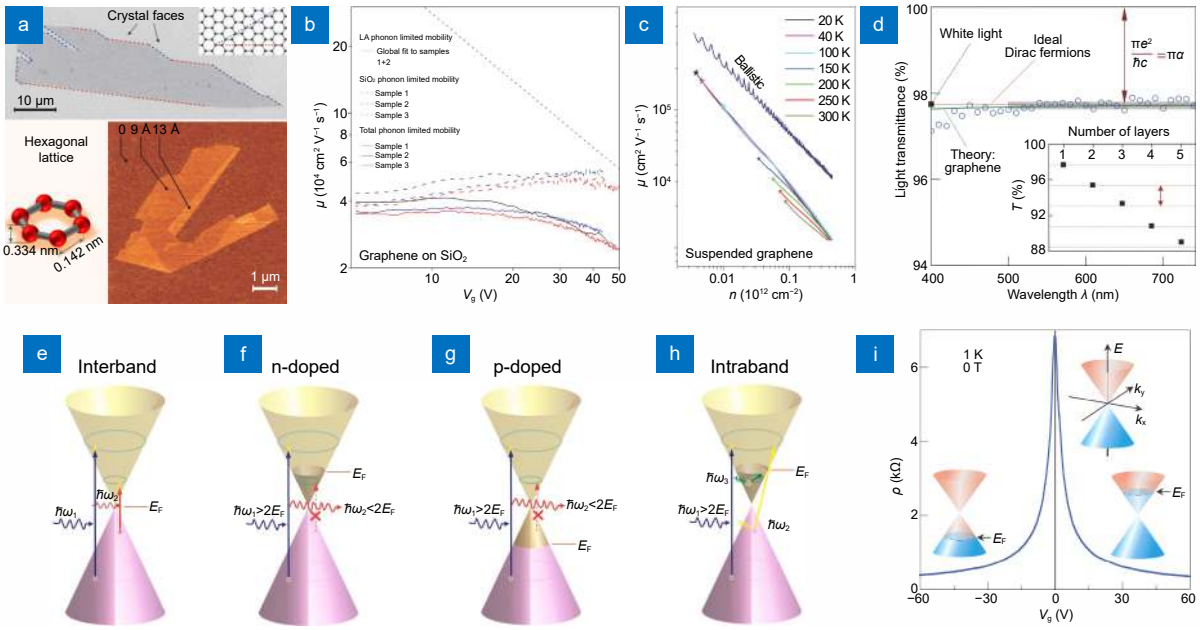

Fig. 2 | The basic material properties of graphene. (**a**) Micrographs of the scanning electron microscopy (upper panel) and atomic force microscopy (lower right panel), and also a schematic diagram of the 2D hexagonal lattice of graphene (lower left panel). Typical carrier mobility for (**b**) graphene on SiO_2 with gate-voltage dependence at room temperature and (**c**) suspended graphene depending on carrier density at the different temperatures. (**d**) Measured transmission spectrum of graphene in the visible range, where the inset is the transmittance as a function of the number of graphene layers. The band structures and its possible transition process for: (**e**) pristine or undoped, (**f**) n-doped, (**g**) p-doped graphene, and (**h**) plasmon absorption in n-doped graphene. (**i**) Dynamic resistivity ρ with gate voltage V_g applied on graphene, in which the insets show the corresponding position of the Fermi energy E_F with changing V_g. Figure reproduced with permission from: (a, i) ref.[130], © 2007 Springer Nature; (b) ref.[142], © 2008 Springer Nature; (c) ref.[144], © 2008 Springer Nature; (d) ref.[151], © 2008 AAAS; (e–h) ref.[118], © 2012 ACS.

for single-layer graphene and $A=N\pi\alpha$ for N-layer graphene, as shown in Fig. 2(d)[151]. In terms of an one-atomic-thick material, this universal optical absorption of 2.3% is strong enough in fact, which for example is ~50 times higher than the same-thickness GaAs[116]. For device applications, however, it is rather small when considering the insertion loss of 2.3%. Therefore, the enhancement of light absorption of graphene is a hot topic all the time[152–157]. Significantly, the optical absorption of graphene can be interpreted from the optical transition process using energy band structure shown in Fig. 2(e–i)[118,130]. Owing to the zero-band gap, there exist two competitive transition processes, *i.e.* intraband and interband transitions, and their relative contributions directly result in the selected absorption of waves with different energies. The interband transition only occurs for n/p-doped graphene when photon energy is larger than two times of Fermi energy ($\hbar\omega>2E_F$), while intraband transition always happens except for pristine or undoped graphene (E_F locates at the Dirac point). For high-energy photons (from visible to near-infrared (NIR)), the interband transition dominates the broadband absorption of ~2.3%; For low-energy photons at THz frequencies usually below $2E_F$ ($\hbar\omega<2E_F$), the interband transitions are forbidden and the absorption is mainly attributed to the intraband transition, which shows typical Drude feature corresponding to the plasmon absorption; For moderate-energy photons in the MIR regime, interband transition is forbidden and the possibility of intraband transition reaches the minimum due to the Pauli-blocking, indicating the minimal absorption loss (smaller than 2.3%)[158–160]. Those transition processes closely depend on the Fermi energy of graphene and the frequency of the incident wave, which therefore can be controlled through chemical doping or electrical gating to shift E_F and induce Pauli-blocking. In general, the condition that photon energy is less than optical phonon energy (0.20 eV) should be taken into account, otherwise the additional losses from electron-phonon coupling are nonnegligible[161]. Therefore, the minimal loss condition is concluded with $\hbar\omega<0.20$ eV ($\lambda>6.2$ μm) and $\hbar\omega<2E_F$. Figure 2(i) shows the gate dependence of graphene resistivity induced by the electric-field effect when a variable gate-voltage is applied. This dynamic tunability with simple electrical gating has been widely exploited to enable electrically-tunable nanophotonic devices, including dynamic metasurfaces and metadevices working at MIR and THz frequencies.

The EM response of graphene can be described and determined by its complex conductivity. From this perspective, here the origin of above-discussed dynamic response of graphene is enquired. The surface conductivity of graphene σ can be strictly expressed using the Kubo formula with intraband and interband contributions ($\sigma=\sigma_{intra}+\sigma_{inter}$)[162–164]. Under the random-phase approximation, it can be simplified as,

$$\sigma_{intra}=\frac{i2e^2k_BT}{\pi\hbar^2(\omega+i\tau^{-1})}\ln\left[2\cosh\left(\frac{E_F}{2k_BT}\right)\right], \tag{1a}$$

$$\sigma_{inter}=\frac{e^2}{4\hbar}\left[\frac{1}{2}+\frac{1}{\pi}\arctan\left(\frac{\hbar\omega-2E_F}{2k_BT}\right)-\frac{i}{2\pi}\ln\left(\frac{(\hbar\omega+2E_F)^2}{(\hbar\omega-2E_F)^2+4(k_BT)^2}\right)\right], \tag{1b}$$

where e is the electron charge, k_B is the Boltzmann constant, T is the temperature, $\hbar$ is the reduced Planck's constant, $\tau=\mu E_F/(ev_F^2)$ is the carrier relaxation lifetime associated with intraband transitions, μ is the carrier mobility, $v_F=10^8$ cm/s is the Fermi velocity. It is obvious that both intraband and interband conductivities are closely related to the Fermi energy E_F determined by the carrier density $n=(E_F/\hbar\omega)^2/\pi$, which can be controlled by chemical, magnetical, or electrical doping, indicating that the ultimate tunability of graphene results from its dynamic conductivity. By analyzing the above equations, it is concluded that in the MIR~THz regime, interband conductivity can be ignored and only intraband conductivity need to be considered when $\hbar\omega<2E_F$, while in the visible~NIR regime, the interband conductivity dominates. This coincides well with the optical transition process in Fig. 2(e–h). At room temperature (T=300 K), if $E_F>>2k_BT$ (~25.8 meV), $2\cosh(E_F/2k_BT)\approx\exp(E_F/2k_BT)$, then the dynamic conductivity of graphene in the MIR~THz regime (only intraband) is re-written with the Drude form (like metals),

$$\sigma_g=\frac{ie^2E_F}{\pi\hbar^2(\omega+i\tau^{-1})}. \tag{2}$$

It can be seen that Eq. (2) equals to Eq. (1a) plus Eq. (1b) under conditions of $\hbar\omega<0.20$ eV and $\hbar\omega<2E_F$ (visually, $\lambda>6.2$ μm and $E_F>0.1$ eV). Therefore, the Drude model of Eq. (2) is credible for characterizing the graphene conductivity at MIR~THz frequencies, which is widely employed as the determined material property of graphene for theoretical and numerical models[164–170].

Plasmons in graphene

Different from photonic modes in dielectrics, there exist special EM modes at the interface of two materials with opposite signs of permittivity (for example, dielectric and conductor), called polaritons, which provide an extraordinary route to manipulate and harness light field below the diffraction limit[171–173]. In 2D materials, the polaritons can be clarified as plasmon polaritons[174], phonon polaritons[175], and exciton polaritons[176]. It is essential that to support and confine these polaritons at an interface, the real part of the permittivity of materials should be negative. As illustrated in Fig. 3, the dielectric function clearly shows the origination of negative permittivity for different polaritons[171]. For the plasmon polaritons, the negative permittivity covers the broadband frequency described by the Drude model (for example metals and graphene); While for phonon polaritons and exciton polaritons the bandwidth of negative permittivity is rather narrow due to the resonant absorption-induced highly dispersive permittivity. In the case of graphene, BP, and topological insulators (TIs), the oscillations of conduction electrons coupled with photons describe exactly the plasmon polaritons[177–179]; For *h*BN and TMDCs, polarized atom and exciton come into being phonon polaritons[180] and exciton polaritons[176], respectively. These polariton modes are highly confined at the interface of 2D materials and dielectric environment, and exhibit strong field enhancement, which provides a fascinating platform for manipulating wave-matter interactions. In the later part of the review, we focus on the plasmon polaritons in graphene, which have been taken full advantages to manipulate light fields with arbitrary amplitude, phase, polarization, and/or frequency when combined with the metasurface concept.

In fact, the plasmon polaritons bounded at the interface of a metal and a dielectric is as well-known as surface plasmon polaritons when coupled with photons, by which the important field of plasmonics was established in the last century and has derived straightforwardly the emerging field of nanophotonics[181–184]. Over the last few decades, a lot of interesting effects, phenomena, and advanced nanophotonic devices based on plasmons have been discovered including metasurfaces and metadevices using noble metals (e.g. gold and silver)[185–193]. In the ongoing search for alternative plasmonic materials, graphene emerged as a promising one for the MIR and THz applications. Currently, the development of graphene plasmonics is pushing forward the nanophotonics to the longwave infrared and be more powerful[194–198]. Compared with metallic plasmons, graphene plasmons (GPs) show several advantages. The first and most important is that the carrier density tunability of graphene by various external stimulus enables the flexibly tunable plasmon properties and active devices. Second, GPs can be excited and sustained from THz to MIR frequencies, where metallic plasmons suffer from larger losses, due to the small carrier density of graphene typically less than one percent of gold[199,200]. Third, GPs possess extremely strong field confinement together with relatively long propagation distance because of its 2D nature and high carrier mobility. The trade-off between the field confinement and propagation length is universal.

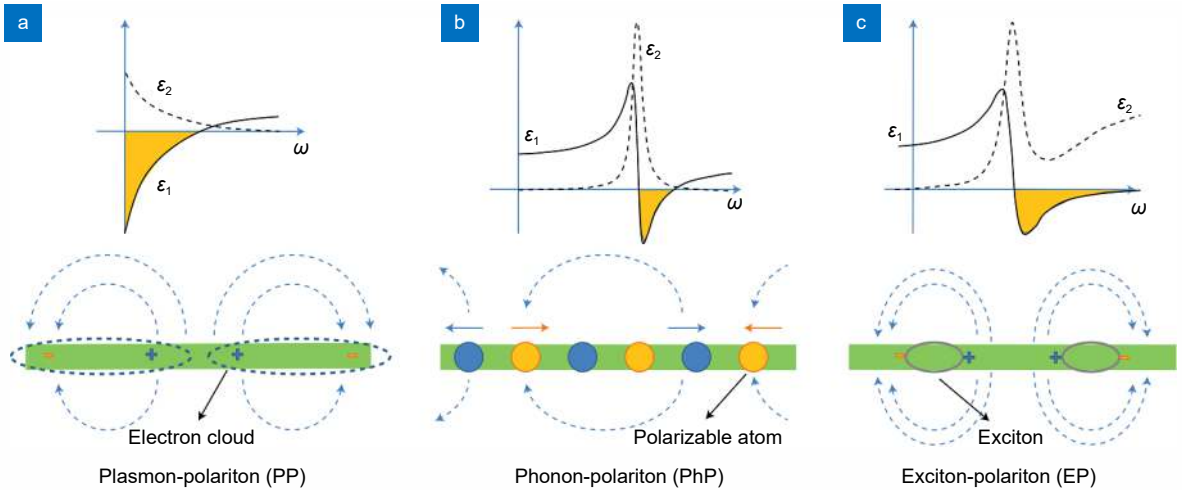

Fig. 3 | Polaritons in 2D materials with different dielectric functions and electric field line distributions. (**a**) Plasmon-polariton, (**b**) phonon-polariton, and (**c**) exciton-polariton. The symbol ε_1 represents the real part of permittivity, ε_2 imaginary part, and ω angular frequency of light. Figure reproduced with permission from ref.[171], © 2017 Springer Nature.

To achieve a large propagation length of GPs, increasing the doping density is a direct route, which in turns decreases the confinement. Even for very high-level doping, however, the penetration depth is still a few orders smaller than that of silver, indicating an appropriate balance of the trade-off and the advantage of field confinement under sufficient propagation length[201–204].

Similarly, GPs can be divided into propagating and localized modes according to their propagation conditions. Although it has been predicted theoretically that graphene supports plasmons, their exciting and detecting have remained a long-term challenge due to the large momentum mismatch between GPs and free-space photons[163,164,205]. In 2011, Ju et al. successfully excited GPs by coupling incident photons with dipolar plasmon resonances in artificially structured graphene and demonstrated the first graphene metamaterial for tunable THz filters[177]. As shown in Fig. 4(a), the proposed metamaterials consisted of a graphene ribbon array, fabricated using standard optical lithography and plasma etching of a large-area graphene on a Si/SiO_2 substrate, and the carrier concentration in the graphene ribbon was controlled by the ion-gel top gate. The experimental results in Fig. 4(b) demonstrated the active control of plasmon resonance through *in situ* electrostatic doping. In single-layer structured graphene, however, the magnitude of plasmon resonance is relatively weak. To overcome this limitation, in 2012, Yan et al. proposed a metamaterial

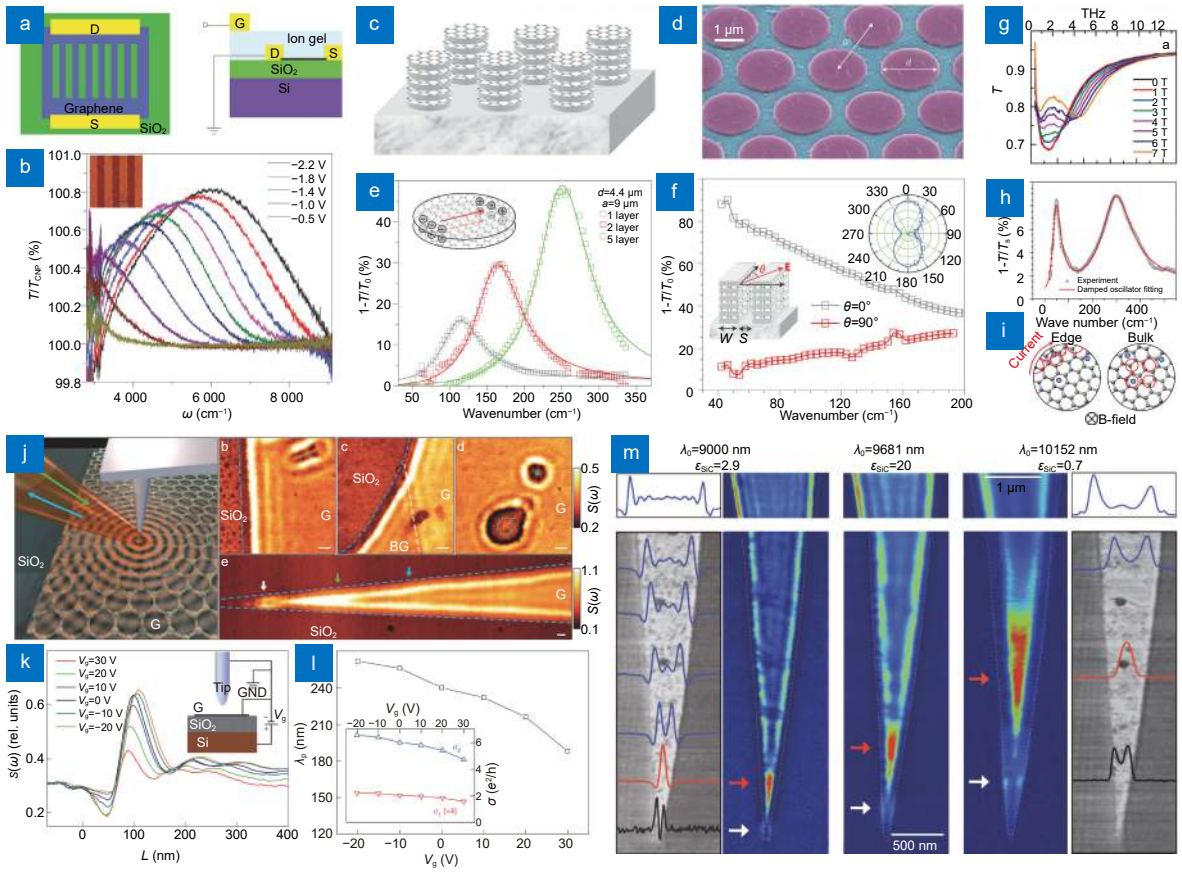

Fig. 4 | The pioneering experiments on GPs. Tunable THz metamaterials based on the gated graphene microribbon array: (**a**) top-view and side-view illustrations of a typical graphene microribbon array on a Si/SiO_2 substrate with ion-gel top gate, (**b**) transmission spectra of a graphene microribbon array as gate voltage (the inset: AFM image). Tunable infrared plasmonic devices using the stacked graphene/insulator array: (**c**) schematic diagram and (**d**) SEM image of the stacked graphene/insulator microdisk array, (**e**) extinction spectra for different layer numbers of disks, (**f**) extinction spectra of a tunable THz linear polarizer using a stacked graphene/insulator microribbon array. (**g**) Transmission spectra of graphene on SiC substrate with defects under different magnetic fields. (**h**) Extinction spectrum of the edge and bulk plasmon modes and (**i**) their corresponding illustration of charged carrier motions. Real-space imaging of GPs: (**j**) diagram of infrared nano-imaging experiment and images of plasmon field amplitude, (**k**) field amplitude perpendicular to the graphene edge and (**l**) plasmon wavelength as the function of gate voltage (the inset: back-gate bias set-up), (**m**) near-field optical images of graphene ribbon and tapered graphene ribbon with different wavelengths of excitation light. Figure reproduced with permission from: (a, b) ref.[177], © 2011 Springer Nature; (c–f) ref.[206], © 2012 Springer Nature; (g) ref.[207], © 2012 ACS; (h, i) ref.[208], © 2012 ACS; (j–l) ref.[210], © 2012 Springer Nature; (m) ref.[209], © 2012 Springer Nature.

device using structured graphene/insulator stacks[206]. Figure 4(c) and 4(d) illustrated the schematic diagram and SEM image of the proposed stacked graphene/insulator microdisk array, respectively. The extinction spectra for different layer numbers of graphene disks, as plotted in Fig. 4(e), showed that with the layer number increasing, the peak intensity of resonance increased significantly, and at the same time, the resonance frequency blue-shifted, which was attributed to the carrier redistribution in multilayer graphene because of strong Coulomb interaction of the adjacent layers. Based on the stacked graphene/insulator microdisk array, a tunable far-infrared notch filter was achieved. By etching the stacks into microribbon arrays, as shown in Fig. 4(f), a tunable THz linear polarizer was demonstrated with assistance of the polarization-dependent plasmon resonances in the ribbon. This work provides a simple method to effectively enhance and tune the frequency as well as magnitude of plasmon resonances in structured graphene. When a magnetic field is applied to the above structured graphene, the dipolar plasmon resonance shows a remarkable difference. In 2012, Crassee et al. found that the resonance peak of the intrinsic plasmons in graphene epitaxially grown on a SiC substrate with defects was modified dramatically by the high magnetic field, as shown in Fig. 4(g), the transmission dip split into two modes, which was so-called bulk and edge magnetoplasmon modes[207]. At the same time, such mode splitting phenomenon was experimentally observed by Yan et al. in graphene disk arrays under the magnetic field[208]. It was concluded that the high-frequency peak and low-frequency peak split from the intrinsic plasmon resonance, as shown in Fig. 4(h) and 4(i), corresponded to the bulk mode and edge mode, respectively, and the former underwent the collective cyclotron motion inside the disk, the latter featured a current along the edge and hence a rotating dipole. Due to the excitation of magnetoplasmons in structured graphene, Faraday rotation has been exploited to devise the metasurfaces for dynamic polarization control (to be discussed in Section *Dynamic spatial EM wave manipulations*). In the same year, Chen et al. and Fei et al., from two independent research groups, reported the real-space imaging of propagating and localized GPs in structure-engineered graphene using scattering-type scanning near-field optical microscopy (s-SNOM), as shown in Fig. 4(j–m)[209,210]. The near-field interference patterns in Fig. 4(j) and 4(m) clearly showed the propagation and localization of GPs, simultaneously revealing the relationships between the excitation wavelength, plasmon wavelength, and field confinement. The gate-voltage tunable fringe field amplitude (Fig. 4(k)) as well as plasmon wavelength (Fig. 4(l)) demonstrated the electrostatic tunability of GPs. This work provides the first direct-evidence of the tightly-confined field of GP mode, ultra-small plasmon wavelength (~50 times smaller than the wavelength of excitation light), and dynamically electrically-tunable functionalities based on GPs. It can be seen that, the excitation of GPs can be released from the large momentum mismatch requirement by patterning graphene into micro/nanostructures due to the plasmon resonances, while for a continuous graphene sheet the excitation is not easy, which is usually implemented by the metallized tip in s-SNOM that can overcome the large momentum mismatch by light scattering on the tip. These pioneering experimental works, assembled in Fig. 4, have provided the method to excite and detect GPs, classified the intrinsic plasmons and magnetoplasmons, and unveiled the fundamental properties of GPs, including dynamical electrostatic-tunability, ultra-short wavelength, and extremely strong field confinement.

Theoretical and numerical models of GPs

At the same time, a number of theoretical and numerical researchers have predicted that graphene can serve as the outstanding platform for guiding and manipulating energy flow in the 2D and 3D spaces with the assistance of GPs[211–222]. Here, in order to provide the fundamentals for Sections *Metasurfaces with building blocks of structured graphene* and *Hybrid metasurfaces integrated with graphene*, the theoretical and numerical models for propagating GPs in continuous graphene sheets and localized GPs in structured graphene are discussed in details. This Section not only provides a powerful methodology to build the graphene metasurfaces but also can promote a deep understanding of the physics in GPs, which is essential to developing accurate models of metasurfaces and metadevices before experiments. As shown in Fig. 5, we firstly discuss the transverse magnetic (TM) and transverse electric (TE) modes of GPs propagating along the x direction with $\exp(i\beta x)$ in a dielectric-graphene-dielectric waveguide. Actually, owing to the geometrical symmetry of the model, the guided TM and TE modes include odd and even modes with different transverse mode-field distributions along the z axis. For the sake of simplicity, only the odd mode

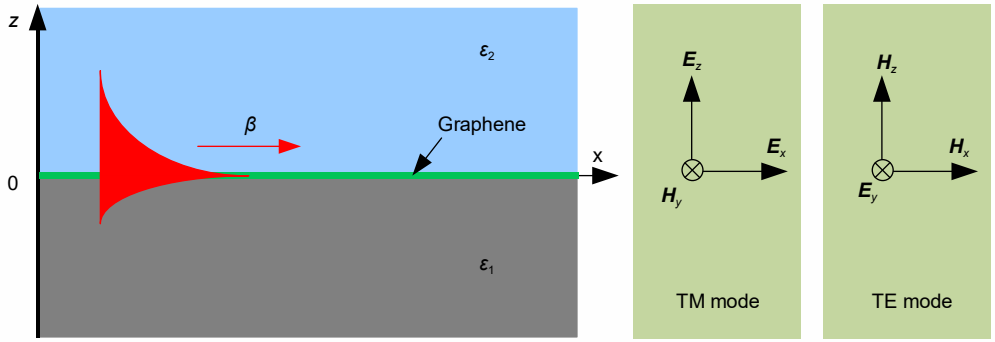

Fig. 5 | Schematic diagrams of a dielectric-graphene-dielectric waveguide and the EM components of the possible TM as well as TE GP modes. β denotes the propagation constant of GPs, ε_1 and ε_2 represent the relative permittivity of dielectrics below and above graphene sheet, respectively.

case is presented in the following discussions, and for the case of even modes the results can be easily obtained by the similar method.

To implement the theoretical analyses based on the Maxwell equations, graphene sheet is regarded as a conducting interface without thickness, and therefore the surface current $\boldsymbol{J}=\sigma_g\boldsymbol{E}$ exists at the sheet. For TM modes, the boundary condition is (z=0),

$$\begin{cases} E_x^{(1)}(0) = E_x^{(2)}(0) \\ H_y^{(1)}(0) - H_y^{(2)}(0) = \sigma_g \cdot E_x^{(1)}(0) \end{cases} . \tag{3}$$

According to the wave equations of EM field, the dispersion relation of TM GPs is then derived,

$$\frac{\varepsilon_1}{\beta_1} + \frac{\varepsilon_2}{\beta_2} = -\frac{\mathrm{i}\sigma_g}{\omega\varepsilon_0} , \tag{4}$$

here, wavevectors in dielectrics satisfy $\beta_{1,2}^2 = \beta^2 - \varepsilon_{1,2}\beta_0^2$, and the dispersion is re-written as,

$$\frac{\varepsilon_1}{\sqrt{\beta^2 - \varepsilon_1\beta_0^2}} + \frac{\varepsilon_2}{\sqrt{\beta^2 - \varepsilon_2\beta_0^2}} = -\frac{\mathrm{i}\sigma_g}{\omega\varepsilon_0} . \tag{5}$$

For TE modes, similarly, the boundary condition is (z=0),

$$\begin{cases} E_y^{(1)}(0) = E_y^{(2)}(0) \\ H_x^{(1)}(0) - H_x^{(2)}(0) = \sigma_g \cdot E_y^{(1)}(0) \end{cases} . \tag{6}$$

The dispersion relation of TE GPs is obtained,

$$\sqrt{\beta^2 - \varepsilon_1\beta_0^2} + \sqrt{\beta^2 - \varepsilon_2\beta_0^2} = -\mathrm{i}\omega\mu_0\sigma_g . \tag{7}$$

In simulations, graphene sheet is generally regarded as an ultrasmall-thickness (Δ) material with equivalent complex permittivity to represent its material property[223–225]. The volume conductivity $\sigma_{g,V}$ and volume current density $\boldsymbol{J}_V$ are,

$$\sigma_{g,V} = \sigma_g/\Delta , \tag{8a}$$

$$\vec{\boldsymbol{J}}_V = \sigma_{g,V}\vec{\boldsymbol{E}} . \tag{8b}$$

Assuming the average permittivity of surrounding dielectrics as ε_d, the Maxwell equations are,

$$\nabla \times \vec{\boldsymbol{H}} = \vec{\boldsymbol{J}}_V - \mathrm{i}\omega\varepsilon_0\varepsilon_d\vec{\boldsymbol{E}} , \tag{9a}$$

$$\nabla \times \vec{\boldsymbol{H}} = -\mathrm{i}\omega\varepsilon_0\varepsilon_g\vec{\boldsymbol{E}} . \tag{9b}$$

Therefore, the equivalent permittivity of Δ-thickness graphene sheet is expressed as,

$$\varepsilon_g = \varepsilon_d + \mathrm{i}\frac{\sigma_g}{\varepsilon_0\omega\Delta} . \tag{10}$$

It is found that $\mathrm{Re}(\varepsilon_g) = \varepsilon_d - \mathrm{Im}(\sigma_g)/(\varepsilon_0\omega\Delta) \approx -\mathrm{Im}(\sigma_g)/(\varepsilon_0\omega\Delta)$ and $\mathrm{Im}(\varepsilon_g) = \mathrm{Re}(\sigma_g)/(\varepsilon_0\omega\Delta)$, which implies that the sign of real (imaginary) part of equivalent permittivity is determined by the sign of imaginary (real) part of surface conductivity. Noteworthy, the sign of $\mathrm{Im}(\sigma_g)$ plays a crucial role in whether graphene supports TE or TM GP mode, which depends on the Fermi energy of graphene.

For the Δ-thickness graphene model, when $\mathrm{Im}(\sigma_g)<0$ (the interband contribution for conductivity is dominant at low Fermi energy), the TE mode is supported and its dispersion relation is[226],

$$\sqrt{\mu_0\varepsilon_0\varepsilon_g\omega^2 - \beta^2}\tan\left(\sqrt{\mu_0\varepsilon_0\varepsilon_g\omega^2 - \beta^2}\frac{\Delta}{2}\right) = \sqrt{\beta^2 - \mu_0\varepsilon_0\omega^2} . \tag{11}$$

Substituting Eq. (10) into Eq. (11) and letting $\Delta\to 0$, the dispersion of TE GPs is simplified to

$$\beta = \beta_0\sqrt{1 - \left(\frac{Z_0\sigma_g}{2}\right)^2} , \tag{12}$$

here $Z_0=1/(\varepsilon_0 c)=\mu_0 c=377\ \Omega$ is the vacuum impedance.

When $\mathrm{Im}(\sigma_g)>0$ (the intraband contribution becomes dominant at relatively high Fermi energy, $\hbar\omega<2E_F$), the TM mode is supported and its dispersion relation is[227],

$$\coth\left(\sqrt{\beta^2-\mu_0\varepsilon_0\varepsilon_g\omega^2}\frac{\Delta}{2}\right)=-\varepsilon_g\frac{\sqrt{\beta^2-\mu_0\varepsilon_0\omega^2}}{\sqrt{\beta^2-\mu_0\varepsilon_0\varepsilon_g\omega^2}}. \quad (13)$$

By the same processing method, the dispersion of TM GPs is reduced to,

$$\beta=\beta_0\sqrt{1-\left(\frac{2}{Z_0\sigma_g}\right)^2}. \quad (14)$$

It is obvious that, Eq. (12) and (14) can also be obtained by setting $\varepsilon_1=\varepsilon_2=1$ in Eq. (5) and (7), indicating the validity of this simulation model where graphene sheet is regarded as an equivalent material with Δ-thickness and permittivity governed by Eq. (10). By comparing Eq. (12) and (14), it is found that in contrast to TM GP mode, TE GP mode is a weakly-guided leaky mode and shows poor field confinement, defined by $\mathrm{Re}(\beta)/\beta_0$. As depicted in Fig. 6(a), the dispersion curve of TE GP mode almost coincides with that of air, which means that the TE GP mode cannot be sustained in an air-graphene-air waveguide, and the inset of Fig. 6(a) clearly shows such leaky property. On the contrary, TM GP mode exhibits good propagation and field confinement. At the same time, such properties can be controlled with great ease by tuning Fermi energy of graphene. From the viewpoint of surface conductivity ($\sigma=\sigma_{intra}+\sigma_{inter}$), the sign of $\mathrm{Im}(\sigma_{intra})$ is always positive so as to support TM GP mode, while the interband transition gives rise to the negative sign of $\mathrm{Im}(\sigma_{inter})$ and thereby TE GP mode is supported at high frequencies or low Fermi energy. As a consequence, graphene can selectively support either the TM or TE GP mode depending on its Fermi energy and the incident photon energy. Furthermore, Figure 6(b) show that the effective mode-field area (A_{eff}) of TM GP mode is almost one percent of that of gold with the same geometry, indicating the extremely high field confinement of TM GP mode. A number of works have well addressed the above issue on the propagating GPs along with graphene sheet from different perspectives, for example launching[228–232], guiding[233–235], coupling[236–238], detecting[150,239], confining[240,241], and tuning[242–245].

Therefore, to manipulate the energy flow of GPs propagating along with graphene sheet, it is critical to control the propagation conditions as described by Eqs. (5) and (14). It can be seen that the propagation performance of GPs is determined by the surface conductivity of graphene: the sign of $\mathrm{Im}(\sigma_g)$ determines whether the TM GP mode is supported ($\mathrm{Im}(\sigma_g)>0$) or not ($\mathrm{Im}(\sigma_g)<0$); the value of $\mathrm{Im}(\sigma_g)$ determines the propagation characteristics of the TM GPs. Accordingly, modulating the surface conductivity of graphene is an efficient way to manipulate the energy flow of propagating GPs on 2D plane. In 2011, Vakil and Engheta reported a theoretical study to demonstrate graphene as a one-atom-thick platform for 2D transformation optics based on GPs through spatially modulating the surface conductivity of graphene[211]. The model was on the basis of the parallel capacitor with graphene sheet as the upper plate, highly doped silicon as the ground plate, and dielectric as the spacer, as schematically shown in Fig. 7(a) and 7(b). According to the basic principle of the parallel capacitor, the relationship between the charge Q on plates and voltage V between plates is governed by $Q=\varepsilon\cdot A\cdot V/h$. Under conditions that the plate area A is fixed, the change of the voltage V, the separation h between two plates, or

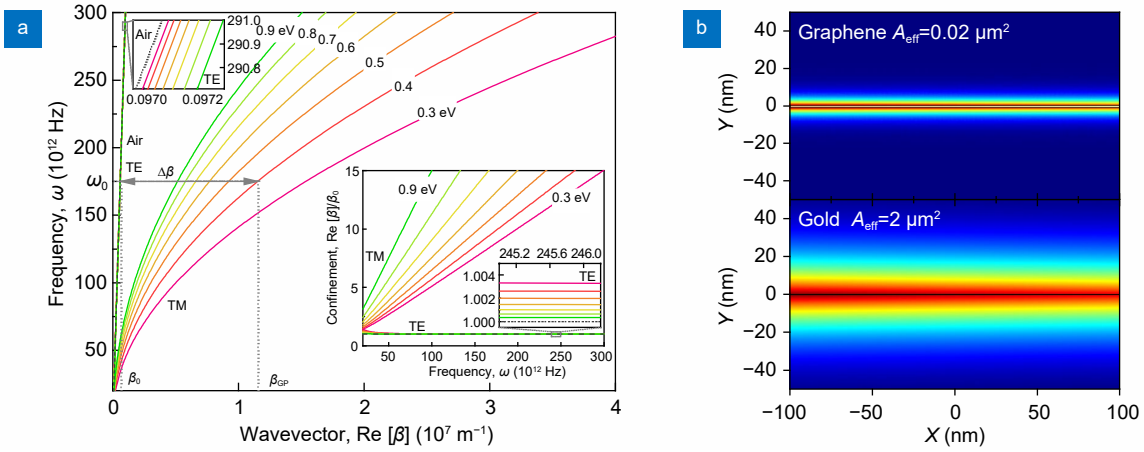

Fig. 6 | Fundamental properties of TM and TE GPs in an air-graphene-air waveguide. (**a**) Dispersion relation and field confinement of TM and TE GPs as the function of Fermi energy calculated from Eqs. (12) and (14) in the MIR~THz regime. (**b**) Field confinement comparison between graphene and gold waveguide using the model in Fig. 5 with the same geometric parameters.

the dielectric permittivity ε of the spacer would result in the charge Q change on plates, corresponding to the carrier density (or Fermi energy) of the graphene plate. Therefore, by controlling the parameters of the capacitor, the tuning of density and distribution of carrier in graphene due to the static electric-field effect can be realized and hence spatially modulating the surface conductivity of graphene sheet can be achieved. As shown in Fig. 7(a), if the ground plate is uneven ($h_1 \neq h_2$), the nonuniform electric field on graphene results in nonuniform conductivity patterns of graphene. On the other hand, the nonuniform conductivity patterns can be achieved by a nonuniform spacer for example unequally doped silica ($\varepsilon_1 \neq \varepsilon_2$), as shown in Fig. 7(b). The simulated results in Fig. 7(c) well demonstrated the above theoretical model, showing the electrical control of propagating GPs by spatially modulating the conductivity of graphene[211]. And further, as shown in Fig. 7(d), a 2D GP waveguide was designed with suitable conductivity patterns. In 2014, Alonso-González et al. experimentally demonstrated the control of propagating GPs using spatial conductivity patterning method[205]. In their experiments, a graphene bilayer prism was implemented to investigate the refraction behavior of GPs propagating along with graphene sheet, and the plasmon wavelength of GPs in bilayer graphene was 1.4-times larger than that in single-layer graphene observed by the near-field imaging, which was attributed to the locally increased conductivity of bilayer graphene (theoretically 1.41-times larger than that of single-layer graphene). The spatial conductivity patterning model provides a theoretical method to dynamically modulate the conductivity of graphene and more importantly, to manipulate the energy flow of propagating GPs on 2D plane without directly patterning graphene, which has triggered the graphene-based 2D optics and a large number of electrically-tunable planar devices including metasurfaces (to be discussed in Section *Dynamic surface EM wave manipulations*).

Compared with the launching difficulty of propagating GPs, structured graphene provides an efficient route to avoid the large momentum mismatch between GPs and excitation light by plasmon resonances, usually termed the localized GP mode[177,206]. As discussed in Section *Basic material properties of graphene*, the surface conductivity of a continuous graphene sheet is described by Eq. (2). For the structured graphene array such as ribbon and disk, its conductivity should be averaged with respect to the unoccupied area. Under the condition of

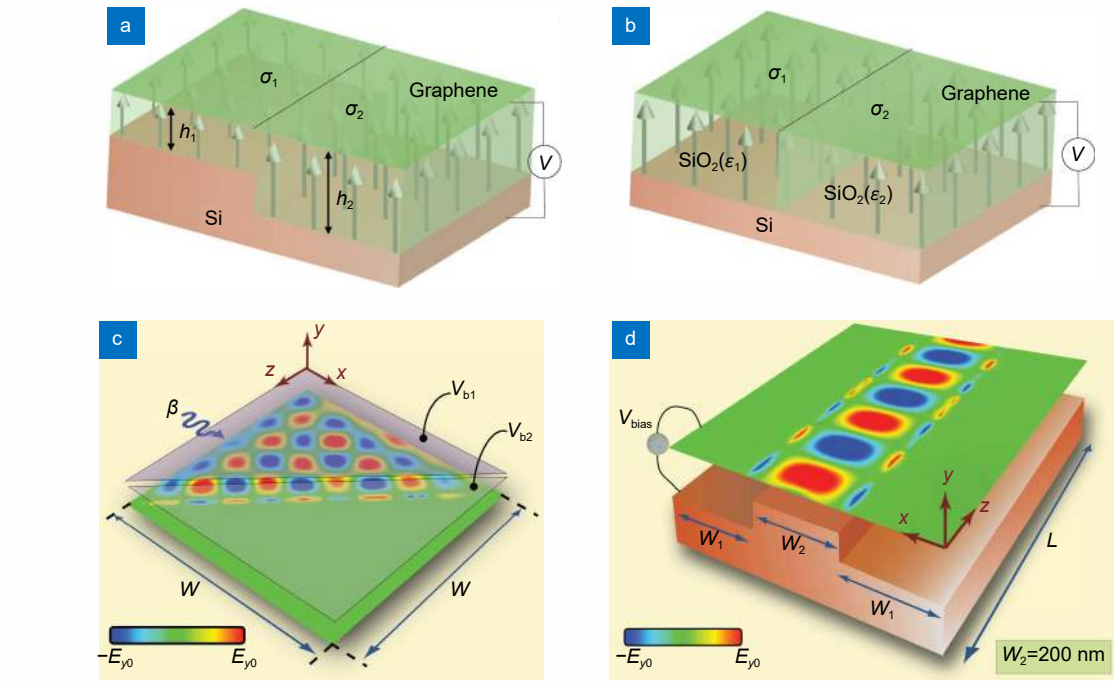

Fig. 7 | Theoretical models and numerical results for manipulating the energy flow of propagating GPs on 2D plane of graphene sheet by spatially modulating the surface conductivity of graphene. Schematic diagram of the parallel capacitor model with (**a**) uneven ground plate Si ($h_1 \neq h_2$) and (**b**) nonuniform spacer for example differently doped SiO_2 ($\varepsilon_1 \neq \varepsilon_2$). (**c**) Simulated propagation of GPs on a graphene sheet with different bias voltages (V_{b1} corresponds to $\mathrm{Im}(\sigma_g)>0$ and V_{b2} corresponds to $\mathrm{Im}(\sigma_g)<0$). (**d**) Simulated results of graphene-based 2D waveguide using the model in (a). Figure reproduced with permission from: (c, d) ref.[211], © 2011 AAAS.

the quasi-static approximation and without lateral coupling of the neighboring unit, the average conductivity of a structured graphene array is given as[206,213],

$$\sigma_g = \mathrm{i}\frac{fD}{\pi}\frac{\omega}{(\omega^2-\omega_p^2)+\mathrm{i}\Gamma_p\omega}\ , \tag{15}$$

where f is the filling factor (the ratio of graphene area to total area), $D=e^2E_F/\hbar^2$ is the Drude weight, and Γ_p is the plasmon resonance width of structured graphene, which is usually 10% larger than the Drude scattering width $\Gamma=ev_F^2/(\mu E_F)$ of continuous graphene sheet. The frequency ω_p of graphene plasmon resonance (GPR) is expressed as[206,246],

$$\omega_p = \sqrt{\frac{3D}{8\varepsilon_m\varepsilon_0 d}}\ , \tag{16}$$

here ε_m is the average permittivity of dielectrics below and above graphene, d is the size (width or diameter) of structured graphene. It can be seen that the average conductivity of structured graphene is closely related to the frequency of GPR, which is mainly determined by its geometric size, Fermi energy, and surrounding dielectrics, indicating the flexible tunability of GPRs in structured graphene.

To perform the light transmission, reflection, and absorption at the interface of metasurface based on structured graphene, the Fresnel coefficients should be found out first. Figure 8 illustrates the schematic model of reflection and refraction of p-polarized light passing through a dielectric-graphene-dielectric interface. Similar to the propagation model in Fig. 5, here graphene sheet is also treated as a conductive interface with zero-thickness. The boundary condition of electric fields is,

$$\begin{cases} \vec{\boldsymbol{n}}\times(\vec{\boldsymbol{E}}_2-\vec{\boldsymbol{E}}_1)=0 \\ \vec{\boldsymbol{n}}\cdot(\vec{\boldsymbol{D}}_2-\vec{\boldsymbol{D}}_1)=\rho_g \end{cases}\ , \tag{17}$$

here the surface charge density of graphene ρ_g can be expressed using conductivity[247],

$$\rho_g = \sigma_g \boldsymbol{E}_t\beta_z\cos\theta_2/\omega\ . \tag{18}$$

Then, Eq. (17) is re-written by the Fresnel coefficients, i.e. reflection coefficient ($r_{12}=\boldsymbol{E}_r/\boldsymbol{E}_i$) and transmission coefficient ($t_{12}=\boldsymbol{E}_t/\boldsymbol{E}_i$),

$$\begin{cases} (1-r_{12})\cos\theta_1 - t_{12}\cos\theta_2 = 0 \\ \varepsilon_0\varepsilon_1(1+r_{12})\sin\theta_1 - t_{12}(\varepsilon_0\varepsilon_2\sin\theta_2+\sigma_g\beta_z\cos\theta_2/\omega)=0 \end{cases}\ . \tag{19}$$

Solving Eq. (19) results in the Fresnel coefficients of graphene interface. In the case of normal incident ($\theta_1=\theta_2=0$), the Fresnel coefficients can be obtained as,

$$\begin{aligned} r_{12} &= \frac{n_1-n_2-Z_0\sigma_g}{n_1+n_2+Z_0\sigma_g},\ t_{12}=\frac{2n_1}{n_1+n_2+Z_0\sigma_g}, \\ r_{21} &= \frac{n_2-n_1-Z_0\sigma_g}{n_1+n_2+Z_0\sigma_g},\ t_{21}=\frac{2n_2}{n_1+n_2+Z_0\sigma_g}. \end{aligned} \tag{20}$$

From Eq. (20), it can be seen that the Fresnel coefficients of graphene interface are determined by its conductivity. As discussed above, for a structured graphene array, its conductivity is governed by Eq. (15), which is closely related to the GPRs. Therefore, the Fresnel coefficients of a structured graphene array can be dynamically tuned by controlling the geometric size, Fermi energy, and surrounding dielectrics. Here, graphene nanoribbon array on SiO_2 substrate is taken as an example to discuss the transmissivity and reflectivity of light (the calculation settings can be found in ref.[248]). Different from the 97.7% transmittance of a continuous graphene sheet over a broad band, the reflection and transmission spectra of graphene nanoribbon array in Fig. 9 show strong filtering features and also the tunable property with varying the Fermi energy, which is in accordance with the previous experiments[177,206]. Besides the amplitude manipulation based on GPR filtering (usually called frequency-selective metasurface) using various structured graphene such as ribbon[170,249], disk[250,251], ring[252,253], and other resonators[254–257], metasurfaces made of structured graphene based on localized GPs have been extensively researched to dynamically control the phase and polarization of light (to be discussed in Section *Dynamic spatial EM wave manipulations*).

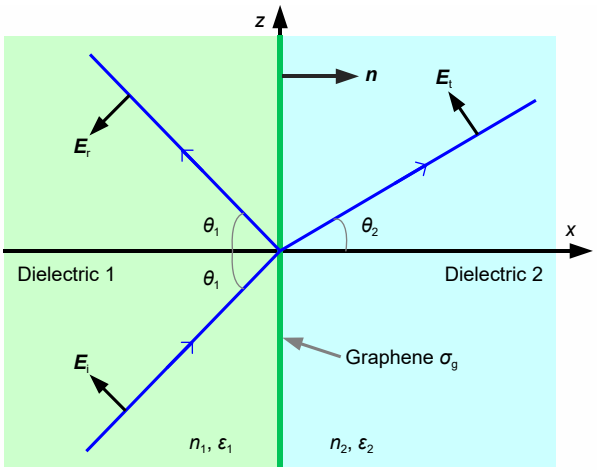

Fig. 8 | Schematic model of reflection and refraction of p-polarized light passing through a dielectric-graphene-dielectric interface. The annotated parameters represent: n_1 (ε_1) and n_2 (ε_2) the refractive indices (permittivities) of dielectric 1 and 2; θ_1 and θ_2 the angles of incidence/reflection and refraction; $\boldsymbol{E}_i$, $\boldsymbol{E}_r$, and $\boldsymbol{E}_t$ the amplitudes of incident, reflected, and transmitted electric fields; $\boldsymbol{n}$ the normal direction.

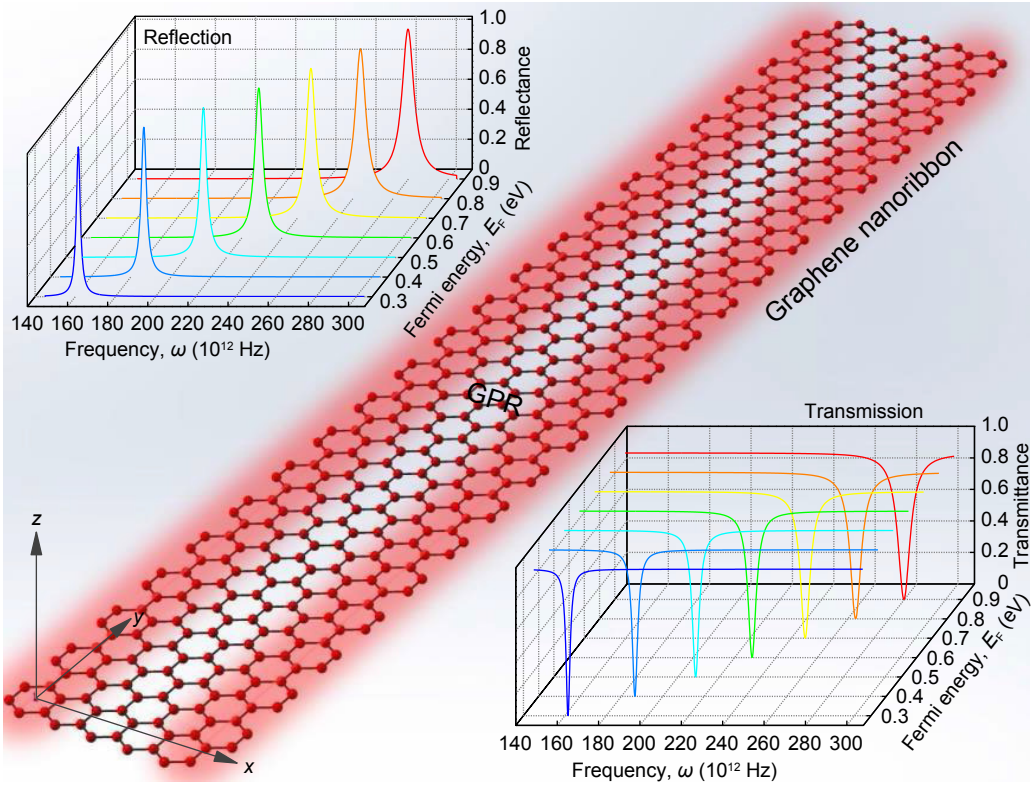

Fig. 9 | Calculated dynamic transmission and reflection of light due to the GPRs in graphene nanoribbon array according to Eq. (20). The width of graphene nanoribbon is ~100-nm-scale along *x* axis and infinite along *y* axis. The incident light is linearly polarized along *x* axis.

Metasurfaces with building blocks of structured graphene

Due to supporting the plasmon modes, naturally, graphene has been developed as the host materials for building plasmonic metasurfaces as that of noble metals, which not only extend the working frequency of metasurfaces from visible and NIR to MIR and THz but also empower the active tunability to them. To construct the GP metasurfaces, how to pattern graphene into diverse metaatoms (micro/nanostructures) is a matter of great concern. Different from bulk metals, it is difficult to structure one-atomic-thick graphene with enough degrees of freedom, leading to the poor family of metaatoms made of graphene. As discussed in Section *Fundamentals of graphene*, in general, there are two technology roadmaps to accomplish this task: one is directly patterning graphene into various geometric structures by advanced fabrication process[39,177,206,258–260], the other is spatially modulating the surface conductivity of graphene to implement equivalently patterning[211,261–264]. The former usually exploits metasurfaces with functionalities of spatial EM wave manipulations in the 3D space (far-field), while the latter mainly provides the ideal platform to manipulate the surface EM wave (propagating GPs) on the 2D plane (near-field). In this Section, recent advances on dynamic spatial and surface EM wave manipulations using plasmonic metasurfaces made of structured graphene are discussed with respect to their dynamic functionalities of the spectrum modulation, wavefront shaping, polarization control, and frequency conversion in the MIR and THz regimes, which are associated with single- or multi-dimensional manipulations of the EM waves.

Dynamic spatial EM wave manipulations

Spectrum modulation

The localized plasmon resonances in graphene nanostructures enable the dramatic filtering of the transmission, reflection, and absorption spectra, offering an efficient way to manipulate the amplitude and frequency of light waves. External stimuli induced tunability of the resonance, such as intensity modulation and wavelength shift of the resonance, makes the spectrum modulation become active control and thereby enable dynamically tunable devices such as tunable filters, sensors, and modulators. Due to such spectral filtering in frequency domain, metasurfaces consisting of periodically patterned graphene (metaatoms) arrays are generally called

frequency-selective metasurfaces, as shown in Fig. 10, including graphene ribbon, disk, ring, split-ring, and other structures. Inspired by the pioneering works[177,206], metasurfaces based on graphene ribbons or disks are the first and extensively researched. Chu and Gan reported a theoretical and numerical study on an active plasmonic switch based on graphene ribbon array operating in the MIR spectrum[170]. As shown in Fig. 10(a), the resonance wavelength of the metasurface can be controlled through passive and/or active tunings: the former is related to the ribbon width and the layer number of graphene, the latter is *in situ* variations of the Fermi energy of graphene ribbon. When slightly changing the Fermi energy, the dynamical resonance wavelength shifts and intensity modulations on the transmission spectra were achieved with great ease. Liu et al. investigated the plasmon modes in graphene rings with symmetric and anti-symmetric structures, as shown in Fig. 10(b), and demonstrated their potentials for optical antennas with highly tunable extinction spectra in THz range[265]. Fang et al. experimentally demonstrated electrical tunability and hybridization of localized GPRs in graphene nanodisks and nanorings[167]. The ion-gel top-gate configuration was proposed to accomplish the electrical doping of the patterned graphene array, as shown in Fig. 10(c). The reflection spectra of the metasurface exhibited flexibly tunable extinction peaks (both amplitude and frequency) produced by the GPRs in nanodisks. Additionally, such spectrum modulation can be brought closer to the NIR in graphene nanoring arrays due to the plasmon hybridization. Papasimakis et al. revealed the strong magnetic response in graphene split rings at THz frequencies[253]. By

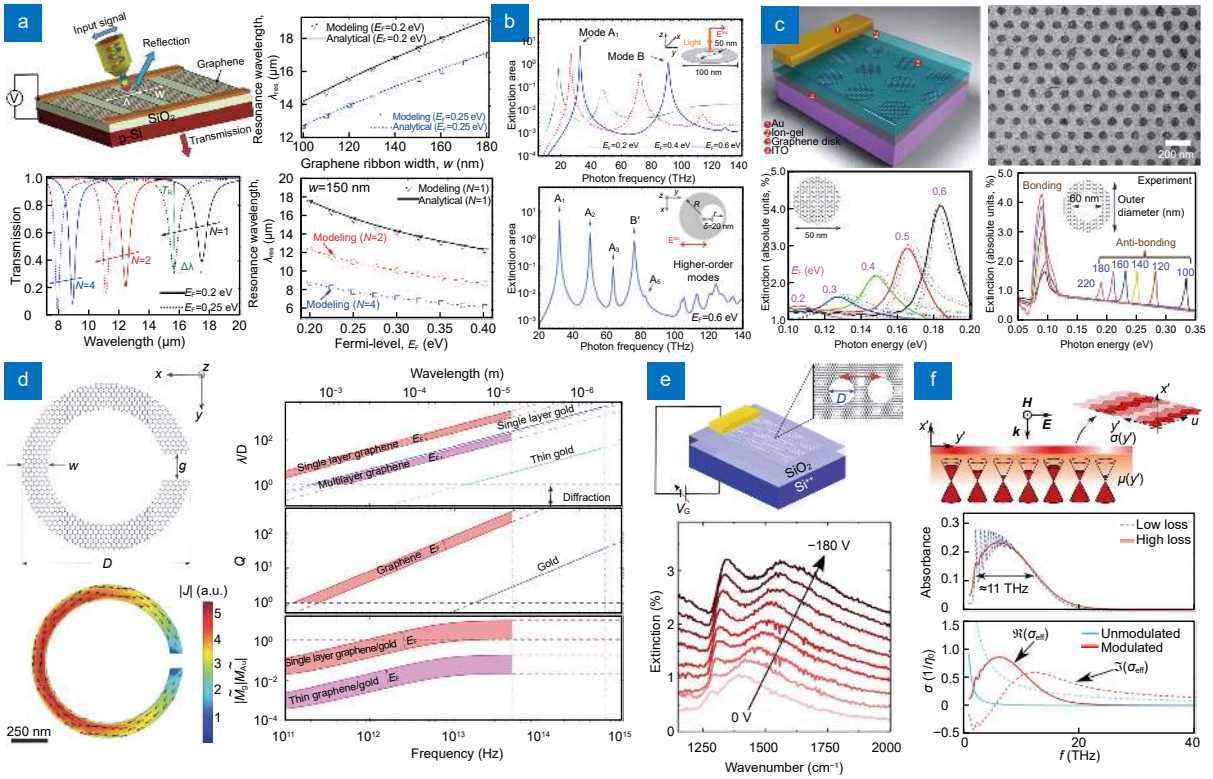

Fig. 10 | Dynamic modulation of the resonance spectra using GP metasurfaces consisting of various localized plasmon resonant structures. (**a**) Graphene ribbon: schematic illustration of the device, transmission spectra with different number of graphene layers, arrays with back gate, passive (with ribbon width) and active (with Fermi energy) tunings of plasmon resonance wavelength. (**b**) Graphene ring: extinction area in graphene rings with symmetric and anti-symmetric structures. (**c**) Graphene disk and ring: scheme of the device consisting of graphene nanodisk array, SEM image of the sample, extinction spectra of graphene nanodisks with different Fermi levels and of graphene nanorings with different outer diameters. (**d**) Graphene split-ring: schematic diagram, simulated on-resonance induced current distribution, comparisons of confinement, quality factor, and the ratio of magnetic polarizability density with varying Fermi level. (**e**) Graphene nanohole: schematic of the device, measured extinction spectra as a function of gate voltage. (**f**) Graphene with 2D conductivity modulation: schematic of the metaatom, simulated transmission and absorption spectra. Figure reproduced with permission from: (a) ref.[170], © 2013 AIP Publishing; (b) ref.[265], © 2012 AIP Publishing; (c) ref.[167], © 2013 ACS; (d) ref.[253], Creative Commons Attribution-NonCommercial-Share Alike 3.0 Unported License; (e) ref.[267], © 2018 ACS; (f) ref.[268], © 2018 ACS.

comparing with gold, graphene exhibited unprecedented advantages in the degree of confinement, quality factor of GPRs, magnetic polarizability density, and in particular the electrically-tunable optical response, as presented in Fig. 10(d), which can be beneficial for the fabrication of active metasurfaces in the THz regime. On the basis of the Babinet structure of two split rings in orthogonal orientation, Li et al. constructed a graphene planar chiral metasurface and reported the tunable dual-band asymmetric transmission for circularly polarized (CP) waves[266]. In 2018, Gopalan et al. proposed a scalable nanoimprint technique to fabricate graphene nanostructures over wafer-scale areas instead of the expensive and low-throughout lithography techniques[267]. As shown in Fig. 10(e), the large-area graphene nanohole arrays were demonstrated with gate-tunable spectral response. In addition to the directly patterned graphene nanostructures, equivalent patterning of graphene by exploiting spatial modulation of the graphene's conductivity is also demonstrated to construct GP metasurfaces with tunable spectral responses. Researchers from Pendry's group proposed a transformation optics approach to design GP metasurfaces with tunable, broadband spectral features[264,268]. As shown in Fig. 10(f), by periodically doping a graphene sheet along one spatial dimension, a subwavelength graphene grating metasurface was achieved with singularities, whose spectrum presented strong and broadband absorption of the THz waves. This work provides an alternative route to implement featured spectrum generation and modulation, in particular enhancing the absorbance and bandwidth of the metasurfaces. It can be seen that in the single-layer graphene nanostructures, the strengths of GPRs are relatively low at low carrier density, and the strengths can be elevated by heightening the doping level, which however is challenging to achieve without reducing the carrier mobility and stability. In the pursuit of strong resonances together with tunability, two efficient approaches are widely adopted: one is by the aid of total internal reflection or a dielectric-coated metal substrate[213,269], the other is using graphene multilayer stacks[206,256,270].

The active control of the plasmon resonance spectrum is of great importance to enhance the performance of GP metasurfaces and metadevices, especially tuning and extending their working wavelength dynamically, which is very attractive for practical applications[271–275]. As an example, here tunable MIR plasmonic sensors using graphene metasurfaces are taken. In 2015, Rodrigo et al. reported a high-sensitivity and electrically-tunable plasmonic biosensor for detecting the protein in a label-free fashion using graphene metasurfaces[272]. As shown in Fig. 11(a), the proposed metasurface is graphene nanoribbon array with electrostatic gating, and protein sensing is enhanced by plasmons and accomplished by detecting the spectral shifts of plasmon resonances. Noteworthy, the vibrational fingerprints of proteins located at 1660 and 1550 cm^{-1} were almost undetectable when they were far away from the plasmon resonance wavelength (e.g. for V_g= −20 V); While for V_g= −130 V the vibrational modes induced decrease in extinction was clearly visible as two dips, which resulted from the resonant coupling of plasmon resonance and molecular vibrations. It is an impossible mission if the active tunability of the protein sensor was absent. Hu et al. went a step further to demonstrate the simultaneous detection of in-plane and out-of-plane molecular vibrational modes with ultrahigh sensitivity by using graphene nanoribbon arrays, which pushed the near-field detection of molecular fingerprints to the far field[271]. The *in situ* electrical tunability of GPRs ensured an extremely wideband detection covering the entire region of molecular fingerprints. More recently, graphene metasurfaces with nanoribbon arrays have been developed to detect gas molecules (such as SO_2 and CO_2)[274,275]. Besides the molecular fingerprint detections, Zundel and Manjavacas proposed a MIR sensor to detect the position of molecules on sensors with the subwavelength spatial resolution by taking advantage of the electrical tunability of GPRs[273]. Figure 11(b) shows the concept of the sensor, composed of finite graphene nanodisk arrays with identical subarrays (or pixels). The doping levels of nanodisks in each subarray were the same and adjustable. Thus, by independently adjusting the doping levels of different subarrays, simultaneous identification of the target molecule and detection of its spatial position could be enabled. The absorption cross-section of each nanodisk indicated different wavelengths of GPRs for different doping levels and also their high-sensitivity shifts. The variation of the absorption cross-section clearly revealed the presence or absence of molecules in the active pixel, and finally the position of molecules could be detected with spatial resolution of the pixel size, as shown in Fig. 11(b). Although it is difficult to individually control the doping level of each pixel, this work brings new opportunities to design GP metasurfaces with position sensing functions

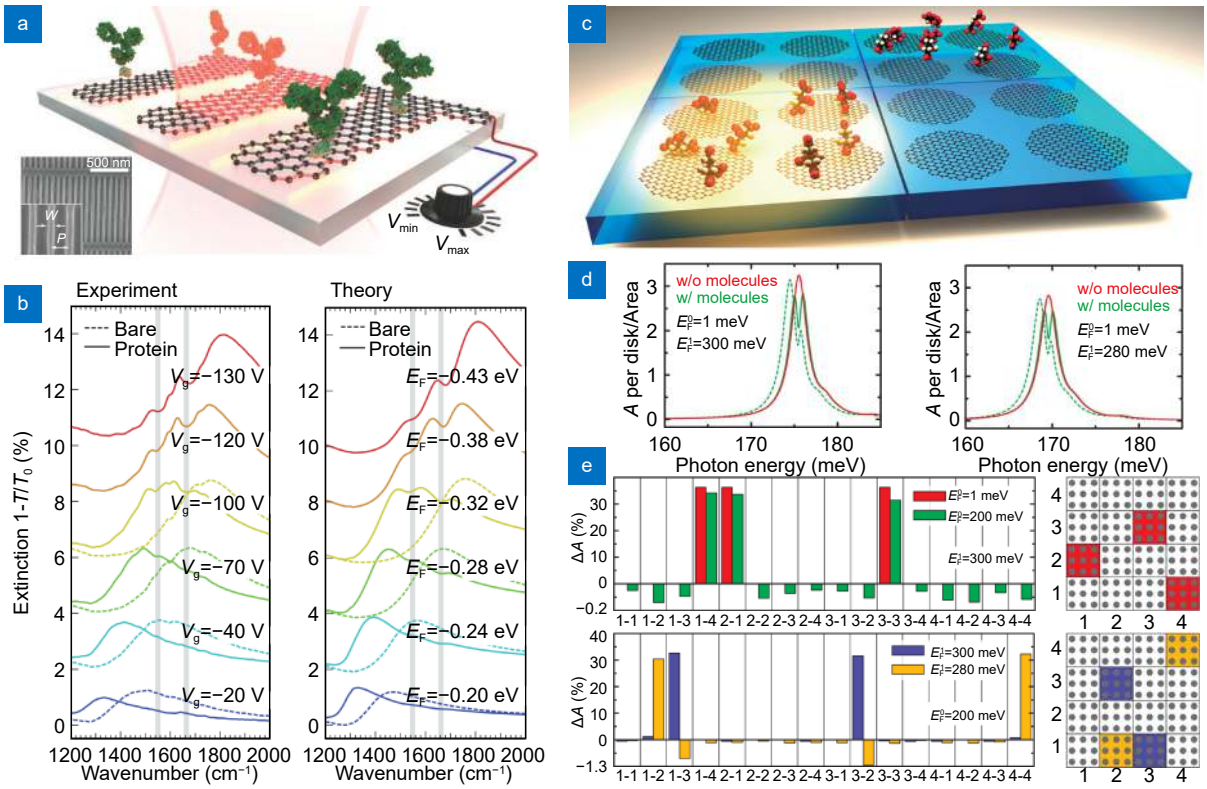

Fig. 11 | Tunable biosensors of vibrational fingerprints using GP metasurfaces based on electrically-tunable spectra of GPRs. Detection of the vibrational fingerprints of proteins: (**a**) conceptual view of the sensor based on electrostatically-gated graphene nanoribbon arrays, (**b**) measured and calculated extinction spectra for varying bias voltage V_g and corresponding Fermi energy E_F. Detection of the vibrational fingerprints and position on the sensor surface of molecules: (**c**) schematic diagram of the sensor with pixeled graphene nanodisk arrays and subarrays, (**d**) absorption cross-section and (**e**) its variation as a function of the active pixel (position). Figure reproduced with permission from: (a, b) ref.[272], © 2015 AAAS; (c–e) ref.[273], © 2017 ACS.

at low frequencies (usually with much large size of metaatom).

The unit cell in the above-discussed GP metasurfaces is independent of each other, and hence the response is solely determined by the individual metaatom. However, it will be significantly different when the neighboring metaatoms are coupled. The occurrences of interesting phenomena and effects have been reported such as unprecedented levels of field enhancement by strong plasmon interaction of coupled graphene nanostructures[276,277]. As its great potential in optical spectrum modulation, electromagnetically induced transparency (EIT) with the sharp and pronounced spectral response has attracted enormous attention, which has been well-studied in metallic plasmonic metasurfaces and metamaterials[186]. In 2013, Cheng et al. proposed a dynamically wavelength-tunable EIT metasurface in the MIR regime based on graphene nanostrips[278]. The metaatom consisted of the laterally coupled graphene nanostrips, i.e. one central nanostrip and two parallel nanostrips, as shown in Fig. 12(a). When the symmetry of the metaatom was broken (there existed a lateral displacement), as shown in Fig. 12(b), a transmission peak emerged and increased with the increase of asymmetry. The electric field distributions at different displacements unveiled the physical origin of the EIT, resulting from the near-field coupling of the bright modes in the central nanostrip and dark modes in two parallel nanostrips. Due to the tunable GPRs in nanostrips, the EIT spectra were inherently tunable in a broad range of MIR, as shown in Fig. 12(c). Inspired by this work, we proposed a phase-coupling scheme to generate and modulate EIT using GP metasurfaces[248]. As shown in Fig. 12(d), the metasurface consisted of two graphene ribbon arrays (GRAs) spatially separated by a dielectric spacer, and the ion-gel gates were used to control the Fermi energy of GRAs independently, which formed a Fabry-Perot (FP) cavity with controllable Fresnel coefficients. The GRAs were modeled as the interfaces with tunable Fresnel coefficient and plasmon resonance spectra, as discussed in Section *Theoretical and numerical models of GPs*. When the plasmon resonance wavelengths of two GRAs were

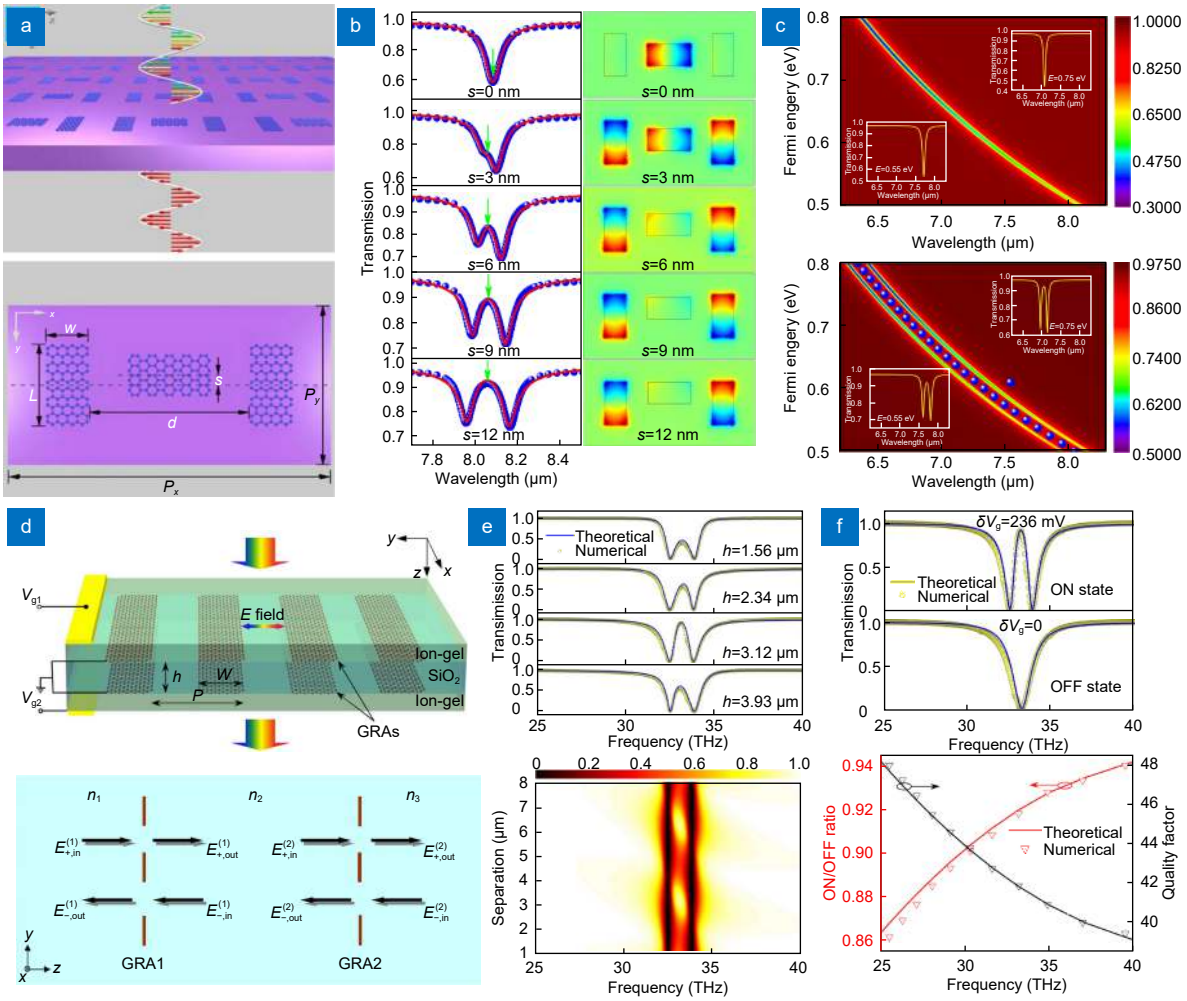

Fig. 12 | Coupling-induced dynamic spectrum modulation with the tunable EIT features using GP metasurfaces. Near-field-coupled graphene nanostrips: (**a**) schematic model, (**b**) transmission spectra and plasmon mode distribution with varying coupling distances, (**c**) transmission spectra as a function of Fermi energy for coupling distances of *s*=0 and 12 nm. Phase-coupled graphene ribbons: (**d**) schematic configuration and transfer matrix model, (**e**) transmission dependence on different separations *h*, (**f**) demonstration of electro-optical switch based on the graphene metasurface. Figure reproduced with permission from: (a–c) ref.[278], © 2013 AIP Publishing; (d–f) ref.[248], © 2014 AIP Publishing.

slightly detuned (through gate-voltage detuning), a transparency peak was observed around the original transmission dip. This was attributed to the constructive interference between the light waves reflected by two GRAs, which was validated by both transfer matrix analyses and numerical simulations. The separation-dependent periodic EIT evolutions are shown in Fig. 12(e) clearly demonstrated that phase coupling contributed to the generation of EIT. By controlling the gate voltage applied on two GRAs, a frequency-selective electro-optical switch was demonstrated with intensity modulation depth larger than 86% over a wide band frequency in the MIR regime, as shown in Fig. 12(f). By cascading such FP cavity, furthermore, a tunable multiple EIT metadevice was conceived[279]. Recently, we achieved the dynamic Fano spectral response using graphene metasurface based on near-field coupling by controlling the Fermi energy of graphene and the polarization of incident MIR light[280]. On the basis of the near-field coupling or phase coupling scheme, currently, graphene-based EIT or Fano metasurfaces with diverse metaatoms have been demonstrated to implement active metadevices with dynamic spectrum modulations[281–284].

Wavefront shaping

Besides the amplitude manipulation, plasmon resonances in graphene nanostructures can also effectively produce the scattering phase retardation, which is strongly associated with the geometry and wavelength. Recently, GP metasurfaces have been widely demonstrated to control the wavefront of light based on the amplitude and phase manipulations. Here, we will

discuss the research progress on graphene-based dynamic metasurfaces for active wavefront shaping. To start with, the phase and amplitude manipulation by graphene nanoribbon metasurfaces are shown in Fig. 13. In 2014, Lu et al. investigated the scattering properties of graphene nanoribbon and found that unit cell with a pair of graphene nanoribbons could provide 0~π phase modulation with large amplitude, as shown in Fig. 13(a)[285]. To realize the full 2π phase coverage, which is crucial for complete wavefront shaping, and also enhance the intrinsically weak light-graphene interaction, Li et al. proposed and demonstrated a GP metasurface to dynamically control the phase and amplitude of light using graphene ribbons on a dielectric/metal substrate[286]. Figure 13(b) shows the schematic configuration of the proposed metasurface, which was the combination of a graphene nanoribbon array and a subwavelength-thick FP cavity. Simulation results in Fig. 13(c) revealed that the phase of the reflected light could almost cover the range from –π to π through varying the ribbon width at a suitable dielectric thickness and, at the same time, the reflectivity was larger than 48.6%. By managing the phase shift distribution along with the interface through graphene ribbons with different widths, a reflective focusing lens was achieved. As shown in Fig. 13(d), the focal length, size and intensity of the spot could be dynamically tuned by adjusting the Fermi energy. By managing the graphene ribbon with different Fermi energy, Yatooshi et al. demonstrated the wavefront control of THz wave using the similar graphene metasurface[287]. In 2017,

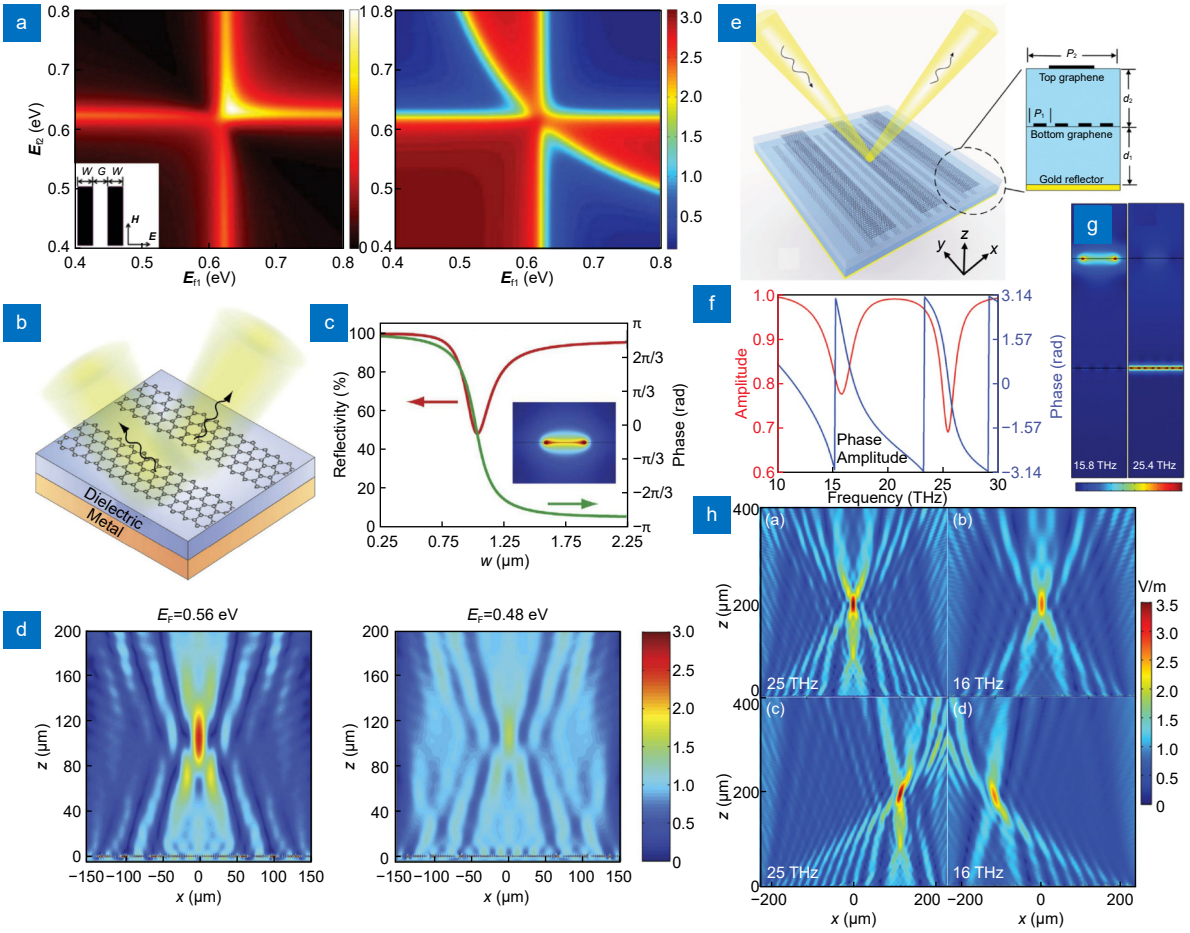

Fig. 13 | Dynamic wavefront shaping using GP metasurfaces based on resonance phase. (**a**) Scattering amplitude and phase as the function of Fermi level of the unit cell with two graphene nanoribbon. FP cavity-enhanced graphene metasurface: (**b**) schematic of metasurfaces, (**c**) reflectivity and phase of the reflected light as a function of ribbon width, (**d**) focusing performance at different Fermi levels. Dual-band light focusing reflector using stacked graphene nanoribbon metasurfaces: (**e**) schematic model, (**f**) amplitude and phase responses of the reflected light, (**g**) the relative electric field distributions at resonant frequencies of 15.8 and 25.4 THz, (**h**) simulated performances of the dual-band focusing reflector. Figure reproduced with permission from: (a) ref.[285], © 2014 John Wiley and Sons; (b–d) ref.[286], Creative Commons Attribution 4.0 International License; (e–h) ref.[288], © 2017 ACS.

Ma et al. stacked two independent GP metasurfaces to achieve dual-band light focusing[288]. As shown in Fig. 13(e), the metadevice was composed of two graphene nanoribbon metasurfaces with large differences in ribbon width as well as period, which ensured that the phase of the reflected light from two metasurfaces could be controlled independently from −π to π at two distinct frequencies, as shown in Fig. 13(f). The independence of the two metasurfaces could also be demonstrated by the electric field distributions at two resonant frequencies, as shown in Fig. 13(g). As a proof-of-principle demonstration, the dual-band focusing reflectors with hyperbolic phase profile were simulated. From Fig. 13(h), it can be seen that the metadevice could simultaneously operate at 16 and 25 THz with good on-axis and off-axis focusing. This work provides a general approach to design multi-band and multi-functional metasurfaces by stacking independent metasurfaces together. In 2018, a series of active wavefront control including anomalous beam steering and focusing, cloaking, and illusion optics were numerically presented by GP metasurfaces with graphene ribbons on a dielectric FP resonator, where the 2π phase requirement was achieved by interplay between GPRs in ribbons and FP resonances in the cavity resonator[289]. More recently, a meta-coupler for dynamical conversion of surface plasmons to propagating waves was reported by constructing a phase-gradient metasurface using graphene ribbons[290].

As above discussions, by tailoring the structural parameters of a single graphene antenna such as ribbon, the abrupt phase modulation of π arising from the plasmon resonance can be introduced. To extend the phase modulation to cover the entire 2π range, multiple independent resonances and coupled antenna resonances have been developed. In addition, the Pancharatnam-Berry (PB) phase based on the orientations of antennas is another efficient method, in fact a completely different one, to implement 2π phase modulation. The PB phase, or geometric phase, is associated with the space-variant conversion of polarization states following the path on the Poincaré sphere, which can be created by anisotropic subwavelength antennas with identical geometric parameters but spatially varying orientations[291]. The phase difference between the transmitted/reflected waves from any two points on the metasurface equals to one-half of the solid angle enclosed by their corresponding traces on the Poincaré sphere[292]. For the CP incident wave, the handedness of transmitted/reflected CP wave is opposite with an additional PB phase of twice the rotation angle of antenna, which means that the entire 2π phase range can be covered by only rotating antenna from 0 to 180° in metasurfaces. Currently, the PB phase has been widely developed to completely shape the wavefront of CP waves using plasmonic and dielectric metasurfaces[4,13,31,46]. Based on such PB phase principle, graphene metasurfaces have also been demonstrated to dynamically control the wavefront of CP light. In 2015, Cheng et al. proposed a graphene metasurface with periodically patterned graphene nanocrosses (as illustrated in Fig. 14(a)) to control the wavefront of CP light[77]. They found that graphene nanocrosses with different orientations could refract light into opposite helicity with uniform amplitude and 0~2π phase range, as shown in Fig. 14(b), by which dynamically tunable anomalous refraction was demonstrated. In 2018, researchers from the same group demonstrated the high-order anomalous reflection using reflection-type graphene nanocrosses metasurface[122]. By properly changing the arrangement of the nanocrosses in the metasurface, as shown in Fig. 14(c), the phase shift up to 6π (4π) could be obtained, corresponding to the 3-order (2-order) anomalous reflection with angle of 70.9° (18.6°). To validate the high-order anomalous reflection of the metasurface, 1-order, 3-order, and 15-order vortex beams were generated by arranging the nanocrosses with azimuthal phase shift as shown in Fig. 14(d). Furthermore, the dynamically-controllable efficiency of the metasurfaces was achieved by tuning the Fermi energy of graphene. In 2019, Bai et al. designed a graphene metasurface with H-shape metaatom to enable spin-dependent wavefront control based on PB phase[293]. A spin-dependent flat lens, as shown in Fig. 14(e), was realized by arranging the metaatom with different orientations. Simulation results proved that the lens exhibited interesting circular dichroism: right-handed circular polarized (RCP) light was scattered (Fig. 14(f)) while left-handed circular polarized (LCP) light was focused (Fig. 14(g)). The active control the circular polarization conversion efficiency and bandwidth was also demonstrated by tuning the Fermi energy. It should be noted that the PB phase is always related to the CP light, which is currently one of the most popular routes for spin-dependent wavefront control using metasurfaces.

Polarization control

To control the polarization state of light, the Faraday effect is a universal train of thought. In the magnetic field, Faraday rotation of several degrees in the continuous

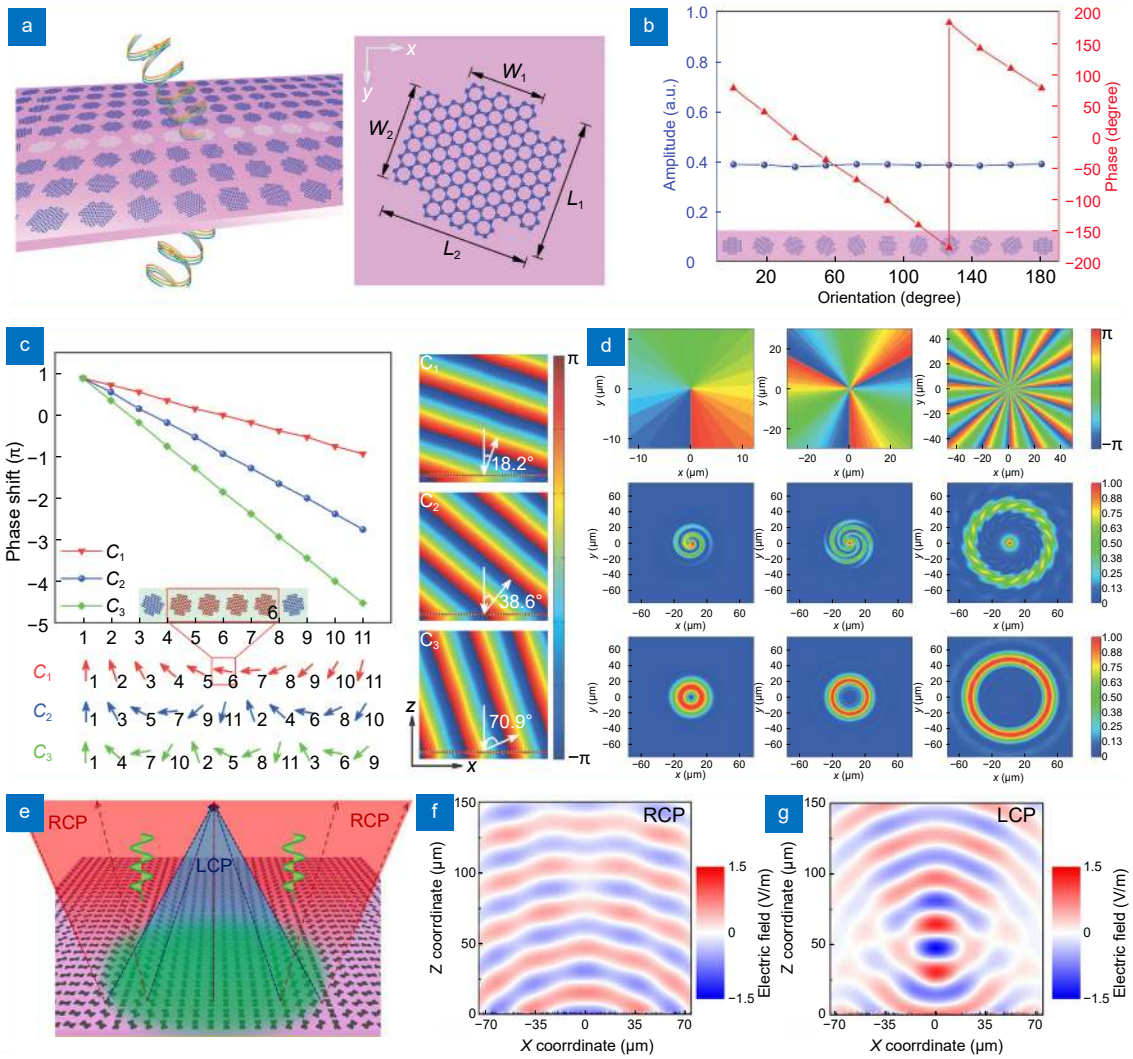

Fig. 14 | Dynamic wavefront shaping using GP metasurfaces based on PB phase. Transmission-type graphene nanocrosses metasurface: (**a**) schematic model, (**b**) transmission amplitude and phase profiles of the CP light at the frequency of 17 THz. Reflection-type graphene nanocrosses metasurface: (**c**) reflective phase shifts and simulated phase distributions of three different arrangements (C_1, C_2, and C_3), (**d**) phase distributions, interferograms, and far-field electric distributions for 1-order, 3-order, and 15-order vortex-beam-generating metasurfaces. The spin-dependent flat lens: (**e**) schematic of the flat lens metasurface, (**f**) electric field map under RCP incidence, (**g**) electric field map under LCP incidence. Figure reproduced with permission from: (a, b) ref.[77], © 2015 John Wiley and Sons; (c, d) ref.[122], © 2018 John Wiley and Sons; (e–g) ref.[293], © 2019 OSA, under the terms of the OSA Open Access Publishing Agreement.

graphene has been demonstrated experimentally by Crassee et al. in 2011[294]. Unfortunately, such giant rotation of the polarization state is typically at lower THz frequency due to the intrinsic cyclotron resonance of massless carriers and meanwhile requires giant magnetic fields, which hinder their applications. To extend the operation range and enhance the maximum rotation angle in smaller magnetic fields, creating metasurfaces with structured graphene to break the uniformity of a continuous graphene sheet has been demonstrated as an efficient way[295]. By patterning graphene into microribbon array, as shown in Fig. 15(a), Tymchenko et al. theoretically demonstrated a large Faraday rotation (more than 1°) at higher THz frequency in much smaller magnetic fields through exciting the magnetoplasmons in individual ribbons[296]. The simulated results in Fig. 15(b) and 15(c) showed the blueshifts of both peaks on transmission and Faraday rotation spectra of graphene microribbon array compared with that of the continuous graphene sheet. In 2014, Hadad et al. proposed a paradigm of graphene metasurface to enhance the Faraday rotation at magnetic field smaller than 1 T[297]. As shown in Fig. 15(d), the proposed graphene metasurface was an equivalent graphene nanodisk array by spatially

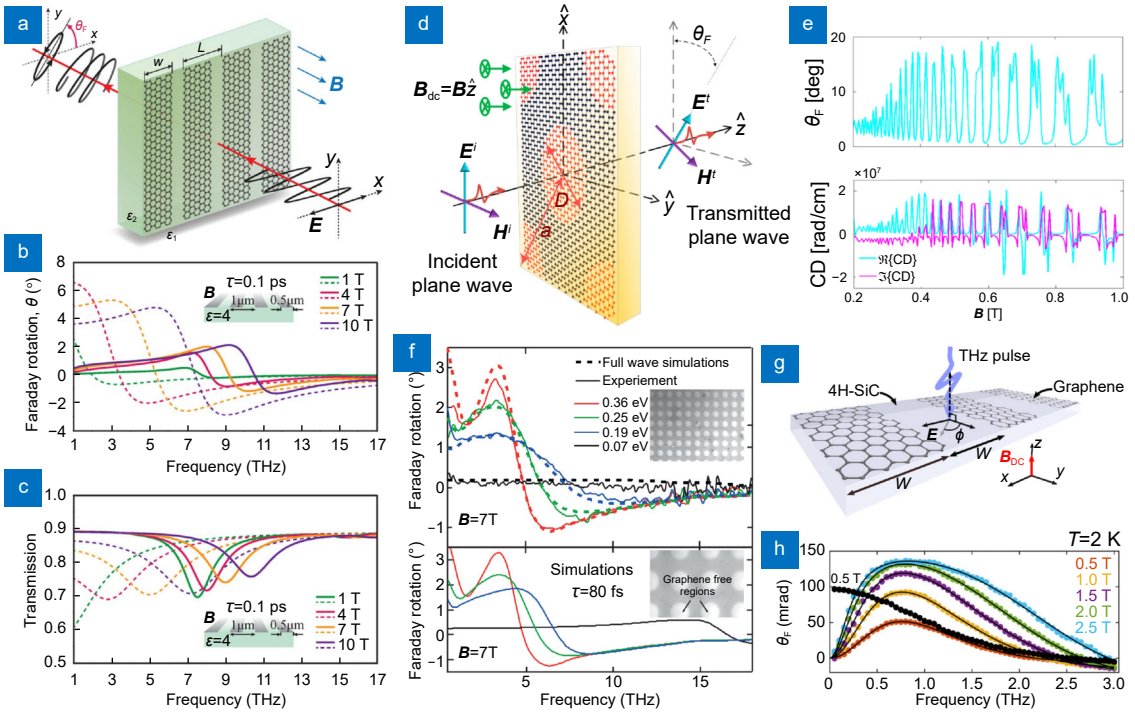

Fig. 15 | Dynamic polarization rotation in graphene metasurfaces based on the magnetoplasmon-enhanced Faraday effects. Graphene microribbon array: (**a**) schematic Faraday rotation, (**b**) Faraday rotation and (**c**) transmission spectra of ribbon arrays and continuous graphene on top of the substrate (ε=4) with relaxation time τ=0.1 ps at various magnetic fields. Equivalent graphene nanodisk array (by spatially modulating conductivity): (**d**) schematic far-field Faraday rotation, (**e**) Faraday rotation angle and (**f**) circular dichroism versus magnetic field at the frequency of 42.7 THz. (f) Measured and simulated Faraday rotation spectra of graphene square antidot (GSA) array at different magnetic fields (the inset: SEM pictures of GSA). (**g**) Schematic model and (**h**) Faraday rotation spectrum of the graphene micro-ribbon metasurface for normally incident THz pulses at different external magnetic fields. Figure reproduced with permission from: (a–c) ref.[296], © 2013 ACS; (d, e) ref.[297], © 2014 ACS; (f) ref.[298], © 2018 APS; (g, h) ref.[299], © 2020 AIP Publishing.

modulating conductivity distribution of a continuous graphene sheet. As shown in Fig. 15(e), the rotation angle of ~18° in the far-field was achieved with only ~0.3 T magnetic bias at the frequency of 45 THz. And interestingly, a strong quantization of the rotation as well as circular dichroism with magnetization was clearly observed, which is attributed to the Landau-level oscillations in the graphene metaatom, showing great potentials to enable the dynamical polarization rotator with very low magnetic bias. More recently, experiments on Faraday rotation using graphene metasurfaces made a breakthrough in the THz regime. In 2018, Tamagnone et al. designed and fabricated three different graphene metasurfaces, that is, a periodic array of graphene square dots, a graphene square antidot lattice (shown in the inset of Fig. 15(f)), and a hybrid metal-graphene patterned structure, where the magnetoplasmons induced blueshift of the Faraday rotation was confirmed experimentally[298]. The strong tunability of the Faraday rotation was also demonstrated using both electric and magnetic fields, and the Faraday rotation spectra at different Fermi energies were plotted in Fig. 15(f) for graphene square antidot lattice. In 2020, Padmanabhan et al. reported a graphene microribbon metasurface (Fig. 15(g)) to dynamically control the transmission and polarization rotation of linearly polarized THz pulses[299]. The tunable Faraday rotation with the external magnetic field and ribbon pattern could be observed in Fig. 15(h). The possibility to control the Faraday rotation and frequency by geometry-engineering, external magnetic and/or electric fields using graphene metasurfaces demonstrated by these important progress holds an exciting promise for dynamical rotating the polarization states of light.

Apart from the Faraday effect, polarization-dependence of the plasmon resonances in structured graphene has already been exploited to implement dynamic polarization control. Due to the geometric symmetry, plasmon resonances in graphene disk and ring are polarization-independent. While for asymmetric graphene structures such as ribbon, rectangle, ellipse, and cross the plasmon resonances are highly sensitive to the polarization state of incident light. In 2013, Cheng et al.

proposed a MIR tunable polarization converter by using asymmetric graphene nanocrosses[300]. As shown in Fig. 16(a), the transmission coefficients and phase retardation of the *x*- and *y*-polarized transmitted waves were highly related to the polarization states of excited waves. When the phase retardation difference between them is exactly 90°, as shown in Fig. 16(b), the linearly polarized light can be converted into the circularly or elliptically polarized light, and also can be rotated with an angle when the phase difference is zero. Meanwhile, the wavelength and polarization states of the transmitted light can be dynamically tuned by controlling the Fermi energy of graphene. On the basis of such principle, various dynamically tunable polarization converters were demonstrated using graphene metasurfaces based on L-shaped graphene nanostructures (Fig. 16(c))[301], rectangular graphene patches (Fig. 16(d))[302], and graphene nanoribbons[303]. In 2018, Panoiu et al. realized a tunable THz polarization converter by two crossed graphene nanoribbon gratings[304]. As shown in Fig. 16(e), the *x*- and *y*-polarized incident wave was reflected by the bottom and top graphene grating respectively, and the phase difference of them can be controlled by the thickness of the insulator spacer. Thus, the proposed metasurface can effectively generate linearly, circularly, and elliptically polarized THz waves.

Frequency conversion

On the way to seek nonlinear materials with low threshold and ultrafast response time, plasmonic nanostructures have been particularly attractive because of their ability to enhance the electric field intensity near nanostructures, such as noble metal nanoparticles and metasurfaces. Although the third-order nonlinear effects including four-wave mixing (FWM), Kerr effect, and third-harmonic generation have been experimentally confirmed in the undoped graphene, even-order nonlinear processes are always forbidden because graphene is a centrosymmetric atomic crystal. To exploit the even-order nonlinearity, Cox and García de Abajo demonstrated theoretically that graphene nanoislands could be an ideal platform for developing the electrically-tunable

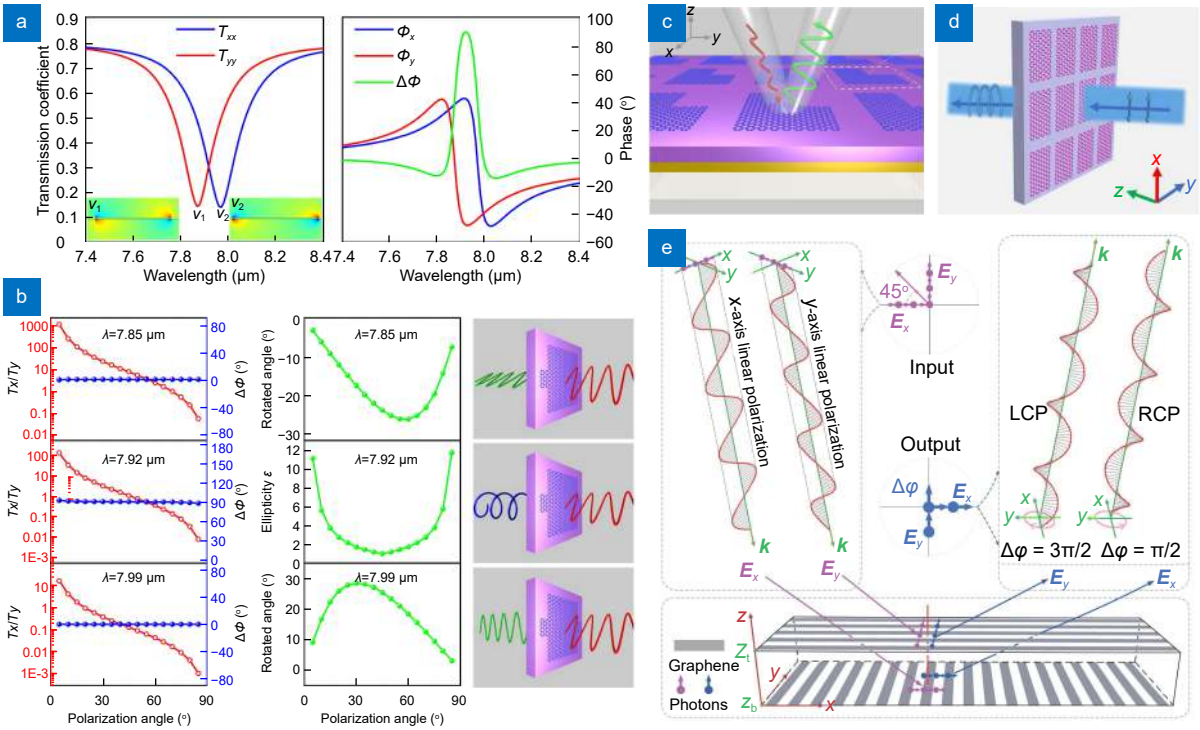

Fig. 16 | Dynamic polarization conversion in GP metasurfaces based on polarization-dependent plasmon resonances. Asymmetric graphene nanocrosses metasurfaces: (**a**) transmission coefficients and phase difference excited by linearly polarized light, (**b**) transmission amplitude ratio, phase difference, rotated polarization angle, and ellipticity versus the incident polarization angle at three wavelengths. (**c**) L-shaped graphene nanostructures. (**d**) Rectangular graphene patches. (**e**) The operation principle of the polarization converter based on crossed-graphene ribbon gratings. Figure reproduced with permission from: (a, b) ref.[300], © 2013 OSA, under the terms of the OSA Open Access Publishing Agreement; (c) ref.[301], © 2013 AIP Publishing; (d) ref.[302], © 2016 OSA; (e) ref.[304], © 2018 OSA, under the terms of the OSA Open Access Publishing Agreement.

nonlinear nanodevices[305]. As shown in Fig. 17(a) and 17(b), the centrosymmetry of graphene was broken when patterned into nanoisland due to the finite-size effect, and graphene dipole was induced by the incident electric field. When the incident light is polarized along *x* direction, only odd harmonics are generated, which results from the mirror symmetry of the nanoisland along that direction. Interestingly, for the incident light polarized along asymmetric *y* direction, both odd and even harmonics can be observed, as shown in Fig. 17(c). Such kind of nonlinear optical polarizabilities of graphene nanoislands are several orders of magnitude larger than those of metal nanoparticles with similar thickness. By exploiting the localized plasmons in doped graphene nanostructures such as nanoislands and nanoribbons, plasmon-assisted nonlinear wave mixing[306,307], including high-harmonic generation[308], sum and difference frequency generation as well as FWM[309], have been successively revealed in graphene metasurfaces. More recently, Panoiu et al. designed a specific graphene metasurface to construct a wide topological bandgap at THz frequency in a static magnetic field and demonstrated a topologically protected FWM process of plasmonic edge states in the bandgap[127]. As shown in Fig. 17(d), the proposed metasurface consisted of a periodic nanohole array in a graphene sheet, which results in a topological bandgap and hence topologically protected one-way edge plasmons. It can be seen from the near-field profiles at the frequencies of signal and idler, plotted in Fig. 17(e) and 17(f), that the signal is amplified during propagation, whereas an edge mode is generated at the idler frequency. Notably, both signal and idler modes exhibit

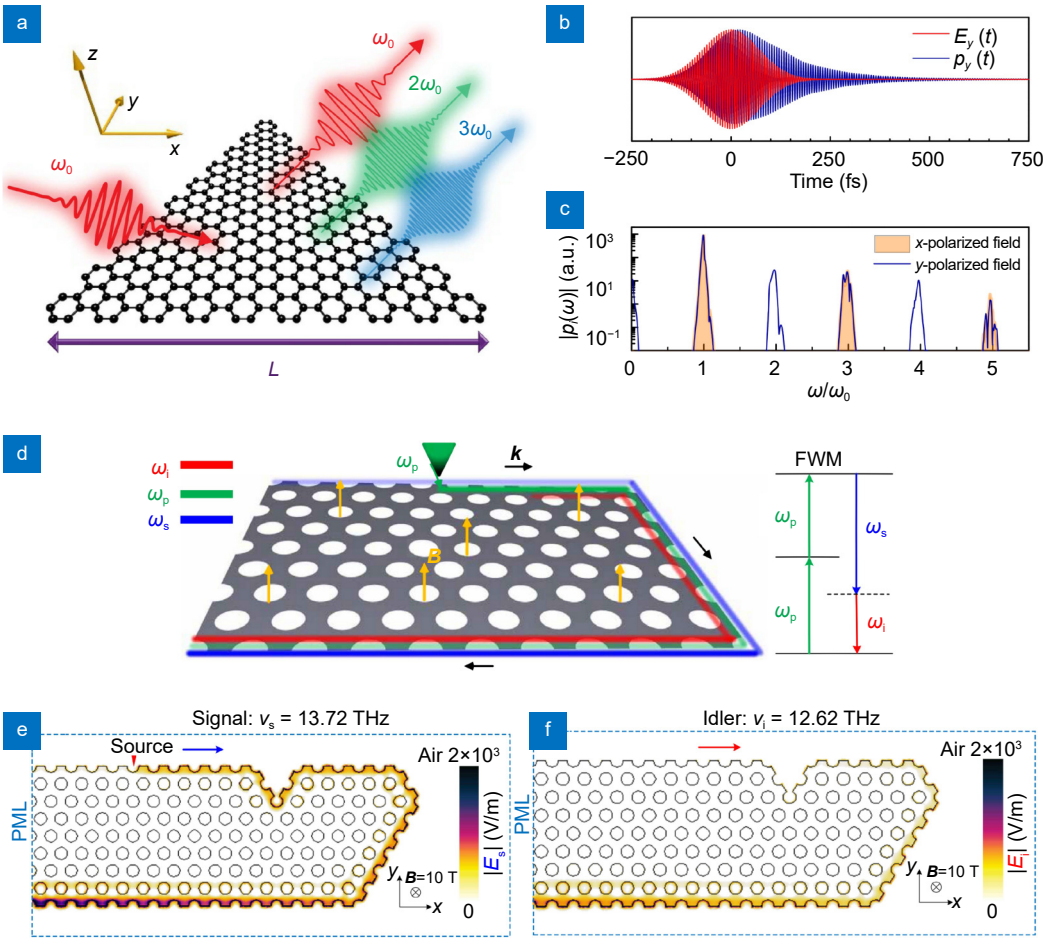

Fig. 17 | Dynamic nonlinear frequency conversion using GP metasurfaces. Harmonic generation in the armchair-edged triangular graphene nanoislands: (**a**) illustration of nanoisland and harmonic generation, (**b**) time-varying graphene dipole induced by the electric field of incident pulse, (**c**) excitation of harmonics for incident pulses with polarizations along the *x* and *y* directions. Topologically protected FWM interactions in a specific graphene metasurface: (**d**) configuration of a periodic nanohole array in a graphene sheet and FWM of topologically protected one-way edge plasmons, near-field profiles at the frequencies of signal (**e**) and idler (**f**). Figure reproduced with permission from: (a–c) ref.[305], © 2014 Springer Nature; (d–f) ref.[127], © 2020 The authors, under a Creative Commons Attribution License 4.0 (CC BY).

unidirectional and defect-immune propagation along the edge of metasurface, indicating that the FWM process is topologically protected. They proved that the effective nonlinear coefficient of the proposed graphene metasurface is about 10 orders of magnitude larger than that of highly nonlinear silicon photonic nanowires.

Dynamic surface EM wave manipulations

As discussed in Section *Theoretical and numerical models of GPs*, graphene shows good energy confinement and guidance of propagating GPs, and has been demonstrated as a one-atom-thick platform for 2D nanophotonic waveguides in the MIR and THz frequencies. Furthermore, the spatial conductivity patterning method proposed by Vakil and Engheta provides an efficient way to actively guide and manipulate the GPs propagating along with graphene sheet, which has attracted increasing attention of researchers in the nanophotonics community[310]. In fact, this method was initially adopted to create functional GP-waveguide devices by implementing special gate-voltage scheme or directly patterning the Fermi energy of graphene. For example, GP-waveguide switches at NIR frequency were achieved by selectively enabling or forbidding propagation of GPs[311]; THz GP-waveguide array was proposed with negligible crosstalk by patterning the ferroelectrics into parallel- and antiparallel-poling configurations, which can induce drastically different carrier densities at the different domain of graphene sheet[221]; Nanofocusing of propagating GPs on graphene sheet in the MIR band was realized by using spatially gradient chemical potential[220].

For more complex manipulation of propagating GPs on graphene, the metasurface concept has been introduced into the 2D GP-waveguide system. According to the spatial conductivity patterning method, the capacitor model is the fact of the matter. By using a silicon-based grating structure as the ground plate of the graphene-silica-silicon capacitor, as shown in Fig. 18(a) and 18(b), we demonstrated a 1D graphene Bragg grating metasurface to selectively reflect and slow-down the propagating GPs[312]. Figure 18(a) shows the schematic model of the proposed graphene metasurface, in which the groove grating silicon plate plays a vital role in spatially modulating the conductivity of graphene sheet. When a gate voltage is applied between graphene sheet and silicon plate, the conductivity distribution immediately changes from uniform to nonuniform with the pattern similar to the groove grating silicon plate, which in turn manipulates the propagating GPs along with graphene sheet according to the Eq. (12). By this means, a suitable setting of grating silicon plate with Bragg scattering condition can finally induce a periodic modulation of the effective refractive index for propagating GPs as that of conventional fiber Bragg grating, and thus gate-voltage tunable reflection of propagating GPs is implemented. To broaden the operation bandwidth of frequency, a graded grating silicon plate is introduced as illustrated in Fig. 18(a). The propagating GP waves at wavelengths of 8.0, 8.5, and 9.0 μm are trapped at different positions, namely "rainbow trapping", and finally reflected back to the incident port, as shown in Fig. 18(b). Interestingly, the group velocity of the propagating GPs could be slow-downed greatly at the trapping position, corresponding to the cutoff frequency of GP grating. It should be noted that, the trapped propagating GP waves can also be released by tuning the gate-voltage, and hence their group velocity can be controlled dynamically. Shi et al. has well analyzed the above performance from the viewpoint of energy band in graphene plasmonic crystals with periodically modulated chemical potential in graphene[313]. According to the Eq. (5), it is found that besides the conductivity of graphene, the dielectrics surrounded graphene sheet drastically affect the propagation constant (or mode index) of the propagating GPs, which provides an alternative method to manipulate the energy flow of the propagating GPs. To implement this idea, we proposed a versatile scheme to design GP metasurface based on the effective medium theory (EMT)[263]. As illustrated in Fig. 18(c), the fundamental configuration of the metasurface is composed of a single-layer graphene and a specific photonic crystal (PC)-like dielectric layer, where periodically arranged two dielectrics with unequal permittivity lead to the mode index modulation of the propagating GPs. On the basis of the EMT, this metasurface can be equivalent to a new material with a global index profile determined by the filling factor of two dielectrics. To demonstrate the feasibility and versatility of the proposal, 2D radial and axial gradient-index (GRIN) lenses in the THz regime were numerically implemented as diverse as Maxwell's Fisheye lens, Luneburg lens, and self-focusing lens, as shown in Fig. 18(d–f) respectively, which can work perfectly well for focusing the GP waves. It can be seen from Fig. 18(g) and 18(h) that the focusing spot was as small as one-sixtieth of the wavelength of excitation light in vacuum and meanwhile could be dynamically tuned by gate voltage, indicating the excellent performances of deep-subwavelength scale and broadband electrical tunability. More importantly, arbitrary metasurfaces with GRIN index profiles could

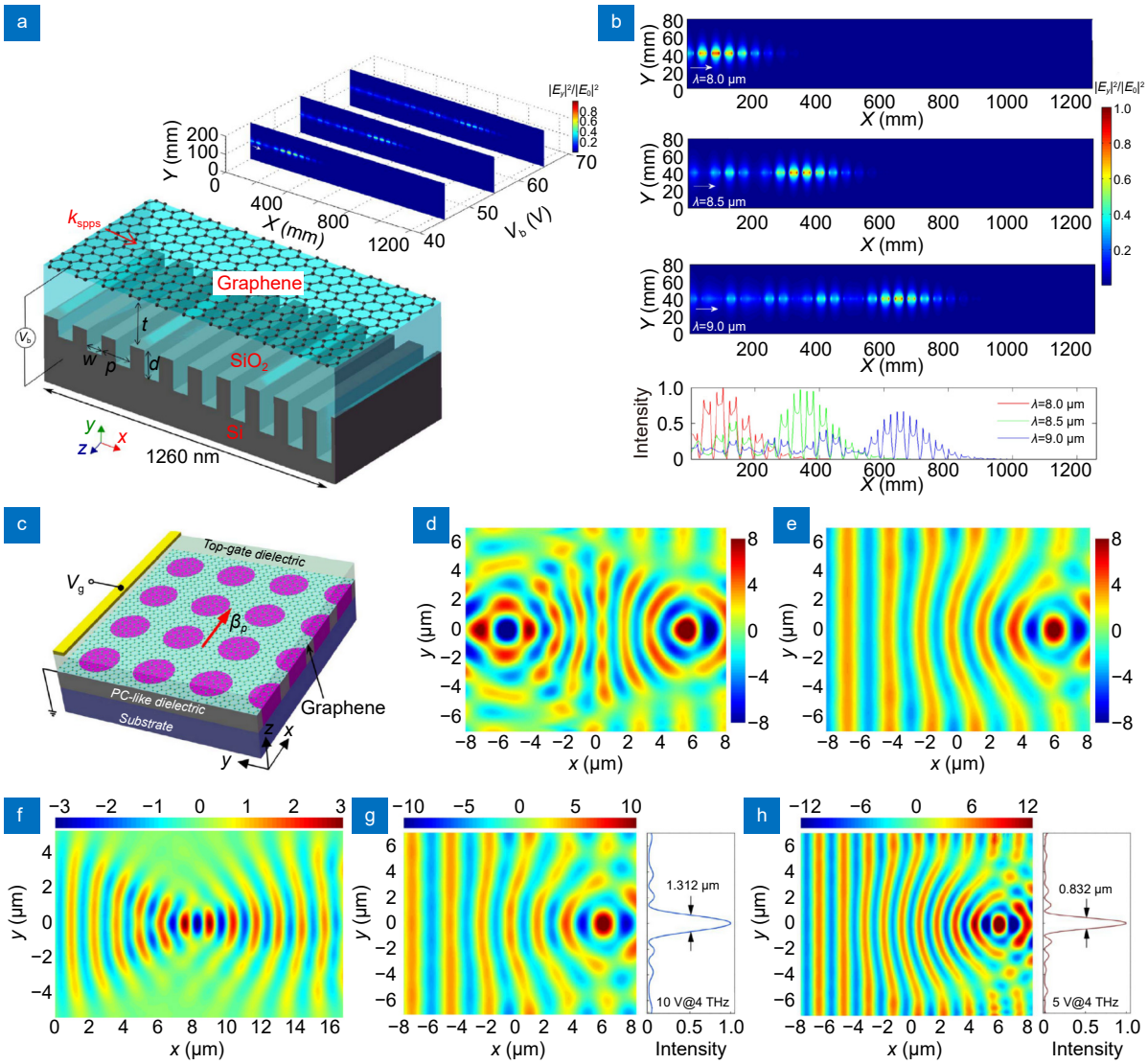

Fig. 18 | Dynamic trapping and focusing of GP waves propagating along the 2D plane of graphene sheet using GP metasurfaces. GP metasurface with a groove grating silicon as the ground plate of the parallel capacitor: (**a**) schematic model with a graded grating silicon plate, (**b**) electric fields of GP waves for different wavelengths. GP metasurface with PC-like dielectric layer underneath graphene sheet: (**c**) fundamental structure model, field distributions of Maxwell's Fisheye lens (**d**), Luneburg lens (**e**), self-focusing lens (**f**), and Luneburg lens at different gate voltages (**g**) and (**h**). Figure reproduced with permission from: (a, b) ref.[312], 2015, (c–h) ref.[263], 2014, under a Creative Commons Attribution 4.0 International License.

be projected through the proposed method, which shows great potentials in developing more active 2D transformational plasmonic devices.

Based on the similar method, in 2019, Basov et al. experimentally demonstrated a broadly tunable 2D PC platform for on-chip plasmonic manipulation using graphene metasurface, which consisted of a hBN encapsulated single-layer graphene on top of a hexagonal lattice array of SiO_2 pillars, as shown in Fig. 19(a) and 19(b)[314]. Due to the presence of the patterned substrate underneath, the conductivity of graphene was unequal between regions above the pillars and voids in SiO_2 and underwent the periodic spatial modulation, which therefore prompted the formation of a 2D Brillouin zone and a plasmonic band structure with an evident bandgap, as shown in Fig. 19(c). By introducing a shift dislocation of the hexagonal lattice, a domain wall was engineered as shown in Fig. 19(b). The near-field imaging of GP waves in Fig. 19(d) visualized both propagating and localized GP waves as a function of gate voltage: at V_g=−40 V, only faint plasmonic fringes were observed; at V_g=−60 V, the hexagonally-patterned dark spots emerged; at V_g=−70 V, an 1D plasmonic mode was confined to the domain wall; at V_g=−90 V, launched GP waves propagated along the

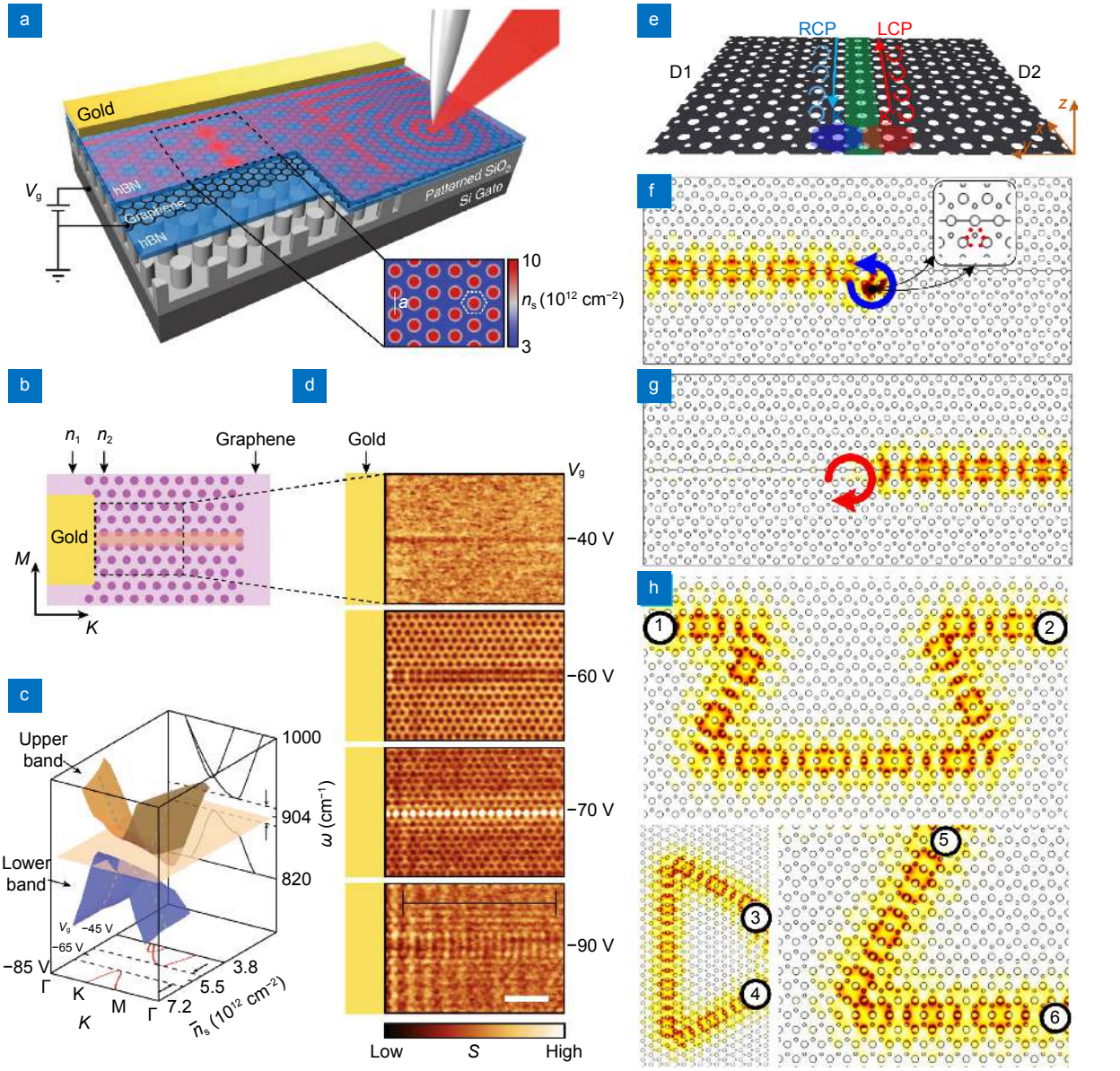

Fig. 19 | Dynamic guiding of GP waves propagating along the 2D plane of graphene sheet using GP metasurfaces. GP metasurface with patterned substrate underneath a fully encapsulated graphene sheet: (**a**) schematic configuration, (**b**) schematic metasurface with an engineered domain wall, (**c**) calculated plasmonic band structure, (**d**) experimental near-field images at different gate voltages. GP metasurface with periodically patterned air nanoholes in a graphene sheet: (**e**) schematic of GP metasurface waveguide by mirror-symmetrically putting two optimized GP metasurfaces together, unidirectional mode propagations of RCP (**f**) and LCP light (**g**), backscattering-immune propagations in U-, C-, and L-bend domain-wall interfaces (**h**). Figure reproduced with permission from: (a–d) ref.[314], 2019, under a Creative Commons Attribution 4.0 International License; (e–h) ref.[315], © 2020 IEEE.

PC. This work provides not only an experimental evidence to construct graphene metasurfaces using the spatial conductivity patterning method, but also a viable platform for electrostatically-tunable manipulating plasmonic waves in the 2D plane. Based on the energy band theory, in 2020, Panoiu et al. proposed a specific graphene plasmonic crystal metasurface to implement the unidirectional and backscattering-immune waveguiding of GP waves in the 2D plane[315]. As illustrated in Fig. 19(e), the proposed metasurface comprised of periodically patterned air nanoholes in a graphene sheet, by which the gapless Dirac cone of graphene was opened and consequently a topological bandgap occurred. And further, a domain-wall interface in the proposed metasurface waveguide was constructed by putting two optimized graphene metasurfaces together in a mirror-symmetric manner, resulting in a plasmonic edge mode inside the bandgap. Numerical results, as shown in Fig.

19(f–h), revealed their typical topological propagation features: unidirectional propagation of GP waves for RCP and LCP excitation light and backscattering-immune propagation in U-, C-, and L-bend domain-wall interfaces.

Hybrid metasurfaces integrated with graphene

Although the manipulations of amplitude, phase, and polarization of EM waves have been well studied using metallic and dielectric metasurfaces, such manipulations are usually passive with the before-fabrication variation of the size, shape, and material properties of the metaatoms and metasurfaces. Beyond patterning graphene into plasmonic nanostructures as aforementioned discussions, integrating graphene with passive metasurfaces is another mainstream route to enable dynamically tunable functionalities due to the fairly mature fabrication processes and larger degrees of freedom for 3D bulky materials (such as metals and dielectrics) when compared with 2D materials (such as graphene). As discussed in Section *Basic material properties of graphene*, the surface conductivity (or dielectric function, or surface resistance) of graphene is electrically tunable with great ease via an external electric field, which is rather attractive for empowering activity to passive metasurfaces and metadevices. In general, the dynamic tunability of a conventional passive metasurface can be actualized by putting an electrically-controlled graphene layer in its proximity, which significantly influences the EM response of the metasurface usually ultra-sensitive to the surrounding environment where graphene locates. In 2012, Min et al. experimentally demonstrated a gate-controlled graphene-integrated metasurface to dynamically modulate both the amplitude and phase of THz wave, and due to the strong coupling of graphene with metaatoms the measured maximum values of amplitude and phase changes exceeded 47% and 32.2° respectively[74]. At the same time, Boltasseva et al. experimentally demonstrated the electrical control of the plasmonic resonances in an infrared regime by fabricating metal nanostructures on a voltage-controlled graphene layer, which largely enhanced the light-graphene interaction and in turn strongly impacted the damping of plasmonic resonances[316]. In 2013, Capasso et al. demonstrated the electrical tuning of plasmonic resonances using graphene-loaded antennas over a broad wavelength range of 650 nm at the MIR frequencies[317]. In 2015, Khanikaev et al. introduced a theoretical model for enhancing the nonlinear response of graphene through graphene-integrated plasmonic metasurfaces, which numerically proved the tunable nonlinear frequency conversion[318]. Inspired by those works, the combination of graphene and metallic structures including metasurfaces emerges as a wonderful platform for exploiting electrically-controlled nanodevices[319–327]. Tremendous attention have been paid to the graphene-hybrid metasurfaces for dynamically EM wave manipulating[328–330]. For such hybrid metasurfaces, their manipulations of amplitude, phase, and/or polarization of EM waves mainly depend on metasurfaces and graphene in general propels such manipulations from static to dynamic. In this Section, graphene-hybrid metasurfaces are distinguished with respect to their control manners with graphene including the global and local ways. Several typical examples on homogeneous metasurfaces and digital coding metasurfaces are discussed in detail based on globally- and locally-controlled graphene, respectively.

Homogeneous metasurfaces based on globally-controlled graphene

Homogeneous metasurface refers to the metasurface in which its metaatoms are simultaneously controlled by one graphene layer, which results in the global-controlled response of all metaatoms when gate voltage is applied. Here, dynamic spectrum modulations related to amplitude change and frequency shift are presented first. To explore a high-speed and high-contrast amplitude modulator, Yao et al. proposed an electrically-tunable MIR perfect absorber by incorporating a graphene-integrated metasurface into a subwavelength-thick optical cavity, as shown in Fig. 20(a), which could be regarded as an asymmetric FP resonator with a metallic fully reflecting mirror in the back and a tunable partially reflecting mirror (i.e. graphene-integrated metasurface)[75]. The metasurface was composed of laterally coupled antennas on a whole graphene sheet, which was employed to control the critical coupling condition of the metasurface absorber via the gate voltage. Figure 20(b) showed the blue shifts of reflection spectra with the gate voltage increasing in the MIR regime. It can be seen that when the gate voltage was 40 V, the reflectance dip reached its lowest value around the wavelength of 6.3 μm, resulting in the modulation depth of more than 95% around this wavelength. Furthermore, the speed of the proposed modulator was estimated up to 20 GHz (limited by detector), which was attributed to the high conductivity and short optical response time of graphene. In the THz regime, the electrically-tunable perfect absorption has more recently been demonstrated through integrating a

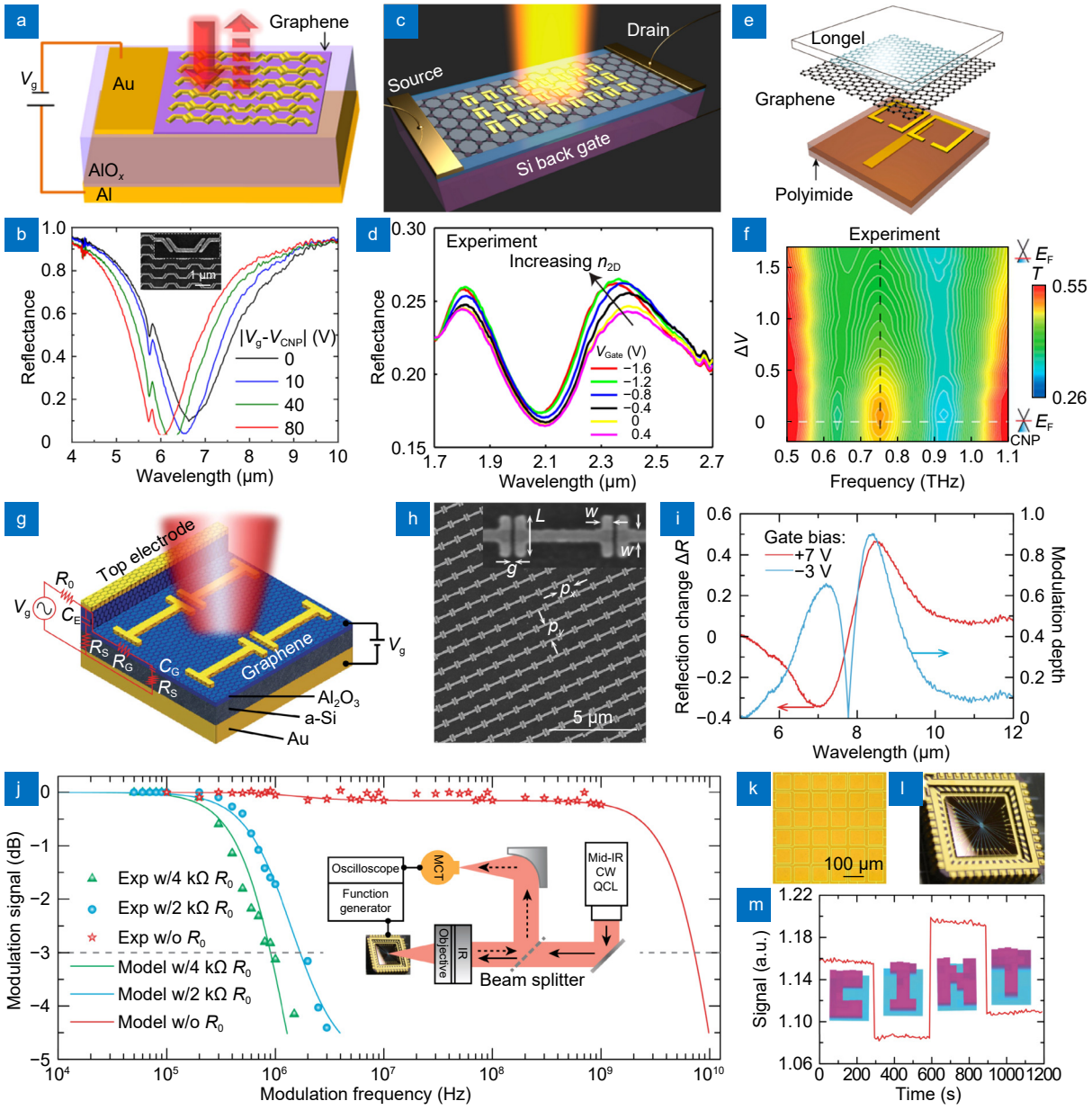

Fig. 20 | Dynamic spectrum modulations using graphene-hybrid metasurfaces. Ultrathin MIR amplitude modulators based on electrically tunable metasurface perfect absorber: (**a**) schematic of metasurface modulator comprising plasmonic structures on graphene, (**b**) measured reflection spectra for different gate voltages (inset: SEM image of the metasurface on graphene). Electrical modulation of Fano resonance in plasmonic metasurface using graphene: (**c**) schematic illustration of the Fano resonant metasurface fabricated on top of graphene with Si back gate, (**d**) measured reflectance spectra of the metasurface with ion-gel top electrolyte at different gate voltages. Electrically tunable EIT and slow light using diatomic metasurface integrated with a gated graphene: (**e**) schematic view of gate-controlled EIT metasurface, (**f**) measured transmission spectra as a function of gate voltage variation. Hybrid graphene metasurfaces for SLM: (**g**) schematic of the metasurface, (**h**) SEM image, (**i**) reflection change and modulation depth as functions of wavelength at gate biases of 7 V (red curve) and -3 V (blue curve), (**j**) modulation speed (inset: measurement system) of the SLM, (**k**) optical micrograph of 6×6 functional pixels, (**l**) photograph of the device, (**m**) spatial reflection patterns of "CINT" by selectively applying gate voltages to individual pixels. Figure reproduced with permission from: (a, b) ref.[75], © 2014 ACS; (c, d) ref.[332], © 2014 ACS; (e, f) ref.[335], © 2018 ACS; (g–m) ref.[337], under a Creative Commons Attribution 4.0 International License.

metallic grating onto graphene Salisbury screen by Zhang et al.[331]. To implement ultrahigh-performance amplitude modulations, successively, Fano resonance and classical analogue of EIT using metal nanostructures exhibited the great promise due to their remarkable features of large sensitivity to the local environment[332–336]. In 2014, Emani et al. integrated a Fano metasurface on a gated-graphene, as shown in Fig. 20(c), and demonstrated the continuously dynamic control of Fano resonances at NIR frequencies (Fig.

20(d))[332]. On the basis of the EIT metasurface hybridly integrated with graphene, in 2018, Kim et al. demonstrated the dynamically-controlled EIT spectra and group delay of THz waves, as shown in Fig. 20(e) and 20(f)[335]. More recently, Zeng et al. presented the experimental demonstration of a prototype MIR spatial light modulator (SLM) based on dynamic amplitude modulation using graphene-hybrid metasurface[337]. Figure 20(g–i) showed the structural model of the proposed metasurface, SEM image of the fabricated sample, and measured electrically-tunable resonant absorption, respectively, revealing the maximum reflection change of 46.7% and modulation depth exceeding 90% around the wavelength of 8.5 μm. In addition to the high modulation depth, the measured modulation speed was as high as 1 GHz, and the intrinsic modulation speed was inferred to be ~7.2 GHz, as illustrated in Fig. 20(j). Finally, a MIR SLM prototype metadevice with 6×6 functional pixels, shown in Fig. 20(k) and 20(l), was fabricated for high frame rate single-pixel imaging by independently switching "ON" and "OFF" the individual pixels through the gate voltages. Clear visualization of the mask patterns "CINT " validated the imaging capability of the SLM, which provides a new scheme to overcome the modulation speed limitation of the traditional liquid crystal and micromirror-based SLMs.

For the phase manipulations, in fact, the aforementioned amplitude manipulations are at the same time accompanied by the phase manipulation due to the electric or magnetic resonances in metasurfaces. This resonance-induced phase retardation has been widely employed to realize dynamic phase modulation of EM waves by a variety of gate-controlled graphene metasurfaces. For instance, Zhou et al. proposed a gate-graphene magnetic resonant metasurface to achieve widely tunable phase modulation of reflected THz waves, where graphene was utilized as a tunable loss to drive the coupling behavior in metasurface[338]; Shvets et al. demonstrated the 55° phase control of the reflected MIR light while maintaining the amplitude constant using a plasmonic metasurface integrated with a graphene sheet[339]; Atwater et al. reported up to 237° phase modulation range using electronically reconfigurable graphene-gold resonator metasurfaces[340]. Besides the above-discussed resonance phase, the PB phase has been extensively investigated to conceive metallic and dielectric metasurfaces for phase manipulation due to its advantages of broadband operation, easy access and large tolerance of design[29,46,341,342]. Recently, integrating graphene with those metasurfaces based on PB phase renders the phase manipulation more active, enabling the dynamic wavefront control. In 2017, Zhang et al. demonstrated the graphene-integrated metasurfaces and metalens based on PB phase for actively modulating the electric-field amplitude (or intensity) of anomalously refracted THz waves[343]. The demonstrated active metasurface consisted of a graphene sheet deposited on the array of U-shaped apertures, as shown in Fig. 21(a), which acted as an active circular polarization converter: a normally incident LCP wave could be converted into the RCP wave. Figure 21(b) showed the full-wave simulation result of gate-controlled modulation on anomalously refracted waves from the metasurface with a linear PB phase profile. It can be seen that, as a result of the in-plane PB phase gradient, a titled wavefront was clearly observed and also the amplitude of electric field distribution in the refracted direction could be actively controlled through the applied voltage, which was further proved by experiments. They went a step further to numerically demonstrate a dynamically tunable metalens by the spatially parabolic phase profile design, as shown in Fig. 21(c), with which the incident THz waves could be focused and electrically controlled. The simulation results in Fig. 21(d) revealed that when the gate voltage was 2.2 V the wavefront of transmitted RCP waves could be converged well at focal point while the electric-field amplitude and energy density at the focal point was significantly reduced when gate voltage decreases to zero. In 2018, a focal length-tunable metalens was demonstrated experimentally with a graphene-integrated PB phase-based metasurface by Hu et al.[344]. As shown in Fig. 21(e) and 21(f), the proposed metalens was mainly composed of a gated-graphene and a gold film etched with rectangular aperture antennas, in which each antenna had different rotation angles to actualize the desired phase profile of metalens, as plotted in Fig. 21(g). The geometric parameters of the designed metalens were presented in Fig. 21(h) and 21(i), where different aperture lengths were introduced to compensate for the phase change aroused from the influence of the chemical potential variation of graphene by the applied gate voltage. The experimental observations of the tunable intensity and phase distribution with gate voltages gave evidence for the capability of the proposed metalens to electrically modulate the wavefront of CP THz waves. The far-field intensity distribution in the axial plane, illustrated in Fig. 21(j) and 21(k), calculated from the measured intensity and phase in the imaging plane clearly showed the dynamic tuning of focal length as large as ~2 mm by the gate voltage.

Similar to the aforementioned dynamic amplitude and phase manipulations, dynamic manipulation of the po-

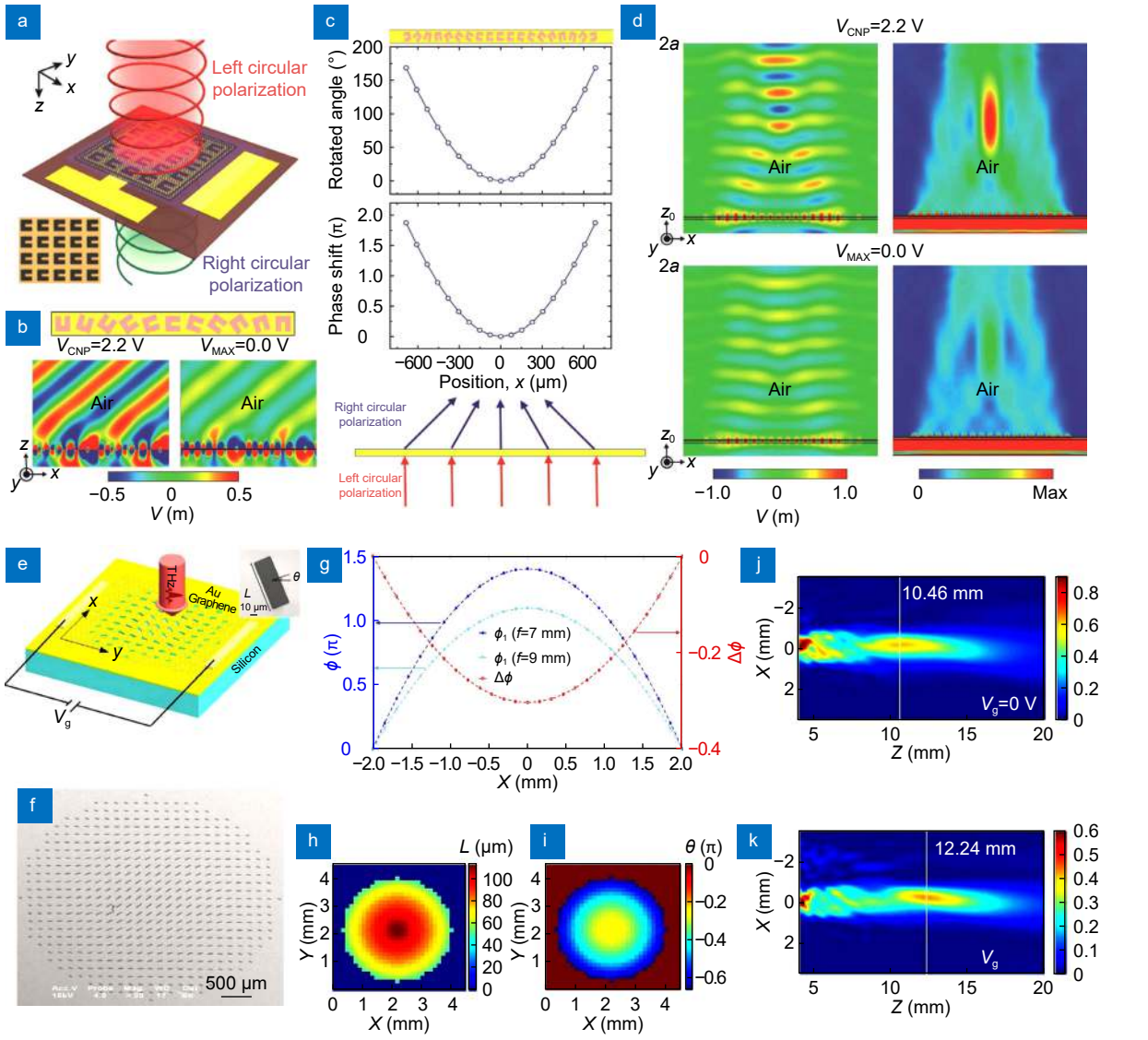

Fig. 21 | Dynamic wavefront control using graphene-hybrid metasurfaces. Electrically modulation of anomalously refracted THz waves with gated-graphene metasurfaces: (**a**) schematic view of the crosspolarized transmission in graphene metasurfaces consisting of a graphene sheet deposited on the array of U-shaped apertures (inset: optical micrograph image), (**b**) schematic of the metasurface with linear phase variation and the simulated wavefront control for LCP incidence at different gate voltages, (**c**) metasurface with parabolic phase profile for focusing THz waves, (**d**) electrically modulations of electric field and energy density of focusing performances. Graphene-enabled electrically controlled THz metalens: (**e**) schematic of the active THz metalens composed of an Au metasurface and a graphene layer, (**f**) SEM micrograph of the fabricated metalens, (**g**) phase distributions of metalens with focal lengths of 7 mm and 9 mm and their phase difference, (**h**) length *L* and (**i**) rotation angle *θ* distributions of the metalens, (**j**) and (**k**) far-field intensity distributions of the transmitted RCP THz waves at gate voltages of 0 and 2 V respectively. Figure reproduced with permission from: (a–d) ref.[343], © 2017 Wiley; (e–k) ref.[344], © 2018 Chinese Laser Press.

larization state using graphene-hybrid metasurfaces has attracted enormous interest. To manipulate the polarization state, the anisotropy of metasurfaces plays a dominant role, in which the different responses along orthogonal principal axes of the metaatoms lead to different amplitude attenuation and phase retardation of the incident EM waves[345–347]. Therefore, the polarization state can be controlled with great ease through carefully engineering the geometries of metaatoms, and further dynamic control of the polarization state can be realized by integrating gate-graphene with metasurfaces, where graphene is often deposed in hot spots created by metasurface to actively adjust the anisotropic responses of metasurfaces, i.e. tuning the amplitude attenuation and phase retardation. On the basis of this principle, Tian et al. proposed a metadevice by integrating graphene with an anisotropic metasurface, as shown in Fig. 22(a), which can dynamically modulate the polarization state of MIR

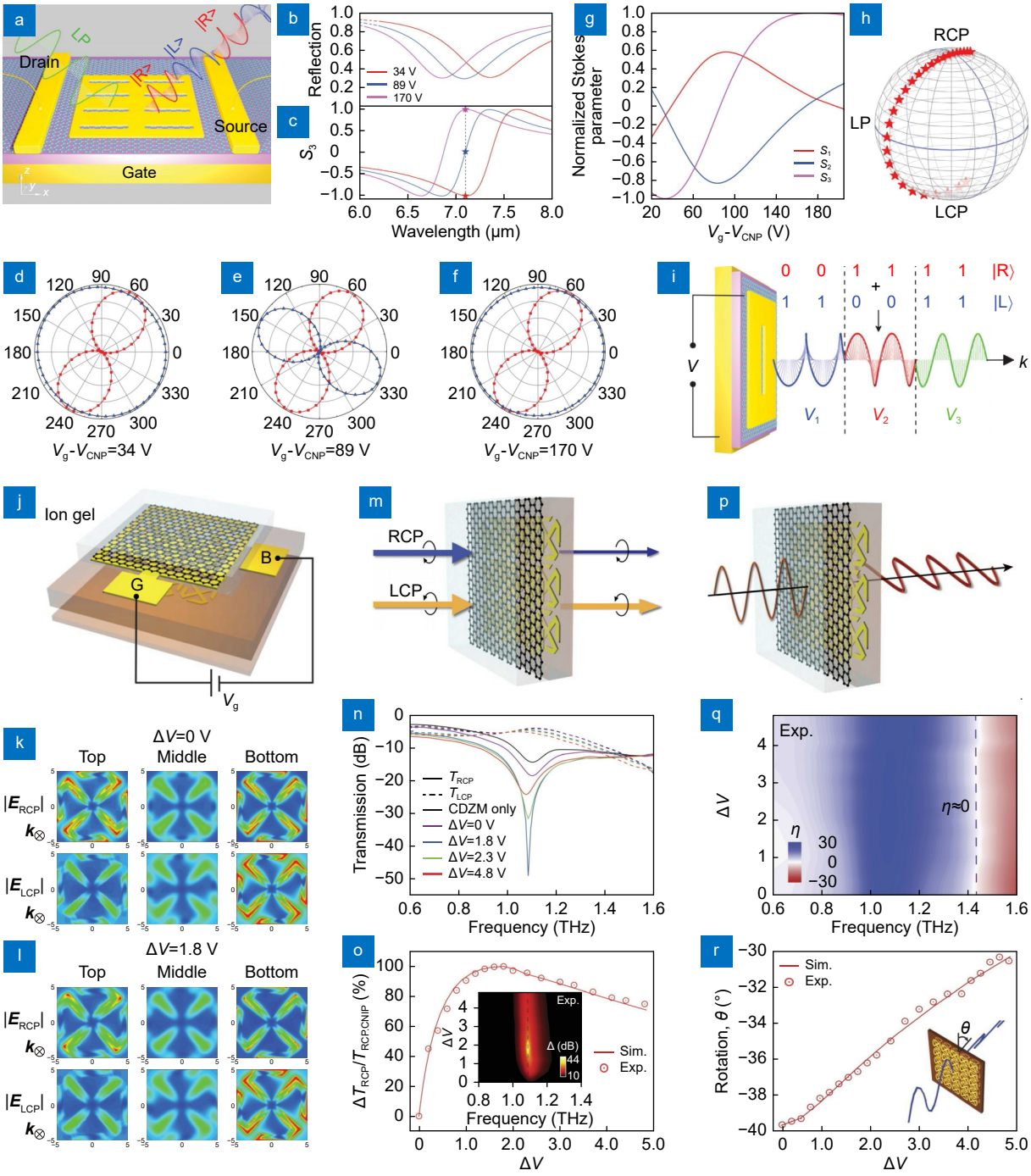

Fig. 22 | Dynamic polarization control using graphene-hybrid metasurfaces. Mid-infrared optical polarization encoding using graphene-integrated plasmonic metasurfaces: (**a**) schematic illustration of the polarization encoding process based on the circular orthogonal polarization basis, (**b**) and (**c**) reflection and normalized Stokes parameter S_3 spectra at different gate voltages as functions of wavelength, (**d**-**f**) polarization states of the reflected light under linearly polarized incident light at three different gate voltages, (**g**) normalized Stokes parameters (S_1, S_2, S_3) as a function of gate voltage, (**h**) corresponding polarization states on the Poincaré sphere, (**i**) schematic illustration of the PDM technique realized by the proposed metadevice. Electrical tuning of the polarization state of THz waves using graphene chiral metasurfaces: (**j**) schematic rendering of the conjugated double Z metasurface with the ion-gel gate, (**k**) and (**l**) electric field distributions for RCP and LCP in the metasurfaces at the frequency of 1.1 THz at gate voltages of 0 and 1.8 V respectively, (**m**) schematic of CD transmission, (**n**) measured transmission spectra for RCP and LCP waves at different gate voltages, (**o**) measured and simulated intensity modulation depth as a function of gate voltage (inset: measured CD with different gate voltages), (**p**) schematic of OA transmission, (**q**) measured ellipticity with different gate voltages, (**r**) azimuthal rotation angle θ at the frequency where η=0 as a function of gate voltage. Figure reproduced with permission from: (a–i) ref.[348], © 2016 John Wiley and Sons; (j–r) ref.[349], under a Creative Commons Attribution NonCommercial License 4.0 (CC BY-NC).

light and realize polarization encoding as well as polarization-division multiplexing (PDM)[348]. The proposed metasurface contained a gold film with rectangular aperture, which had strong anisotropy: largely different responses for the incident light polarized along two orthogonal principal axes of rectangular aperture. The calculated reflection spectra and normalized Stokes parameter S_3 in Fig. 22(b) and 22(c) showed a large reflection amplitude and widely tunable range of the polarization state. As illustrated in Fig. 22(d) and 22(f), the linearly polarized (LP) incident light could be converted into ideal LCP or RCP light when the gate voltage is 34 or 170 V respectively; When the gate voltage is 89 V, as shown in Fig. 22(e), the reflected light is LP with polarization direction nearly perpendicular to the incident LP light. Thus, the LP incident light can be transformed into LCP, RCP, and orthogonal LP light by the proposed metadevice through only switching the gate voltage applied on graphene. It can be seen from Fig. 22(g) that when the gate voltage swept from 20 to 205 V, the Stokes parameters varied continuously in large ranges and in particular S_3 covered the range from −1 to 1, indicating the continuous polarization evolution from LCP to RCP. The continuous path in the Poincaré sphere, as shown in Fig. 22(h), revealed that all polarization states on the path could be dynamically achieved by tuning gate voltage. By using the proposed metadevice, two independent binary-format signals could be directly encoded into a single light beam with superposition of LCP and RCP light beams in the time domain, describing the PDM technique as shown in Fig. 22(i). Similar to the circular orthogonal polarization basis, polarization encoding and PDM based on the linear orthogonal polarization basis were also demonstrated using the proposed metadevice when the incident light was elliptically polarized. In the THz regime, Kim et al. demonstrated the directly electrical tuning of the polarization state in gate-graphene integrated chiral metadevice, including gate-controlled circular dichroism (CD) and optical activity (OA)[349]. The metadevice consisted of a layer of graphene and bilayer of the chiral metasurface, as shown in Fig. 22(j), with a conjugated double Z-shape gold layer. The simulated electric field distributions in Fig. 22(k) and 22(l) revealed the different responses of the metadevice for LCP and RCP waves due to the different radiation losses, leading to electrically selective control of polarization state. Figure 22(m–o) provided the CD performances of the metadevice. The measured transmission spectra in Fig. 22(n) evidenced the CD transmission: the transmission of RCP THz wave exhibited obvious resonance feature and could be strongly modulated by gate voltage, while that of LCP wave was very insensitive to the applied voltage. For the RCP wave, the modulation depth was measured up to 99% at the resonance frequency of 1.1 THz, as shown in Fig. 22(o). The electrical modulation of CD, defined by the difference in transmission for RCP and LCP waves, was plotted in the inset of Fig. 22(o) and as a result, a very large CD value of ~45 dB was achieved. Additionally, the proposed metadevice could work as an active polarization rotator for LP THz wave, as illustrated in Fig. 22(p), which is usually called OA. It can be seen from the measured ellipticity in Fig. 22(q) that at the off-resonance frequency of ~1.42 THz, the ellipticity almost equaled zero, implying the nearly identical transmission of RCP and LCP waves. Consequently, the polarization rotation of the LP wave could be obtained at this off-resonance frequency. Figure 22(r) gave the measured relation between rotation angle and gate voltage, and showed the dynamically electrical tuning of rotation angle from 30° to 40°.

Digital coding metasurfaces based on locally-controlled graphene

Compared with homogeneous metasurfaces based on globally-controlled graphene, it is highly desired to independently control the unit cells of metasurfaces, which provides more degrees of freedom and possibilities for manipulating EM waves. In order to explore the distinct abilities for manipulating EM waves in programmable manners, in 2014, Cui et al. proposed a new concept of digital metamaterials, which has advanced metamaterials and metasurfaces more controllable, multi-functional, and intelligent[350–352]. In general, the core feature of digital metamaterials relies on the independently-controllable metaatom or array of several metaatoms. In 2018, Balci et al. demonstrated an electrically reconfigurable digital metadevice working in microwave frequencies with the assistance of locally-controlled graphene[79]. Firstly, the electrical control of both amplitude and phase of microwave was theoretically and experimentally investigated in graphene-integrated split-ring resonator (SRR) metasurfaces. Then, based on the digital metasurface concept, they proposed a digital metadevice with spatially varying dielectric constant to implement voltage-controlled adaptive transformation optics. As shown in Fig. 23(a–c), the local dielectric constant could

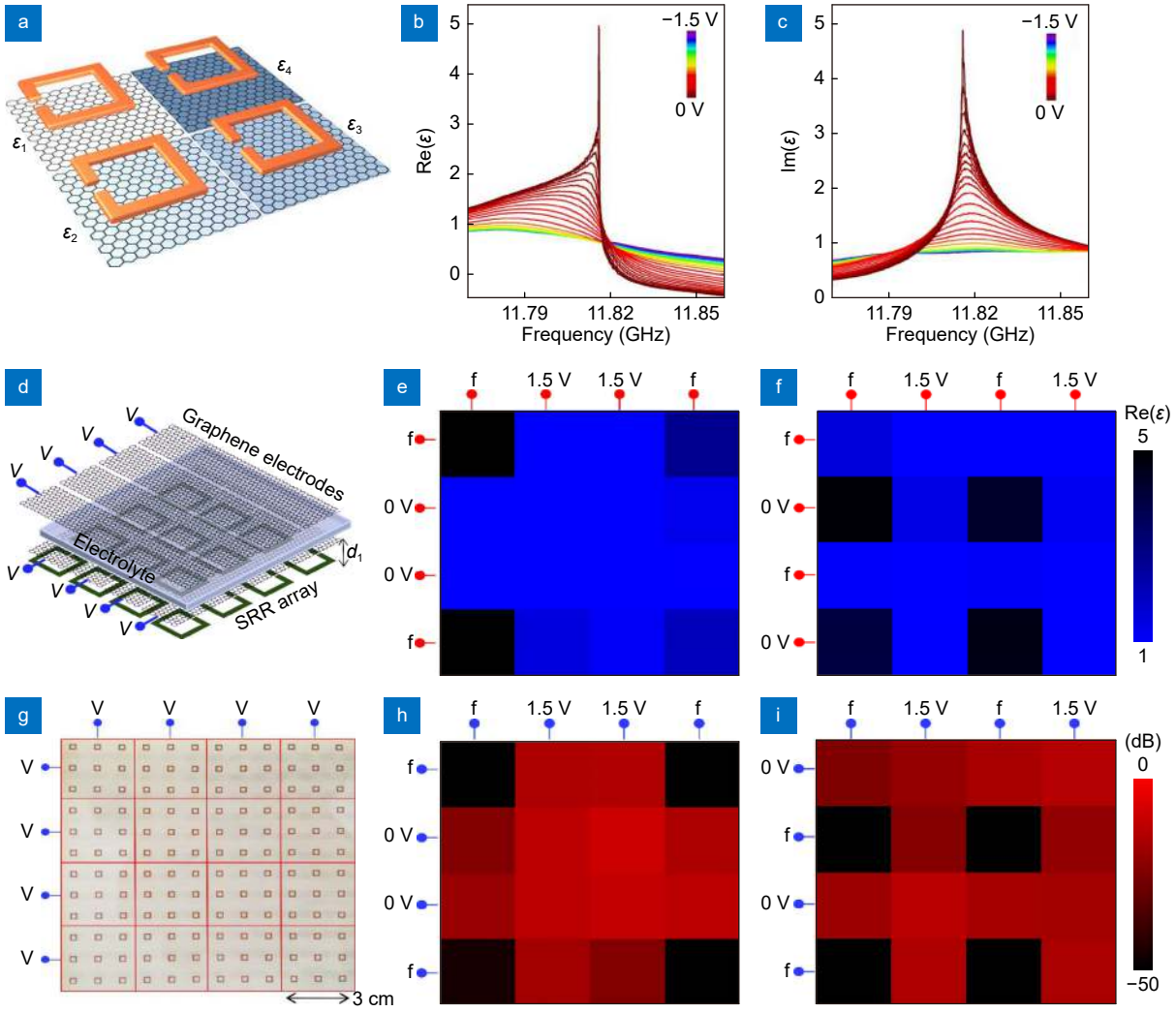

Fig. 23 | Electrically reconfigurable digital graphene-hybrid metadevices with spatially varying dielectric constant. (**a**) Schematic of a digital metasurface with individually addressable pixels, (**b**) and (**c**) calculated real and imaginary part of the effective dielectric constant in a single pixel as functions of bias voltages, (**d**) schematic of the pixelated metadevice, (**e**) and (**f**) spatial maps of the real part of the dielectric constant at different voltage configuration, (**g**) photograph of fabricated metadevice with 4×4 arrays of active pixel containing 3×3 SRRs, (**h**) and (**i**) measured transmission patterns corresponding to (e) and (f) respectively. Figure reproduced with permission from ref.[79], under a Creative Commons Attribution NonCommercial License 4.0 (CC BY-NC).

be reconfigured by controlling the gate voltage on individual metaatoms. The pixelated metadevice shown in Fig. 23(d) and 23(g) consisted of 4×4 arrays of active pixels and each pixel contained 3×3 SRRs (*i.e.* metaatom), where patterned graphene layers were used as top and bottom electrodes to locally control the pixels in a row or a column. By varying applied bias configuration to the electrodes, charge density on pixels could be controlled actively and hence dielectric constant pattern was configured, as shown in Fig. 23(e) and 23(f). As a result, various transmission patterns were obtained with various voltage configurations, as shown in Fig. 23(h) and 23(i).

More recently, a programmable graphene-metal hybrid metasurface for dynamic wavefront control of the microwave was experimentally reported by Chen et al., based on which dynamic functions including beam redirecting and Radar cross section (RCS) reduction was achieved with binary phase coding[353]. As shown in Fig. 24(a) and 24(b), the proposed phase coding metasurface consisted of four layers including metal patch, substrate, ground, and patterned graphene ribbon sandwich layer, where the sheet resistance of different graphene ribbons was independently tuned by DC voltages. Thanks to the uniform amplitude and opposite phase of the reflected wave, as shown in Fig. 24(b), the binary phase coding in unit cells described as "0" bit and "1" bit could be easily achieved by setting voltages at 0 and 4 V respectively. On

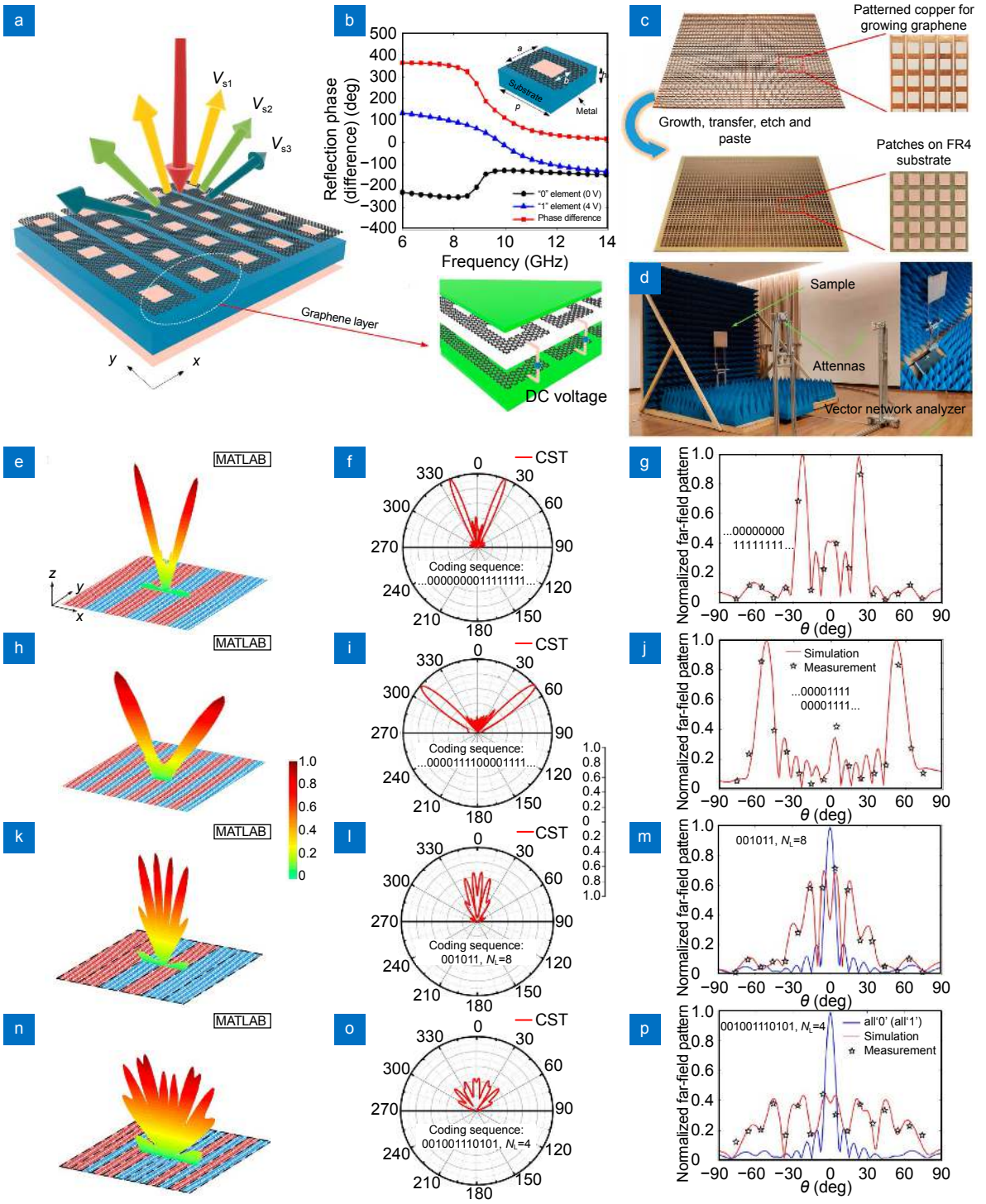

Fig. 24 | Programmable graphene-hybrid metasurfaces for dynamic wavefront control. (**a**) Conceptual illustration of the metasurface, (**b**) phase of the reflected waves from the coding graphene metasurface elements, (**c**) photograph of fabricated metasurfaces, (**d**) measurement system, (**e**-**g**) calculated, simulated, and measured far-field results for beam redirecting at the coding sequence of...0000000011111111..., (**h**-**j**) results for beam redirecting at the coding sequence of...0000111100001111..., (**k**-**m**) results for RCS reduction at the coding sequence of 001011 with 8 unit cells in a lattice, (**n**-**p**) results for RCS reduction at the coding sequence of 001001110101 with 4 unit cells in a lattice. Figure reproduced with permission from ref.[353], © 2020 ACS.

the basis of this property, applications of the designed graphene-based coding metasurfaces were focused on beam redirecting and RCS reduction. The fabricated metasurface consisted of 48×48 elements with the overall size of 226 mm×226 mm, as shown in Fig. 24(c). The far-field patterns from MATLAB calculation and CST

simulation agreed well with experimentally measured scattering field using the free-space wave method shown in Fig. 24(d). Specifically, the simplest arrangement of coding metasurface is the all "0" or all "1" scenario, which means unit cells in metasurface with identical phase distribution. Under this scenario, the far-field scattering beam would be reflected along the incident direction. For periodic coding sequences, as shown in Fig. 24(e–j), the normally incident beams could be scattered into two symmetrically radiating branches, and the reflection angle was strongly associated with the coding sequence, indicating programmable beam redirecting. For more complicated coding sequences such as random coding instead of periodic, more sophisticated wavefront control could be enabled, for example the RCS reduction, which was here accomplished by both absorbing the incident wave and redirecting the residual energy. Compared with beam redirecting in two branches using periodic coding, the complex random coding sequences led to more branches in the far-field radiating pattern, as shown in Fig. 24(k–p). It is worth noting that with the radiating branches increasing, the energy of incident beam was scattered into more directions, and thus the RCS of the proposed metasurface was reduced accordingly.

Actually, complete manipulation of EM waves requires the arbitrary control of both phase and amplitude. However, most of the digital coding metasurfaces solely depend on the phase shift while the amplitude response is usually fixed. To address this issue, Zhang et al. directly introduced the independent amplitude modulation into phase coding metasurface by designing a graphene-based digital coding metasurface for dynamical and continuous wavefront control of reflected wave in the microwave band[354]. This metasurface was mainly composed of metallic structures and a graphene sandwich structure with fishnet patterns, as shown in Fig. 25(a), by which continuous amplitude modulation could be implemented through controlling the sheet resistance of graphene while the phase response was kept unchanged. The binary phase coding of "0" and "1" was realized using two types of metaatoms with π phase difference. The phase coding sequences of the metasurface were schematically shown in Fig. 25(b), in which the "1" and "0" elements comprised 4×4 equal-sized metaatoms. Based on the standard print circuit board technique, a prototype of the patterned metal layer containing 32×32 metaatoms with "0" and "1" coding was fabricated, as shown in Fig. 25(c), and the patterned graphene layer was fabricated by standard laser cutting method shown in Fig. 25(d). Both the simulated and experimental results in Fig. 25(e–m) revealed that the far-field scattering pattern would be continuously tuned from directional mirror reflection to diffusive scattering when increasing the sheet resistance from 220 to 1500 Ω. Obviously, only a dominant pencil-like reflected beam was observed with low side lobes for 220 Ω. When resistance increased to 1500 Ω, the directional beam was destroyed with randomly distributed energy in various directions, implying the significant RCS reduction, which can be interpreted by interference of the scattering waves with random phase caused by amplitude modulation.

Conclusion and outlook

To summarize, we have provided a comprehensive review of the dynamic metasurfaces and metadevices enabled by graphene, including metasurfaces with building blocks of structured graphene and metasurfaces hybridly-integrated with graphene, with our focus on electrically-controlled dynamical manipulation of the EM waves covering the MIR, THz, and microwave regimes. Before discussing the state-of-the-art developments, the fundamentals of graphene as diverse as the basic material properties, plasmons in graphene, and in particular the theoretical and numerical models of GPs are described in details. Above all, the dynamic functionalities of the spectrum manipulation, wavefront shaping, polarization control, and frequency conversion in both near/far fields and global/local manners are elaborated using graphene-empowered metasurfaces and metadevices. As a comparative comment, it should be emphasized that the ultrabroadband and continuous tunability of graphene by external electrical stimuli empowers the metasurfaces and metadevices with the real-time, dynamical tunability over almost the entire spectrum of EM waves, which can never be accomplished currently by other solutions such as phase-change materials and transparent conducting oxides. Although chip-integrated MIR metadevices and microwave programmable metadevices using graphene have been already reported, it does not mean that graphene metasurfaces have been developed sufficiently. Here, we would like to underline that the investigation is just started in terms of the emerging concept in dynamic metasurfaces and widely potential applications in the future. Currently, this field is experiencing the explosive developments, where opportunities

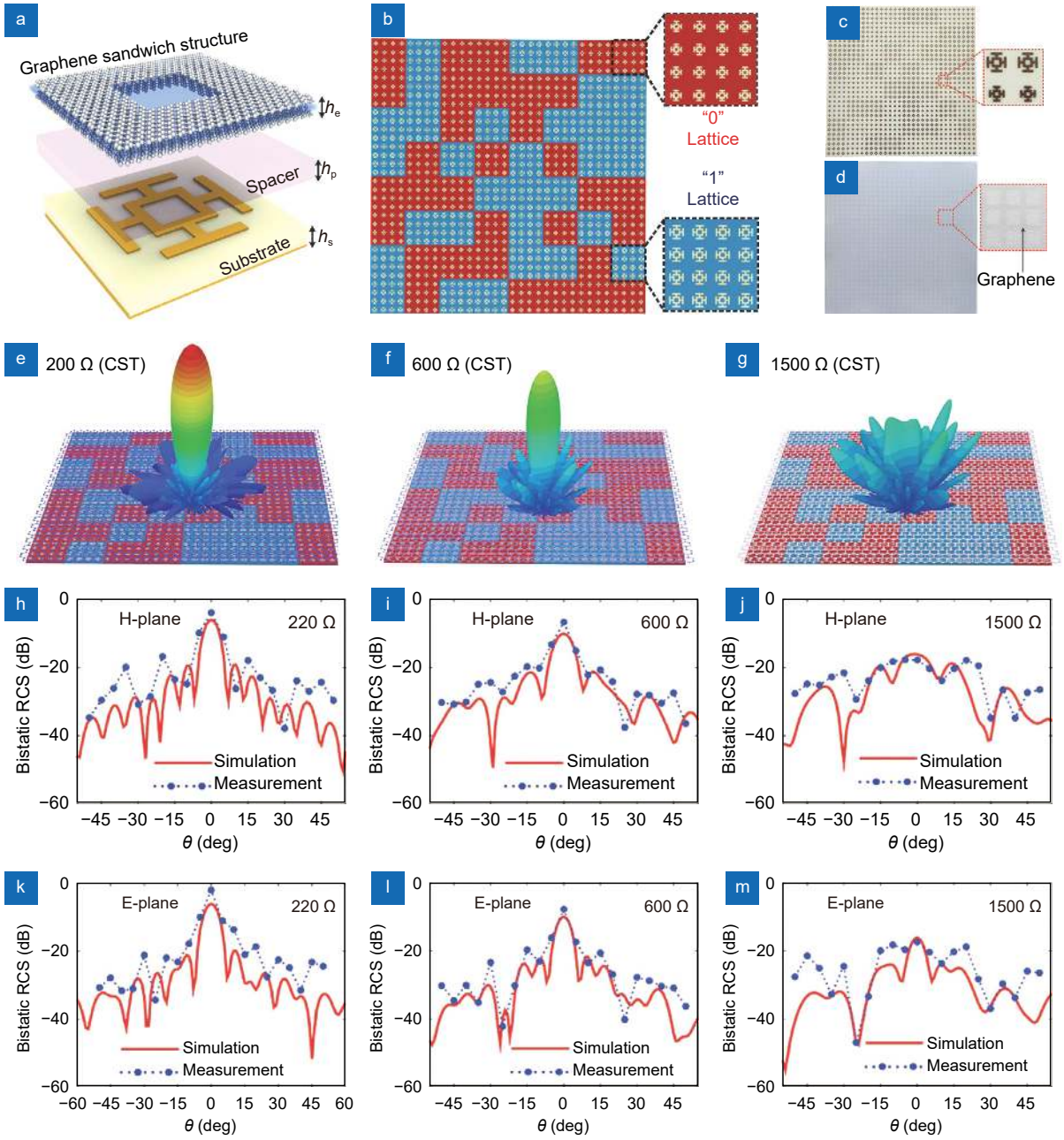

Fig. 25 | Dynamic scattering steering using graphene-integrated digital coding metasurfaces. (**a**) 3D schematic of the metaatom consisting of five layers: graphene layer, spacer, metal pattern, substrate, and ground layer, (**b**) optimal coding distributions of the proposed metasurface, (**c**) and (**d**) photograph of metal patterned layer and graphene patterned layer, (**e**-**g**) simulated 3D scattering patterns at different surface resistances of graphene, (**h**-**m**) measured bistatic RCS of the proposed coding metasurface in the H- and E-plane. Figure reproduced with permission from ref.[354], © 2020 John Wiley and Sons.

and challenges coexist.

For metasurfaces based structured graphene, their developments highly depend on the design method and nanofabrication techniques for graphene patterns in particular with more complicated geometry and larger footprint. For the design methods, as the demands of performance and functionality growing, the pattern design and optimization of metasurfaces and metadevices become computationally expensive and time-inefficient. To overcome such challenge, the artificial intelligence-based algorithms for smart inverse design show great potentials, which can search the parameter space in a more efficient way, leading to the on-demand design of novel metasurfaces and metadevices with tremendous complexity[355,356]. For the nanofabrication techniques, currently, the simple and periodic graphene patterns

such as ribbons, disks, and rings are widely fabricated by using standard electron-beam lithography (EBL) followed by plasma etching. To achieve polarization and/or phase manipulations, however, the anisotropic and aperiodic graphene patterns are indispensable, which requires high-quality nanofabrication technique because the defect and edge effects of graphene patterns strongly impact the polarization and phase responses of EM waves. For example, to efficiently exploit the PB phase for dynamic wavefront shaping, it is essential to arrange the anisotropic graphene patterns with varying rotation angles, which have not yet been experimentally validated due to the fabrication challenge for high-quality graphene patterns. Besides the EBL, recently-developed direct laser writing technique may provide a promising alternative to address this challenge by right of the advantages of mask-free and resist-free, which can avoid degenerating the quality of graphene patterns induced by the complex procedures in EBL and simultaneously enhance the fabrication efficiency for complex patterns[114,357,358]. Before the pattern fabrication, the challenges to achieve consistent, large-scale, transfer-free, and layer-number-controlled graphene films are worth mentioning, which to some extent determines the viability of the fabrication technology. To address these challenges, the graphene oxide routine has been recently demonstrated as a new solution by Jia et al., where the solution-phase preparation of the high-quality and large-scale graphene oxide layer is firstly performed, and then controllable conversion from graphene oxide layer into graphene layer is accomplished based on laser photoreduction[359]. Moreover, such laser patterning technique naturally results in equivalent fabrication of functional photonic devices for integrated photonics and flat optics[360]. To date, they have experimentally reported an ultrabroadband graphene oxide flat lens for wavefront shaping and an ultrathin graphene metamaterial for extremely broadband absorption of unpolarized light[260,361]. This low-cost and scalable method provides unprecedented control over the layer thickness, number, and pattern in particularly designing and fabricating multilayer graphene-based metamaterials, which exhibit great potentials in the future. In addition, the new metasurface concept, such as on-chip metasurfaces and time-variant metasurfaces[50,362–365], and functionalities as that of metallic and dielectric counterparts are highly expected to be transplanted into graphene-based metasurfaces and metadevices such as multidimensional EM wave manipulations.

For graphene-hybrid metasurfaces, the future in fact goes along with the development of conventional passive metasurfaces including concept and fabrication. A number of experimental works have proved that integrating graphene layer to the metallic or dielectric metasurfaces and metadevices can transform the passive metadevices to be more active and multifunctional, which are extremely desired for integrated photonic applications. Despite the rapidly growing demand, dynamic metasurfaces lag behind passive metasurfaces in terms of the functionalities. The dynamic versions of many intriguing functionalities have not been actualized experimentally using graphene-hybrid metasurfaces, including dynamic holography, encryption, orbital-angular momentum multiplexing and demultiplexing, etc. The challenges mainly exist in integrating high-quality graphene layer to metasurfaces and metadevices, and also fabricating the electrodes without influence on the quality of graphene. Generally, the dynamic tunability of a metasurface is actualized by putting a graphene layer in its proximity, which significantly influences the EM response of the metasurface. Such dynamic tuning is widely implemented by electrical method using metallic electrode or graphene electrode, which challenge the fabrication process and also limit the tuning speed as well as footprint of metadevices. To overcome the speed limitation of electric switches, all-optical control is a promising direction based on the optical nonlinearity of graphene enhanced by the extreme light confinement in metasurface, which can also greatly reduce the device footprint without electrodes[366]. The dynamic manipulations of amplitude, phase, and polarization have been reported in the NIR, MIR, and THz regimes by globally-controlled graphene-hybrid metasurfaces and in the microwave band by locally-controlled graphene-hybrid metasurfaces. However, due to the difficulty of locally controlling the individual metaatoms in metasurfaces at the shortwave frequencies, where the sizes of metaatoms and metasurfaces are smaller than that at the longwave frequencies, manipulating the EM waves in the NIR, MIR, and THz regimes by programmable manners based on the digital metasurface concept remains challenges.

At last, dynamic metasurfaces and metadevices enabled by other graphene-like 2D materials, such as BP, TIs, and TMDCs, are also an attractive direction[367–373]. Besides electrical tunability, 2D materials beyond graphene can empower more unique advantages to

metasurfaces and metadevices, such as nonlinearity together with optical controllability, which will undoubtedly expand the degrees of freedom in EM wave manipulation and improve the modulation speed by optical-controllable metasurfaces. Several research groups have recently focused on the 2D materials-based metasurfaces to explore the new value of 2D materials and metasurfaces. For example, Novotny et al. demonstrated controllable steering of the second harmonic (SH) emission by coupling a monolayer MoS_2 onto an optical phased array consisting of gold antennas[374]; By integrated WS_2 with Au plasmonic nanosieve metasurfaces, Lu et al. reported the SH metalens, OAM generation, beam steering, polarization control, and holograms[375–377]; Zentgraf et al. proposed a WS_2-integrated plasmonic metasurface based on PB phase to modulate the polarization and phase of SH signal[378]. Those pioneering works offer new opportunities for dynamically generating and manipulating the EM waves by nonlinear means. With the all potential future directions and gradually improved nanofabrication technique, we believe that the dynamic metasurfaces and metadevices using graphene and further graphene-like 2D materials will certainly revolutionize the EM wave manipulations and finally commercialized applications in the future.

References

1. Yu NF, Genevet P, Kats MA, Aieta F, Tetienne JP et al. Light propagation with phase discontinuities: generalized laws of reflection and refraction. *Science* **334**, 333–337 (2011).
2. Li GX, Zhang S, Zentgraf T. Nonlinear photonic metasurfaces. *Nat Rev Mater* **2**, 17010 (2017).
3. Tseng ML, Hsiao HH, Chu CH, Chen MK, Sun G et al. Metalenses: advances and applications. *Adv Opt Mater* **6**, 1800554 (2018).
4. Chen SQ, Li ZC, Liu WW, Cheng H, Tian JG. From single-dimensional to multidimensional manipulation of optical waves with metasurfaces. *Adv Mater* **31**, 1802458 (2019).
5. Wang HT, Hao CL, Lin H, Wang YT, Lan T et al. Generation of super-resolved optical needle and multifocal array using graphene oxide metalenses. *Opto-Electron Adv* **4**, 200031 (2021).
6. Jiang Q, Jin GF, Cao LC. When metasurface meets hologram: principle and advances. *Adv Opt Photonics* **11**, 518–576 (2019).
7. Zhang XG, Jiang WX, Jiang HL, Wang Q, Tian HW et al. An optically driven digital metasurface for programming electromagnetic functions. *Nat Electron* **3**, 165–171 (2020).
8. Zhang YB, Liu H, Cheng H, Tian JG, Chen SQ. Multidimensional manipulation of wave fields based on artificial microstructures. *Opto-Electron Adv* **3**, 200002 (2020).
9. Arbabi A, Horie Y, Bagheri M, Faraon A. Dielectric metasurfaces for complete control of phase and polarization with subwavelength spatial resolution and high transmission. *Nat Nanotechnol* **10**, 937–943 (2015).
10. Kamali SM, Arbabi E, Arbabi A, Horie Y, Faraji-Dana M et al. Angle-multiplexed metasurfaces: encoding independent wavefronts in a single metasurface under different illumination angles. *Phys Rev X* **7**, 041056 (2017).
11. Liu ZC, Li ZC, Liu Z, Cheng H, Liu WW et al. Single-layer plasmonic metasurface half-wave plates with wavelength-independent polarization conversion angle. *ACS Photonics* **4**, 2061–2069 (2017).
12. Jang M, Horie Y, Shibukawa A, Brake J, Liu Y et al. Wavefront shaping with disorder-engineered metasurfaces. *Nat Photonics* **12**, 84–90 (2018).
13. Overvig AC, Shrestha S, Malek SC, Lu M, Stein A et al. Dielectric metasurfaces for complete and independent control of the optical amplitude and phase. *Light Sci Appl* **8**, 92 (2019).
14. Guo JY, Wang T, Quan BG, Zhao H, Gu CZ et al. Polarization multiplexing for double images display. *Opto-Electron Adv* **2**, 180029 (2019).
15. Khorasaninejad M, Chen WT, Devlin RC, Oh J, Zhu AY et al. Metalenses at visible wavelengths: diffraction-limited focusing and subwavelength resolution imaging. *Science* **352**, 1190–1194 (2016).
16. Wang SM, Wu PC, Su VC, Lai YC, Hung Chu C et al. Broadband achromatic optical metasurface devices. *Nat Commun* **8**, 187 (2017).
17. Chen WT, Zhu AY, Sanjeev V, Khorasaninejad M, Shi ZJ et al. A broadband achromatic metalens for focusing and imaging in the visible. *Nat Nanotechnol* **13**, 220–226 (2018).
18. Shrestha S, Overvig AC, Lu M, Stein A, Yu NF. Broadband achromatic dielectric metalenses. *Light Sci Appl* **7**, 85 (2018).
19. Wang SM, Wu PC, Su VC, Lai YC, Chen MK et al. A broadband achromatic metalens in the visible. *Nat Nanotechnol* **13**, 227–232 (2018).
20. Fan ZB, Qiu HY, Zhang HL, Pang XN, Zhou LD et al. A broadband achromatic metalens array for integral imaging in the visible. *Light Sci Appl* **8**, 67 (2019).
21. Park JS, Zhang SY, She A, Chen WT, Lin P et al. All-glass, large metalens at visible wavelength using deep-ultraviolet projection lithography. *Nano Lett* **19**, 8673–8682 (2019).
22. Wen DD, Yue FY, Li GX, Zheng GX, Chan KL et al. Helicity multiplexed broadband metasurface holograms. *Nat Commun* **6**, 8241 (2015).
23. Li X, Chen LW, Li Y, Zhang XH, Pu MB et al. Multicolor 3D meta-holography by broadband plasmonic modulation. *Sci Adv* **2**, e1601102 (2016).
24. Ren HR, Briere G, Fang XY, Ni PN, Sawant R et al. Metasurface orbital angular momentum holography. *Nat Commun* **10**, 2986 (2019).
25. Deng ZL, Jin MK, Ye X, Wang S, Shi T et al. Full-color complex-amplitude vectorial holograms based on multi-freedom metasurfaces. *Adv Funct Mater* **30**, 1910610 (2020).
26. Zhang F, Pu MB, Gao P, Jin JJ, Li X et al. Simultaneous full-color printing and holography enabled by centimeter-scale plasmonic metasurfaces. *Adv Sci* **7**, 1903156 (2020).
27. Li Z, Liu WW, Li ZC, Tang CC, Cheng H et al. Tripling the capacity of optical vortices by nonlinear metasurface. *Laser Photon Rev* **12**, 1800164 (2018).
28. Yan C, Li X, Pu MB, Ma XL, Zhang F et al. Generation of polarization-sensitive modulated optical vortices with all-dielectric metasurfaces. *ACS Photonics* **6**, 628–633 (2019).

29. Zang XF, Zhu YM, Mao CX, Xu WW, Ding HZ et al. Manipulating terahertz plasmonic vortex based on geometric and dynamic phase. *Adv Opt Mater* **7**, 1801328 (2019).
30. Li Y, Li X, Chen LW, Pu MB, Jin JJ et al. Orbital angular momentum multiplexing and demultiplexing by a single metasurface. *Adv Opt Mater* **5**, 1600502 (2017).
31. Li SQ, Li XY, Zhang L, Wang GX, Zhang LX et al. Efficient optical angular momentum manipulation for compact multiplexing and demultiplexing using a dielectric metasurface. *Adv Opt Mater* **8**, 1901666 (2020).
32. Qu SW, Wu WW, Chen BJ et al. Controlling Dispersion Characteristics of Terahertz Metasurface. *Sci Rep* **5**, 9367 (2015).
33. Dou KH, Xie X, Pu MB, Li X, Ma XL et al. Off-axis multi-wavelength dispersion controlling metalens for multi-color imaging. *Opto-Electron Adv* **3**, 190005 (2020).
34. Zhang X, Li Q, Liu F et al. Controlling angular dispersions in optical metasurfaces. *Light Sci Appl* **9**, 76 (2020).
35. Wang YL, Fan QB, Xu T. Design of high efficiency achromatic metalens with large operation bandwidth using bilayer architecture. *Opto-Electron Adv* **4**, 200008 (2021).
36. Scheuer J. Optical metasurfaces are coming of age: short- and long-term opportunities for commercial applications. *ACS Photonics* **7**, 1323–1354 (2020).
37. Luo J, Zeng B, Wang CT, Gao P, Liu KP et al. Fabrication of anisotropically arrayed nano-slots metasurfaces using reflective plasmonic lithography. *Nanoscale* **7**, 18805–18812 (2015).
38. Sun S, Zhou ZX, Zhang C, Gao YS, Duan ZH et al. All-dielectric full-color printing with TiO_2 metasurfaces. *ACS Nano* **11**, 4445–4452 (2017).
39. Su VC, Chu CH, Sun G, Tsai DP. Advances in optical metasurfaces: fabrication and applications [Invited]. *Opt Express* **26**, 13148–13182 (2018).
40. Xu ZJ, Dong Y, Tseng CK, Hu T, Tong JC et al. CMOS-compatible all-Si metasurface polarizing bandpass filters on 12-inch wafers. *Opt Express* **27**, 26060–26069 (2019).
41. Li HP, Wang GM, Hu GW, Cai T, Qiu CW et al. 3D-printed curved metasurface with multifunctional wavefronts. *Adv Opt Mater* **8**, 2000129 (2020).
42. Xomalis A, Demirtzioglou I, Plum E, Jung Y, Nalla V et al. Fibre-optic metadevice for all-optical signal modulation based on coherent absorption. *Nat Commun* **9**, 182 (2018).
43. Xie YY, Ni PN, Wang QH, Kan Q, Briere G et al. Metasurface-integrated vertical cavity surface-emitting lasers for programmable directional lasing emissions. *Nat Nanotechnol* **15**, 125–130 (2020).
44. Sroor H, Huang YW, Sephton B, Naidoo D, Vallés A et al. High-purity orbital angular momentum states from a visible metasurface laser. *Nat Photonics* **14**, 498–503 (2020).
45. Wang JY, Coillet A, Demichel O, Wang ZQ, Rego D et al. Saturable plasmonic metasurfaces for laser mode locking. *Light Sci Appl* **9**, 50 (2020).
46. Li SQ, Li XY, Wang GX, Liu S, Zhang LX et al. Multidimensional manipulation of photonic spin hall effect with a single-layer dielectric metasurface. *Adv Opt Mater* **7**, 1801365 (2019).
47. Ma XL, Pu MB, Li X, Guo YH, Luo XG. All-metallic wide-angle metasurfaces for multifunctional polarization manipulation. *Opto-Electron Adv* **2**, 180023 (2019).
48. Ma DN, Li Z, Cheng H, Chen SQ. Multi-dimensional manipulation of optical field with metasurfaces and its optimization based on machine learning. *Chin Sci Bull* **65**, 1824–1844 (2020).
49. Yu NF, Capasso F. Flat optics with designer metasurfaces. *Nat Mater* **13**, 139–150 (2014).
50. Meng Y, Liu ZT, Xie ZW, Wang RD, Qi TC et al. Versatile on-chip light coupling and (de)multiplexing from arbitrary polarizations to controlled waveguide modes using an integrated dielectric metasurface. *Photonics Res* **8**, 564–576 (2020).
51. Lapine M, Shadrivov IV, Kivshar YS. Colloquium: nonlinear metamaterials. *Rev Mod Phys* **86**, 1093–1123 (2014).
52. Sain B, Meier C, Zentgraf T. Nonlinear optics in all-dielectric nanoantennas and metasurfaces: a review. *Adv Photonics* **1**, 024002 (2019).
53. Fang XY, Ren HR, Gu M. Orbital angular momentum holography for high-security encryption. *Nat Photonics* **14**, 102–108 (2020).
54. Zhao J, Yang X, Dai JY, Cheng Q, Li X et al. Programmable time-domain digital-coding metasurface for non-linear harmonic manipulation and new wireless communication systems. *Natl Sci Rev* **6**, 231–238 (2019).
55. Li LL, Ruan HX, Liu C, Li Y, Shuang Y et al. Machine-learning reprogrammable metasurface imager. *Nat Commun* **10**, 1082 (2019).
56. Wu ZC, Zhou M, Khoram E, Liu BY, Yu ZF. Neuromorphic metasurface. *Photonics Res* **8**, 46–50 (2020).
57. Wang K, Titchener JG, Kruk SS, Xu L, Chung HP et al. Quantum metasurface for multiphoton interference and state reconstruction. *Science* **361**, 1104–1107 (2018).
58. Li L, Liu ZX, Ren XF, Wang SM, Su VC et al. Metalens-array-based high-dimensional and multiphoton quantum source. *Science* **368**, 1487–1490 (2020).
59. Lu CC, Hu XY, Shi KB, Hu Q, Zhu R et al. An actively ultrafast tunable giant slow-light effect in ultrathin nonlinear metasurfaces. *Light Sci Appl* **4**, e302 (2015).
60. Yin XH, Steinle T, Huang LL, Taubner T, Wuttig M et al. Beam switching and bifocal zoom lensing using active plasmonic metasurfaces. *Light Sci Appl* **6**, e17016 (2017).
61. Zhang M, Ma XL, Pu MB, Liu KP, Guo YH et al. Large-area and low-cost nanoslit-based flexible metasurfaces for multispectral electromagnetic wave manipulation. *Adv Opt Mater* **7**, 1900657 (2019).
62. Shaltout AM, Shalaev VM, Brongersma ML. Spatiotemporal light control with active metasurfaces. *Science* **364**, eaat3100 (2019).
63. Zhang XG, Yu Q, Jiang WX, Sun YL, Bai L et al. Polarization-controlled dual-programmable metasurfaces. *Adv Sci* **7**, 1903382 (2020).
64. Papaioannou M, Plum E, Rogers ETF, Zheludev NI. All-optical dynamic focusing of light via coherent absorption in a plasmonic metasurface. *Light Sci Appl* **7**, 17157 (2018).
65. Liu XB, Wang Q, Zhang XQ, Li H, Xu Q et al. Thermally dependent dynamic meta-holography using a vanadium dioxide integrated metasurface. *Adv Opt Mater* **7**, 1900175 (2019).
66. Cala Lesinà A, Goodwill D, Bernier E, Ramunno L, Berini P. Tunable plasmonic metasurfaces for optical phased arrays. *IEEE J Sel Top Quantum Electron* **27**, 4700116 (2021).
67. Park J, Kang JH, Kim SJ, Liu XG, Brongersma ML. Dynamic Reflection Phase and Polarization Control in Metasurfaces. *Nano Lett* **17**, 407–413 (2017).
68. Shirmanesh GK, Sokhoyan R, Pala RA, Atwater HA. Dual-gated active metasurface at 1550 nm with wide (>300°) phase tunability. *Nano Lett* **18**, 2957–2963 (2018).

69. Forouzmand A, Salary MM, Inampudi S, Mosallaei H. A tunable multigate indium-tin-oxide-assisted all-dielectric metasurface. *Adv Opt Mater* **6**, 1701275 (2018).
70. Rensberg J, Zhang SY, Zhou Y, McLeod AS, Schwarz C et al. Active optical metasurfaces based on defect-engineered phase-transition materials. *Nano Lett* **16**, 1050–1055 (2016).
71. Wang Q, Rogers ETF, Gholipour B, Wang CM, Yuan GH et al. Optically reconfigurable metasurfaces and photonic devices based on phase change materials. *Nat Photonics* **10**, 60–65 (2016).
72. Dong WL, Qiu YM, Zhou XL, Banas A, Banas K et al. Tunable mid-infrared phase-change metasurface. *Adv Opt Mater* **6**, 1701346 (2018).
73. Shen ZX, Zhou SH, Li XN, Ge SJ, Chen P et al. Liquid crystal integrated metalens with tunable chromatic aberration. *Adv Photonics* **2**, 036002 (2020).
74. Lee SH, Choi M, Kim TT, Lee S, Liu M et al. Switching terahertz waves with gate-controlled active graphene metamaterials. *Nat Mater* **11**, 936–941 (2012).
75. Yao Y, Shankar R, Kats MA, Song Y, Kong J et al. Electrically tunable metasurface perfect absorbers for ultrathin mid-infrared optical modulators. *Nano Lett* **14**, 6526–6532 (2014).
76. Li Q, Tian Z, Zhang XQ, Xu NN, Singh R et al. Dual control of active graphene –silicon hybrid metamaterial devices. *Carbon* **90**, 146–153 (2015).
77. Cheng H, Chen SQ, Yu P, Liu WW, Li ZC et al. Dynamically tunable broadband infrared anomalous refraction based on graphene metasurfaces. *Adv Opt Mater* **3**, 1744–1749 (2015).
78. Kindness SJ, Almond NW, Wei BB, Wallis R, Michailow W et al. Active control of electromagnetically induced transparency in a terahertz metamaterial array with graphene for continuous resonance frequency tuning. *Adv Opt Mater* **6**, 1800570 (2018).
79. Balci O, Kakenov N, Karademir E, Balci S, Cakmakyapan S et al. Electrically switchable metadevices via graphene. *Sci Adv* **4**, eaao1749 (2018).
80. Zhao J, Cheng Q, Chen J, Qi MQ, Jiang WX et al. A tunable metamaterial absorber using varactor diodes. *New J Phys* **15**, 043049 (2013).
81. Zhang L, Chen XQ, Liu S, Zhang Q, Zhao J et al. Space-time-coding digital metasurfaces. *Nat Commun* **9**, 4334 (2018).
82. Wu RY, Zhang L, Bao L, Wu LW, Ma Q et al. Digital metasurface with phase code and reflection-transmission amplitude code for flexible full-space electromagnetic manipulations. *Adv Opt Mater* **7**, 1801429 (2019).
83. Li Y, Lin J, Guo HJ, Sun WJ, Xiao SY et al. A tunable metasurface with switchable functionalities: from perfect transparency to perfect absorption. *Adv Opt Mater* **8**, 1901548 (2020).
84. Song SC, Ma XL, Pu MB, Li X, Liu KP et al. Actively tunable structural color rendering with tensile substrate. *Adv Opt Mater* **5**, 1600829 (2017).
85. Kamali SM, Arbabi E, Arbabi A, Horie Y, Faraon A. Highly tunable elastic dielectric metasurface lenses. *Laser Photon Rev* **10**, 1002–1008 (2016).
86. Malek SC, Ee HS, Agarwal R. Strain multiplexed metasurface holograms on a stretchable substrate. *Nano Lett* **17**, 3641–3645 (2017).
87. Roy T, Zhang SY, Jung IW, Troccoli M, Capasso F et al. Dynamic metasurface lens based on MEMS technology. *APL Photonics* **3**, 021302 (2018).
88. Zhao XG, Schalch J, Zhang JD, Seren HR, Duan GW et al. Electromechanically tunable metasurface transmission waveplate at terahertz frequencies. *Optica* **5**, 303–310 (2018).
89. Arbabi E, Arbabi A, Kamali SM, Horie Y, Faraji-Dana M et al. MEMS-tunable dielectric metasurface lens. *Nat Commun* **9**, 812 (2018).
90. Diebold AV, Imani MF, Sleasman T, Smith DR. Phaseless coherent and incoherent microwave ghost imaging with dynamic metasurface apertures. *Optica* **5**, 1529–1541 (2018).
91. Zhang C, Xiao SM, Wang YH, Gao YS, Fan YB et al. Lead halide perovskite-based dynamic metasurfaces. *Laser Photon Rev* **13**, 1900079 (2019).
92. Wu PC, Pala RA, Kafaie Shirmanesh G, Cheng WH, Sokhoyan R et al. Dynamic beam steering with all-dielectric electro-optic III-V multiple-quantum-well metasurfaces. *Nat Commun* **10**, 3654 (2019).
93. Nemati A, Wang Q, Hong MN, Teng JH. Tunable and reconfigurable metasurfaces and metadevices. *Opto-Electron Adv* **1**, 180009 (2018).
94. Li SQ, Xu XW, Veetil RM, Valuckas V, Paniagua-Dominguez R et al. Phase-only transmissive spatial light modulator based on tunable dielectric metasurface. *Science* **364**, 1087–1090 (2019).
95. Ren MX, Cai W, Xu JJ. Tailorable dynamics in nonlinear optical metasurfaces. *Adv Mater* **32**, 1806317 (2020).
96. Sun YL, Zhang XG, Yu Q, Jiang WX, Cui TJ. Infrared-controlled programmable metasurface. *Sci Bull* **65**, 883–888 (2020).
97. Ding F, Yang YQ, Bozhevolnyi SI. Dynamic metasurfaces using phase-change chalcogenides. *Adv Opt Mater* **7**, 1801709 (2019).
98. Cui T, Bai BF, Sun HB. Tunable metasurfaces based on active materials. *Adv Funct Mater* **29**, 1806692 (2019).
99. Kang L, Jenkins RP, Werner DH. Recent progress in active optical metasurfaces. *Adv Opt Mater* **7**, 1801813 (2019).
100. He Q, Sun SL, Zhou L. Tunable/reconfigurable metasurfaces: physics and applications. *Research* **2019**, 1849272 (2019).
101. Hail CU, Michel AKU, Poulikakos D, Eghlidi H. Optical metasurfaces: evolving from passive to adaptive. *Adv Opt Mater* **7**, 1801786 (2019).
102. Bonaccorso F, Sun Z, Hasan T, Ferrari AC. Graphene photonics and optoelectronics. *Nat Photonics* **4**, 611–622 (2010).
103. Xu MS, Liang T, Shi MM, Chen HZ. Graphene-like two-dimensional materials. *Chem Rev* **113**, 3766–3798 (2013).
104. Sun ZP, Martinez A, Wang F. Optical modulators with 2D layered materials. *Nat Photonics* **10**, 227–238 (2016).
105. Fan YC, Shen NH, Zhang FL, Zhao Q, Wu HJ et al. Graphene plasmonics: a platform for 2D optics. *Adv Opt Mater* **7**, 1800537 (2019).
106. Goossens S, Navickaite G, Monasterio C, Gupta S, Piqueras JJ et al. Broadband image sensor array based on graphene –CMOS integration. *Nat Photonics* **11**, 366–371 (2017).
107. de Abajo FJG. Graphene plasmonics: challenges and opportunities. *ACS Photonics* **1**, 135–152 (2014).
108. Xia FN, Wang H, Xiao D, Dubey M, Ramasubramaniam A. Two-dimensional material nanophotonics. *Nat Photonics* **8**, 899–907 (2014).
109. Anichini C, Czepa W, Pakulski D, Aliprandi A, Ciesielski A et al. Chemical sensing with 2D materials. *Chem Soc Rev* **47**, 4860–4908 (2018).
110. Autere A, Jussila H, Dai YY, Wang YD, Lipsanen H et al. Nonlinear optics with 2D layered materials. *Adv Mater* **30**, 1705963

(2018).
111. Qi X, Zhang YP, Ou QD, Ha ST, Qiu CW et al. Photonics and optoelectronics of 2D metal-halide perovskites. *Small* **14**, 1800682 (2018).
112. Klein M, Badada BH, Binder R, Alfrey A, McKie M et al. 2D semiconductor nonlinear plasmonic modulators. *Nat Commun* **10**, 3264 (2019).
113. Neumaier D, Pindl S, Lemme MC. Integrating graphene into semiconductor fabrication lines. *Nat Mater* **18**, 525–529 (2019).
114. Fu XY, Chen ZD, Han DD, Zhang YL, Xia H et al. Laser fabrication of graphene-based supercapacitors. *Photonics Res* **8**, 577–588 (2020).
115. Cao Y, Rodan-Legrain D, Rubies-Bigorda O, Park JM, Watanabe K et al. Tunable correlated states and spin-polarized phases in twisted bilayer-bilayer graphene. *Nature* **583**, 215–220 (2020).
116. Wang F, Zhang YB, Tian CS, Girit C, Zettl A et al. Gate-variable optical transitions in graphene. *Science* **320**, 206–209 (2008).
117. Grigorenko AN, Polini M, Novoselov KS. Graphene plasmonics. *Nat Photonics* **6**, 749–758 (2012).
118. Bao QL, Loh KP. Graphene photonics, plasmonics, and broadband optoelectronic devices. *ACS Nano* **6**, 3677–3694 (2012).
119. Amin M, Farhat M, Bağcı H. A dynamically reconfigurable Fano metamaterial through graphene tuning for switching and sensing applications. *Sci Rep* **3**, 2105 (2013).
120. Chen PY, Soric J, Padooru YR, Bernety HM, Yakovlev AB et al. Nanostructured graphene metasurface for tunable terahertz cloaking. *New J Phys* **15**, 123029 (2013).
121. Liu ZZ, Li ZY, Aydin K. Time-varying metasurfaces based on graphene microribbon arrays. *ACS Photonics* **3**, 2035–2039 (2016).
122. Wang C, Liu WW, Li ZC, Cheng H, Li Z et al. Dynamically tunable deep subwavelength high-order anomalous reflection using graphene metasurfaces. *Adv Opt Mater* **6**, 1701047 (2018).
123. Su ZX, Cheng F, Li L, Liu YM. Complete control of smith-purcell radiation by graphene metasurfaces. *ACS Photonics* **6**, 1947–1954 (2019).
124. Zhu H, Chen SQ, Wen J, Wang J, Chen L. Graphene-based metasurfaces for switching polarization states of anomalous reflection and focusing. *Opt Lett* **44**, 5764–5767 (2019).
125. Lin KT, Lin H, Yang TS, Jia BH. Structured graphene metamaterial selective absorbers for high efficiency and omnidirectional solar thermal energy conversion. *Nat Commun* **11**, 1389 (2020).
126. Han SJ, Kim S, Kim S, Low T, Brar VW et al. Complete complex amplitude modulation with electronically tunable graphene plasmonic metamolecules. *ACS Nano* **14**, 1166–1175 (2020).
127. You JW, Lan ZH, Panoiu NC. Four-wave mixing of topological edge plasmons in graphene metasurfaces. *Sci Adv* **6**, eaaz3910 (2020).
128. Novoselov KS, Geim AK, Morozov SV, Jiang D, Zhang Y et al. Electric field effect in atomically thin carbon films. *Science* **306**, 666–669 (2004).
129. Novoselov KS, Geim AK, Morozov SV, Jiang D, Katsnelson MI et al. Two-dimensional gas of massless Dirac fermions in graphene. *Nature* **438**, 197–200 (2005).
130. Geim AK, Novoselov KS. The rise of graphene. *Nat Mater* **6**, 183–191 (2007).
131. Novoselov KS, Fal′ko VI, Colombo L, Gellert PR, Schwab MG et al. A roadmap for graphene. *Nature* **490**, 192–200 (2012).
132. Lu H, Gong YK, Mao D, Gan XT, Zhao JL. Strong plasmonic confinement and optical force in phosphorene pairs. *Opt Express* **25**, 5255–5263 (2017).
133. Zhou Y, Zhang MX, Guo ZN, Miao LL, Han ST et al. Recent advances in black phosphorus-based photonics, electronics, sensors and energy devices. *Mater Horiz* **4**, 997–1019 (2017).
134. Luo MM, Fan TJ, Zhou Y, Zhang H, Mei L. 2D black phosphorus –based biomedical applications. *Adv Funct Mater* **29**, 1808306 (2019).
135. Xu XD, Yao W, Xiao D, Heinz TF. Spin and pseudospins in layered transition metal dichalcogenides. *Nat Phys* **10**, 343–350 (2014).
136. Zhu WJ, Low T, Lee YH, Wang H, Farmer DB et al. Electronic transport and device prospects of monolayer molybdenum disulphide grown by chemical vapour deposition. *Nat Commun* **5**, 3087 (2014).
137. Aslan OB, Chenet DA, van der Zande AM, Hone JC, Heinz TF. Linearly polarized excitons in single- and few-layer ReS_2 crystals. *ACS Photonics* **3**, 96–101 (2016).
138. Wang XT, Cui Y, Li T, Lei M, Li JB et al. Recent advances in the functional 2D photonic and optoelectronic devices. *Adv Opt Mater* **7**, 1801274 (2019).
139. Zhang ZP, Zhou F, Yang PF, Jiang B, Hu JY et al. Direct growth of multi-layer graphene on quartz glass for high-performance broadband neutral density filter applications. *Adv Opt Mater* **8**, 2000166 (2020).
140. Li JZ, Chen MG, Zhang CH, Dong HC, Lin WY et al. Fractal-theory-based control of the shape and quality of CVD-grown 2D materials. *Adv Mater* **31**, 1902431 (2019).
141. Novoselov KS, Jiang D, Schedin F, Booth TJ, Khotkevich VV et al. Two-dimensional atomic crystals. *Proc Natl Acad Sci USA* **102**, 10451–10453 (2005).
142. Chen JH, Jang C, Xiao SD, Ishigami M, Fuhrer MS. Intrinsic and extrinsic performance limits of graphene devices on SiO_2. *Nat Nanotechnol* **3**, 206–209 (2008).
143. Wang L, Meric I, Huang PY, Gao Q, Gao Y et al. One-dimensional electrical contact to a two-dimensional material. *Science* **342**, 614–617 (2013).
144. Du X, Skachko I, Barker A, Andrei EY. Approaching ballistic transport in suspended graphene. *Nat Nanotechnol* **3**, 491–495 (2008).
145. Liu M, Yin XB, Ulin-Avila E, Geng BS, Zentgraf T et al. A graphene-based broadband optical modulator. *Nature* **474**, 64–67 (2011).
146. Phare CT, Lee YHD, Cardenas J, Lipson M. Graphene electro-optic modulator with 30 GHz bandwidth. *Nat Photonics* **9**, 511–514 (2015).
147. Ye T, Wang B, Wang C, Li ZY, Zhang ZW et al. Approaching the intrinsic lifetime and modulating a graphene plasmonic resonance at a few hundred GHz. *Adv Opt Mater* **7**, 1900315 (2019).
148. Ding YH, Cheng Z, Zhu XL, Yvind K, Dong JJ et al. Ultra-compact integrated graphene plasmonic photodetector with bandwidth above 110 GHz. *Nanophotonics* **9**, 317–325 (2020).
149. Gan XT, Shiue RJ, Gao YD, Meric I, Heinz TF et al. Chip-integrated ultrafast graphene photodetector with high responsivity. *Nat Photonics* **7**, 883–887 (2013).
150. Guo JS, Li J, Liu CY, Yin YL, Wang WH et al. High-performance silicon-graphene hybrid plasmonic waveguide photodetectors beyond 1.55 μm. *Light Sci Appl* **9**, 29 (2020).

151. Nair RR, Blake P, Grigorenko AN, Novoselov KS, Booth TJ et al. Fine structure constant defines visual transparency of graphene. *Science* **320**, 1308 (2008).
152. Nikitin AY, Guinea F, Garcia-Vidal FJ, Martin-Moreno L. Surface plasmon enhanced absorption and suppressed transmission in periodic arrays of graphene ribbons. *Phys Rev B* **85**, 081405 (2012).
153. Fan YC, Wei ZY, Zhang ZR, Li HQ. Enhancing infrared extinction and absorption in a monolayer graphene sheet by harvesting the electric dipolar mode of split ring resonators. *Opt Lett* **38**, 5410–5413 (2013).
154. Lu H, Cumming BP, Gu M. Highly efficient plasmonic enhancement of graphene absorption at telecommunication wavelengths. *Opt Lett* **40**, 3647–3650 (2015).
155. Lu H, Gan XT, Jia BH, Mao D, Zhao JL. Tunable high-efficiency light absorption of monolayer graphene via Tamm plasmon polaritons. *Opt Lett* **41**, 4743–4746 (2016).
156. Sahoo PK, Pae JY, Murukeshan VM. Enhanced absorption in a graphene embedded 1D guided-mode-resonance structure without back-reflector and interferometrically written gratings. *Opt Lett* **44**, 3661–3664 (2019).
157. Li ZW, Lu H, Li YW, Jiao H, Zhao JL. Near-infrared light absorption enhancement in graphene induced by the Tamm state in optical thin films. *Acta Opt Sin* **39**, 0131001 (2019).
158. Li ZQ, Henriksen EA, Jiang Z, Hao Z, Martin MC et al. Dirac charge dynamics in graphene by infrared spectroscopy. *Nat Phys* **4**, 532–535 (2008).
159. Low T, Avouris P. Graphene plasmonics for terahertz to mid-infrared applications. *ACS Nano* **8**, 1086–1101 (2014).
160. Mak KF, Ju L, Wang F, Heinz TF. Optical spectroscopy of graphene: from the far infrared to the ultraviolet. *Solid State Commun* **152**, 1341–1349 (2012).
161. Jablan M, Buljan H, Soljačić M. Plasmonics in graphene at infrared frequencies. *Phys Rev B* **80**, 245435 (2009).
162. Falkovsky LA, Pershoguba SS. Optical far-infrared properties of a graphene monolayer and multilayer. *Phys Rev B* **76**, 153410 (2007).
163. Chen PY, Alù A. Atomically thin surface cloak using graphene monolayers. *ACS Nano* **5**, 5855–5863 (2011).
164. Gao WL, Shu J, Qiu CY, Xu QF. Excitation of plasmonic waves in graphene by guided-mode resonances. *ACS Nano* **6**, 7806–7813 (2012).
165. Li K, Fitzgerald JM, Xiao XF, Caldwell JD, Zhang C et al. Graphene plasmon cavities made with silicon carbide. *ACS Omega* **2**, 3640–3646 (2017).
166. Wang YL, Li T, Zhu SN. Graphene-based plasmonic modulator on a groove-structured metasurface. *Opt Lett* **42**, 2247–2250 (2017).
167. Fang ZY, Thongrattanasiri S, Schlather A, Liu Z, Ma LL et al. Gated tunability and hybridization of localized plasmons in nanostructured graphene. *ACS Nano* **7**, 2388–2395 (2013).
168. Wang GX, Liu XM, Lu H, Zeng C. Graphene plasmonic lens for manipulating energy flow. *Sci Rep* **4**, 4073 (2014).
169. Christensen J, Manjavacas A, Thongrattanasiri S, Koppens FHL, de Abajo FJG. Graphene plasmon waveguiding and hybridization in individual and paired nanoribbons. *ACS Nano* **6**, 431–440 (2012).
170. Chu HS, How Gan C. Active plasmonic switching at mid-infrared wavelengths with graphene ribbon arrays. *Appl Phys Lett* **102**, 231107 (2013).
171. Low T, Chaves A, Caldwell JD, Kumar A, Fang NX et al. Polaritons in layered two-dimensional materials. *Nat Mater* **16**, 182–194 (2017).
172. Basov DN, Fogler MM, de Abajo FJG. Polaritons in van der Waals materials. *Science* **354**, aag1992 (2016).
173. Dolado I, Alfaro-Mozaz FJ, Li PN, Nikulina E, Bylinkin A et al. Nanoscale guiding of infrared light with hyperbolic volume and surface polaritons in van der Waals material ribbons. *Adv Mater* **32**, 1906530 (2020).
174. Koppens FHL, Chang DE, de Abajo FJG. Graphene plasmonics: a platform for strong light-matter interactions. *Nano Lett* **11**, 3370–3377 (2011).
175. Lyu BS, Li HY, Jiang LL, Shan WF, Hu C et al. Phonon polariton-assisted infrared nanoimaging of local strain in hexagonal boron nitride. *Nano Lett* **19**, 1982–1989 (2019).
176. Liu XZ, Galfsky T, Sun Z, Xia FN, Lin EC et al. Strong light-matter coupling in two-dimensional atomic crystals. *Nat Photonics* **9**, 30–34 (2015).
177. Ju L, Geng BS, Horng J, Girit C, Martin M et al. Graphene plasmonics for tunable terahertz metamaterials. *Nat Nanotechnol* **6**, 630–634 (2011).
178. Han L, Wang L, Xing HZ, Chen XS. Active tuning of midinfrared surface plasmon resonance and its hybridization in black phosphorus sheet array. *ACS Photonics* **5**, 3828–3837 (2018).
179. Lu H, Dai SQ, Yue ZJ, Fan YC, Cheng HC et al. Sb_2Te_3 topological insulator: surface plasmon resonance and application in refractive index monitoring. *Nanoscale* **11**, 4759–4766 (2019).
180. Hu GW, Shen JL, Qiu CW, Alù A, Dai SY. Phonon polaritons and hyperbolic response in van der Waals materials. *Adv Opt Mater* **8**, 1901393 (2020).
181. Zia R, Brongersma ML. Surface plasmon polariton analogue to Young's double-slit experiment. *Nat Nanotechnol* **2**, 426–429 (2007).
182. Barnes WL, Dereux A, Ebbesen TW. Surface plasmon subwavelength optics. *Nature* **424**, 824–830 (2003).
183. Zayats AV, Smolyaninov II, Maradudin AA. Nano-optics of surface plasmon polaritons. *Phys Rep* **408**, 131–314 (2005).
184. Gramotnev DK, Bozhevolnyi SI. Plasmonics beyond the diffraction limit. *Nat Photonics* **4**, 83–91 (2010).
185. Tsakmakidis KL, Boardman AD, Hess O. 'Trapped rainbow' storage of light in metamaterials. *Nature* **450**, 397–401 (2007).
186. Liu N, Langguth L, Weiss T, Kästel J, Fleischhauer M et al. Plasmonic analogue of electromagnetically induced transparency at the Drude damping limit. *Nat Mater* **8**, 758–762 (2009).
187. Lu YJ, Kim J, Chen HY, Wu C, Dabidian N et al. Plasmonic nanolaser using epitaxially grown silver film. *Science* **337**, 450–453 (2012).
188. Meinzer N, Barnes WL, Hooper IR. Plasmonic meta-atoms and metasurfaces. *Nat Photonics* **8**, 889–898 (2014).
189. Luo S, Li Q, Yang YQ, Chen XX, Wang W et al. Controlling fluorescence emission with split-ring-resonator-based plasmonic metasurfaces. *Laser Photon Rev* **11**, 1600299 (2017).
190. Ayata M, Fedoryshyn Y, Heni W, Baeuerle B, Josten A et al. High-speed plasmonic modulator in a single metal layer. *Science* **358**, 630–632 (2017).
191. Zhang JW, Dai SQ, Ma CJ, Di JL, Zhao JL. Compact surface plasmon holographic microscopy for near-field film mapping. *Opt Lett* **42**, 3462–3465 (2017).
192. Luo XG. Plasmonic metalens for nanofabrication. *Natl Sci Rev* **5**, 137–138 (2018).

193. Qiu M, Zhang L, Tang ZX, Jin W, Qiu CW et al. 3D metaphotonic nanostructures with intrinsic chirality. *Adv Funct Mater* **28**, 1803147 (2018).
194. Guo QS, Li C, Deng BC, Yuan SF, Guinea F et al. Infrared nanophotonics based on graphene plasmonics. *ACS Photonics* **4**, 2989–2999 (2017).
195. Guo QS, Yu RW, Li C, Yuan SF, Deng BC et al. Efficient electrical detection of mid-infrared graphene plasmons at room temperature. *Nat Mater* **17**, 986–992 (2018).
196. Li YY, Tantiwanichapan K, Swan AK, Paiella R. Graphene plasmonic devices for terahertz optoelectronics. *Nanophotonics* **9**, 1901–1920 (2020).
197. Lu H, Gan XT, Mao D, Jia BH, Zhao JL. Flexibly tunable high-quality-factor induced transparency in plasmonic systems. *Sci Rep* **8**, 1558 (2018).
198. Lu H, Li YW, Yue ZJ, Mao D, Zhao JL. Graphene-tuned EIT-like effect in photonic multilayers for actively controlled light absorption of topological insulators. *Opt Express* **28**, 31893–31903 (2020).
199. Yan HG, Low T, Zhu WJ, Wu YQ, Freitag M et al. Damping pathways of mid-infrared plasmons in graphene nanostructures. *Nat Photonics* **7**, 394–399 (2013).
200. Naik GV, Shalaev VM, Boltasseva A. Alternative plasmonic materials: beyond gold and silver. *Adv Mater* **25**, 3264–3294 (2013).
201. Lu WB, Zhu W, Xu HJ, Ni ZH, Dong ZG et al. Flexible transformation plasmonics using graphene. *Opt Express* **21**, 10475–10482 (2013).
202. Ooi KJA, Cheng JL, Sipe JE, Ang LK, Tan DTH. Ultrafast, broadband, and configurable midinfrared all-optical switching in nonlinear graphene plasmonic waveguides. *APL Photonics* **1**, 046101 (2016).
203. Zhou W, Lee J, Nanda J, Pantelides ST, Pennycook SJ et al. Atomically localized plasmon enhancement in monolayer graphene. *Nat Nanotechnol* **7**, 161–165 (2012).
204. Li YL, Yan HG, Farmer DB, Meng X, Zhu WJ et al. Graphene plasmon enhanced vibrational sensing of surface-adsorbed layers. *Nano Lett* **14**, 1573–1577 (2014).
205. Alonso-González P, Nikitin AY, Golmar F, Centeno A, Pesquera A et al. Controlling graphene plasmons with resonant metal antennas and spatial conductivity patterns. *Science* **344**, 1369–1373 (2014).
206. Yan HG, Li XS, Chandra B, Tulevski G, Wu YQ et al. Tunable infrared plasmonic devices using graphene/insulator stacks. *Nat Nanotechnol* **7**, 330–334 (2012).
207. Crassee I, Orlita M, Potemski M, Walter AL, Ostler M et al. Intrinsic terahertz plasmons and magnetoplasmons in large scale monolayer graphene. *Nano Lett* **12**, 2470–2474 (2012).
208. Yan HG, Li ZQ, Li XS, Zhu WJ, Avouris P et al. Infrared spectroscopy of tunable dirac terahertz magneto-plasmons in graphene. *Nano Lett* **12**, 3766–3771 (2012).
209. Chen JN, Badioli M, Alonso-González P, Thongrattanasiri S, Huth F et al. Optical nano-imaging of gate-tunable graphene plasmons. *Nature* **487**, 77–81 (2012).
210. Fei Z, Rodin AS, Andreev GO, Bao W, McLeod AS et al. Gate-tuning of graphene plasmons revealed by infrared nano-imaging. *Nature* **487**, 82–85 (2012).
211. Vakil A, Engheta N. Transformation optics using graphene. *Science* **332**, 1291–1294 (2011).
212. Nikitin AY, Guinea F, García-Vidal FJ, Martín-Moreno L. Edge and waveguide terahertz surface plasmon modes in graphene microribbons. *Phys Rev B* **84**, 161407 (2011).
213. Thongrattanasiri S, Koppens FHL, de Abajo FJG. Complete optical absorption in periodically patterned graphene. *Phys Rev Lett* **108**, 047401 (2012).
214. Wang B, Zhang X, Yuan XC, Teng JH. Optical coupling of surface plasmons between graphene sheets. *Appl Phys Lett* **100**, 131111 (2012).
215. Wang B, Zhang X, García-Vidal FJ, Yuan XC, Teng JH. Strong coupling of surface plasmon polaritons in monolayer graphene sheet arrays. *Phys Rev Lett* **109**, 073901 (2012).
216. Auditore A, de Angelis C, Locatelli A, Aceves AB. Tuning of surface plasmon polaritons beat length in graphene directional couplers. *Opt Lett* **38**, 4228–4231 (2013).
217. Ishikawa A, Tanaka T. Plasmon hybridization in graphene metamaterials. *Appl Phys Lett* **102**, 253110 (2013).
218. Forati E, Hanson GW. Surface plasmon polaritons on soft-boundary graphene nanoribbons and their application in switching/demultiplexing. *Appl Phys Lett* **103**, 133104 (2013).
219. Lu H. Plasmonic characteristics in nanoscale graphene resonator-coupled waveguides. *Appl Phys B* **118**, 61–67 (2015).
220. Qiu WB, Liu XH, Zhao J, He SH, Ma YH et al. Nanofocusing of mid-infrared electromagnetic waves on graphene monolayer. *Appl Phys Lett* **104**, 041109 (2014).
221. Jin DF, Kumar A, Hung Fung K, Xu J, Fang NX. Terahertz plasmonics in ferroelectric-gated graphene. *Appl Phys Lett* **102**, 201118 (2013).
222. Lu H, Gan XT, Mao D, Zhao JL. Graphene-supported manipulation of surface plasmon polaritons in metallic nanowaveguides. *Photonics Res* **5**, 162–167 (2017).
223. Lao J, Tao J, Wang QJ, Huang XG. Tunable graphene-based plasmonic waveguides: nano modulators and nano attenuators. *Laser Photon Rev* **8**, 569–574 (2014).
224. Zhu XL, Yan W, Mortensen NA, Xiao SS. Bends and splitters in graphene nanoribbon waveguides. *Opt Express* **21**, 3486–3491 (2013).
225. Nesterov ML, Bravo-Abad J, Nikitin AY, Garcia-Vidal FJ, Martin-Moreno L. Graphene supports the propagation of subwavelength optical solitons. *Laser Photon Rev* **7**, L7–L11 (2013).
226. Balanis CA. *Advanced Engineering Electromagnetics* 2nd ed (*John Wiley & Sons, Inc.*, New York, 2012).
227. Alù A, Engheta N. Optical nanotransmission lines: synthesis of planar left-handed metamaterials in the infrared and visible regimes. *J Opt Soc Am B* **23**, 571–583 (2006).
228. Liu SG, Zhang C, Hu M, Chen XX, Zhang P et al. Coherent and tunable terahertz radiation from graphene surface plasmon polaritons excited by an electron beam. *Appl Phys Lett* **104**, 201104 (2014).
229. Bao YJ, Zu S, Zhang YF, Fang ZY. Active control of graphene-based unidirectional surface plasmon launcher. *ACS Photonics* **2**, 1135–1140 (2015).
230. Lu H, Zhao JL, Gu M. Nanowires-assisted excitation and propagation of mid-infrared surface plasmon polaritons in graphene. *J Appl Phys* **120**, 163106 (2016).
231. Constant TJ, Hornett SM, Chang DE, Hendry E. All-optical generation of surface plasmons in graphene. *Nat Phys* **12**, 124–127 (2016).
232. Miscuglio M, Spirito D, Zaccaria RP, Krahne R. Shape approaches for enhancing plasmon propagation in graphene. *ACS*

Photonics **3**, 2170–2175 (2016).
233. Tao J, Yu XC, Hu B, Dubrovkin A, Wang QJ. Graphene-based tunable plasmonic Bragg reflector with a broad bandwidth. *Opt Lett* **39**, 271–274 (2014).
234. Wang L, Bie ML, Cai W, Zhang XZ, Xu JJ. Graphene plasmonic tamm states with ultracompact footprint. *Phys Rev Appl* **12**, 024057 (2019).
235. Kim JT, Kim J, Choi H, Choi CG, Choi SY. Graphene-based photonic devices for soft hybrid optoelectronic systems. *Nanotechnology* **23**, 344005 (2012).
236. Ooi KJA, Chu HS, Bai P, Ang LK. Electro-optical graphene plasmonic logic gates. *Opt Lett* **39**, 1629–1632 (2014).
237. Iizuka H, Fan SH. Deep subwavelength plasmonic waveguide switch in double graphene layer structure. *Appl Phys Lett* **103**, 233107 (2013).
238. He MD, Wang KJ, Wang L, Li JB, Liu JQ et al. Graphene-based terahertz tunable plasmonic directional coupler. *Appl Phys Lett* **105**, 081903 (2014).
239. Bandurin DA, Svintsov D, Gayduchenko I, Xu SG, Principi A et al. Resonant terahertz detection using graphene plasmons. *Nat Commun* **9**, 5392 (2018).
240. Curto AG, Rivas JG. Confining light to the atomic scale. *Nat Nanotechnol* **13**, 442–443 (2018).
241. Song JCW. Plasmon propagation pushed to the limit. *Nature* **557**, 501–502 (2018).
242. Morozov MY, Davoyan AR, Moiseenko IM, Satou A, Otsuji T et al. Active guiding of Dirac plasmons in graphene. *Appl Phys Lett* **106**, 061105 (2015).
243. Ni GX, Wang L, Goldflam MD, Wagner M, Fei Z et al. Ultrafast optical switching of infrared plasmon polaritons in high-mobility graphene. *Nat Photonics* **10**, 244–247 (2016).
244. Ding Y, Guan X, Zhu X, Hu H, Bozhevolnyi SI et al. Efficient electro-optic modulation in low-loss graphene-plasmonic slot waveguides. *Nanoscale* **9**, 15576–15581 (2017).
245. Woessner A, Gao YD, Torre I, Lundeberg MB, Tan C et al. Electrical 2π phase control of infrared light in a 350-nm footprint using graphene plasmons. *Nat Photonics* **11**, 421–424 (2017).
246. Leavitt RP, Little JW. Absorption and emission of radiation by plasmons in two-dimensional electron-gas disks. *Phys Rev B* **34**, 2450–2457 (1986).
247. Stauber T, Peres NMR, Geim AK. Optical conductivity of graphene in the visible region of the spectrum. *Phys Rev B* **78**, 085432 (2008).
248. Zeng C, Guo J, Liu XM. High-contrast electro-optic modulation of spatial light induced by graphene-integrated Fabry-Pérot microcavity. *Appl Phys Lett* **105**, 121103 (2014).
249. Deng BC, Guo QS, Li C, Wang HZ, Ling X et al. Coupling-enhanced broadband mid-infrared light absorption in graphene plasmonic nanostructures. *ACS Nano* **10**, 11172–11178 (2016).
250. Fang ZY, Wang YM, Schlather AE, Liu Z, Ajayan PM et al. Active tunable absorption enhancement with graphene nanodisk arrays. *Nano Lett* **14**, 299–304 (2014).
251. Silveiro I, de Abajo FJG. Plasmons in inhomogeneously doped neutral and charged graphene nanodisks. *Appl Phys Lett* **104**, 131103 (2014).
252. Tang WW, Wang L, Chen XS, Liu CL, Yu AQ et al. Dynamic metamaterial based on the graphene split ring high-Q Fano-resonnator for sensing applications. *Nanoscale* **8**, 15196–15204 (2016).
253. Papasimakis N, Thongrattanasiri S, Zheludev NI, de Abajo FJG. The magnetic response of graphene split-ring metamaterials. *Light Sci Appl* **2**, e78 (2013).
254. Tamagnone M, Gómez-Díaz JS, Mosig JR, Perruisseau-Carrier J. Reconfigurable terahertz plasmonic antenna concept using a graphene stack. *Appl Phys Lett* **101**, 214102 (2012).
255. Brar VW, Jang MS, Sherrott M, Lopez JJ, Atwater HA. Highly confined tunable mid-infrared plasmonics in graphene nanoresonators. *Nano Lett* **13**, 2541–2547 (2013).
256. Rodrigo D, Tittl A, Limaj O, de Abajo FJG, Pruneri V et al. Double-layer graphene for enhanced tunable infrared plasmonics. *Light Sci Appl* **6**, e16277 (2017).
257. Zhang N, Jiang XJ, Fan J, Luo WW, Xiang YX et al. Experimental observed plasmon near-field response in isolated suspended graphene resonators. *Nanotechnology* **30**, 505201 (2019).
258. Xiong W, Zhou YS, Hou WJ, Jiang LJ, Gao Y et al. Direct writing of graphene patterns on insulating substrates under ambient conditions. *Sci Rep* **4**, 4892 (2014).
259. Zhang K, Zhang L, Yap FL, Song P, Qiu CW et al. Large-area graphene nanodot array for plasmon-enhanced infrared spectroscopy. *Small* **12**, 1302–1308 (2016).
260. Lin H, Sturmberg BCP, Lin KT, Yang YY, Zheng XR et al. A 90-nm-thick graphene metamaterial for strong and extremely broadband absorption of unpolarized light. *Nat Photonics* **13**, 270–276 (2019).
261. Takamura M, Kumada N, Wang SN, Kumakura K, Taniyasu Y. Plasmon control driven by spatial carrier density modulation in graphene. *ACS Photonics* **6**, 947–952 (2019).
262. Vakil A, Engheta N. Fourier optics on graphene. *Phys Rev B* **85**, 075434 (2012).
263. Zeng C, Liu XM, Wang GX. Electrically tunable graphene plasmonic quasicrystal metasurfaces for transformation optics. *Sci Rep* **4**, 5763 (2014).
264. Huidobro PA, Kraft M, Maier SA, Pendry JB. Graphene as a tunable anisotropic or isotropic plasmonic metasurface. *ACS Nano* **10**, 5499–5506 (2016).
265. Liu PH, Cai W, Wang L, Zhang XZ, Xu JJ. Tunable terahertz optical antennas based on graphene ring structures. *Appl Phys Lett* **100**, 153111 (2012).
266. Li ZC, Liu WW, Cheng H, Chen SQ, Tian JG. Tunable dual-band asymmetric transmission for circularly polarized waves with graphene planar chiral metasurfaces. *Opt Lett* **41**, 3142–3145 (2016).
267. Gopalan KK, Paulillo B, Mackenzie DMA, Rodrigo D, Bareza N et al. Scalable and tunable periodic graphene nanohole arrays for mid-infrared plasmonics. *Nano Lett* **18**, 5913–5918 (2018).
268. Galiffi E, Pendry JB, Huidobro PA. Broadband tunable THz absorption with singular graphene metasurfaces. *ACS Nano* **12**, 1006–1013 (2018).
269. Alaee R, Farhat M, Rockstuhl C, Lederer F. A perfect absorber made of a graphene micro-ribbon metamaterial. *Opt Express* **20**, 28017–28024 (2012).
270. Li G, Semenenko V, Perebeinos V, Liu PQ. Multilayer graphene terahertz plasmonic structures for enhanced frequency tuning range. *ACS Photonics* **6**, 3180–3185 (2019).
271. Hu H, Yang XX, Zhai F, Hu DB, Liu RN et al. Far-field nanoscale infrared spectroscopy of vibrational fingerprints of molecules with graphene plasmons. *Nat Commun* **7**, 12334 (2016).
272. Rodrigo D, Limaj O, Janner D, Etezadi D, de Abajo FJG et al.

Mid-infrared plasmonic biosensing with graphene. *Science* **349**, 165–168 (2015).
273. Zundel L, Manjavacas A. Spatially resolved optical sensing using graphene nanodisk arrays. *ACS Photonics* **4**, 1831–1838 (2017).
274. Bareza N Jr, Gopalan KK, Alani R, Paulillo B, Pruneri V. Mid-infrared gas sensing using graphene plasmons tuned by reversible chemical doping. *ACS Photonics* **7**, 879–884 (2020).
275. Hu H, Yang XX, Guo XD, Khaliji K, Biswas SR et al. Gas identification with graphene plasmons. *Nat Commun* **10**, 1131 (2019).
276. Shi X, Han DZ, Dai YY, Yu ZF, Sun Y et al. Plasmonic analog of electromagnetically induced transparency in nanostructure graphene. *Opt Express* **21**, 28438–28443 (2013).
277. Thongrattanasiri S, de Abajo FJG. Optical field enhancement by strong plasmon interaction in graphene nanostructures. *Phys Rev Lett* **110**, 187401 (2013).
278. Cheng H, Chen SQ, Yu P, Duan XY, Xie BY et al. Dynamically tunable plasmonically induced transparency in periodically patterned graphene nanostrips. *Appl Phys Lett* **103**, 203112 (2013).
279. Zeng C, Cui YD, Liu XM. Tunable multiple phase-coupled plasmon-induced transparencies in graphene metamaterials. *Opt Express* **23**, 545–551 (2015).
280. Lu H, Mao D, Zeng C, Xiao FJ, Yang DX et al. Plasmonic Fano spectral response from graphene metasurfaces in the MIR region. *Opt Mater Express* **8**, 1058–1068 (2018).
281. He XJ, Zhang QF, Lu GJ, Ying GB, Wu FM et al. Tunable ultrasensitive terahertz sensor based on complementary graphene metamaterials. *RSC Adv* **6**, 52212–52218 (2016).
282. Cui YD, Zeng C. Efficient modulation of orthogonally polarized infrared light using graphene metamaterials. *J Appl Phys* **121**, 143102 (2017).
283. Zhao XL, Yuan C, Zhu L, Yao JQ. Graphene-based tunable terahertz plasmon-induced transparency metamaterial. *Nanoscale* **8**, 15273–15280 (2016).
284. He XY, Liu F, Lin FT, Shi WZ. Graphene patterns supported terahertz tunable plasmon induced transparency. *Opt Express* **26**, 9931–9944 (2018).
285. Lu FF, Liu BA, Shen S. Infrared wavefront control based on graphene metasurfaces. *Adv Opt Mater* **2**, 794–799 (2014).
286. Li ZB, Yao K, Xia FN, Shen S, Tian JG et al. Graphene plasmonic metasurfaces to steer infrared light. *Sci Rep* **5**, 12423 (2015).
287. Yatooshi T, Ishikawa A, Tsuruta K. Terahertz wavefront control by tunable metasurface made of graphene ribbons. *Appl Phys Lett* **107**, 053105 (2015).
288. Ma W, Huang Z, Bai XK, Zhan P, Liu YM. Dual-band light focusing using stacked graphene metasurfaces. *ACS Photonics* **4**, 1770–1775 (2017).
289. Biswas SR, Gutiérrez CE, Nemilentsau A, Lee IH, Oh SH et al. Tunable graphene metasurface reflectarray for cloaking, illusion, and focusing. *Phys Rev Appl* **9**, 034021 (2018).
290. Zhu H, Deng M, Chen SQ, Chen L. Graphene-based metacoupler for direction-controllable emission of surface plasmons. *Opt Lett* **44**, 3382–3385 (2019).
291. Chen HT, Taylor AJ, Yu NF. A review of metasurfaces: physics and applications. *Rep Prog Phys* **79**, 076401 (2016).
292. Bomzon Z, Biener G, Kleiner V, Hasman E. Space-variant Pancharatnam-Berry phase optical elements with computer-generated subwavelength gratings. *Opt Lett* **27**, 1141–1143 (2002).
293. Bai XX, Tang LL, Yao W, Zang Q, Lu JL et al. High efficiency active wavefront manipulation of spin photonics based on a graphene metasurface. *Opt Express* **27**, 22475–22484 (2019).
294. Crassee I, Levallois J, Walter AL, Ostler M, Bostwick A et al. Giant Faraday rotation in single- and multilayer graphene. *Nat Phys* **7**, 48–51 (2011).
295. Fallahi A, Perruisseau-Carrier J. Manipulation of giant Faraday rotation in graphene metasurfaces. *Appl Phys Lett* **101**, 231605 (2012).
296. Tymchenko M, Nikitin AY, Martín-Moreno L. Faraday Rotation Due to Excitation of Magnetoplasmons in Graphene Microribbons. *ACS Nano* **7**, 9780–9787 (2013).
297. Hadad Y, Davoyan AR, Engheta N, Steinberg BZ. Extreme and quantized magneto-optics with graphene meta-atoms and metasurfaces. *ACS Photonics* **1**, 1068–1073 (2014).
298. Tamagnone M, Slipchenko TM, Moldovan C, Liu PQ, Centeno A et al. Magnetoplasmonic enhancement of Faraday rotation in patterned graphene metasurfaces. *Phys Rev B* **97**, 241410 (2018).
299. Padmanabhan P, Boubanga-Tombet S, Fukidome H, Otsuji T, Prasankumar RP. A graphene-based magnetoplasmonic metasurface for actively tunable transmission and polarization rotation at terahertz frequencies. *Appl Phys Lett* **116**, 221107 (2020).
300. Cheng H, Chen SQ, Yu P, Li JX, Deng L et al. Mid-infrared tunable optical polarization converter composed of asymmetric graphene nanocrosses. *Opt Lett* **38**, 1567–1569 (2013).
301. Cheng H, Chen SQ, Yu P, Li JX, Xie BY et al. Dynamically tunable broadband mid-infrared cross polarization converter based on graphene metamaterial. *Appl Phys Lett* **103**, 223102 (2013).
302. Guo TJ, Argyropoulos C. Broadband polarizers based on graphene metasurfaces. *Opt Lett* **41**, 5592–5595 (2016).
303. Polischuk OV, Melnikova VS, Popov VV. Giant cross-polarization conversion of terahertz radiation by plasmons in an active graphene metasurface. *Appl Phys Lett* **109**, 131101 (2016).
304. You JW, Panoiu NC. Polarization control using passive and active crossed graphene gratings. *Opt Express* **26**, 1882–1894 (2018).
305. Cox JD, de Abajo FJG. Electrically tunable nonlinear plasmonics in graphene nanoislands. *Nat Commun* **5**, 5725 (2014).
306. Kundys D, Van Duppen B, Marshall OP, Rodriguez F, Torre I et al. Nonlinear light mixing by graphene plasmons. *Nano Lett* **18**, 282–287 (2018).
307. Cox JD, de Abajo FJG. Nonlinear graphene nanoplasmonics. *Acc Chem Res* **52**, 2536–2547 (2019).
308. Cox JD, Marini A, de Abajo FJG. Plasmon-assisted high-harmonic generation in graphene. *Nat Commun* **8**, 14380 (2017).
309. Cox JD, de Abajo FJG. Plasmon-enhanced nonlinear wave mixing in nanostructured graphene. *ACS Photonics* **2**, 306–312 (2015).
310. Cheng JR, Wang WL, Mosallaei H, Kaxiras E. Surface plasmon engineering in graphene functionalized with organic molecules: a multiscale theoretical investigation. *Nano Lett* **14**, 50–56 (2014).
311. Gómez-Díaz JS, Perruisseau-Carrier J. Graphene-based plasmonic switches at near infrared frequencies. *Opt Express* **21**, 15490–15504 (2013).
312. Lu H, Zeng C, Zhang QM, Liu XN, Hossain M et al. Graphene-based active slow surface plasmon polaritons. *Sci Rep* **5**, 8443 (2015).

313. Shi B, Cai W, Zhang XZ, Xiang YX, Zhan Y et al. Tunable band-stop filters for graphene plasmons based on periodically modulated graphene. *Sci Rep* **6**, 26796 (2016).
314. Xiong L, Forsythe C, Jung M, McLeod AS, Sunku SS et al. Photonic crystal for graphene plasmons. *Nat Commun* **10**, 4780 (2019).
315. You JW, Lan ZH, Bao QL, Panoiu NC. Valley-hall topological plasmons in a graphene nanohole plasmonic crystal waveguide. *IEEE J Sel Top Quantum Electron* **26**, 4600308 (2020).
316. Emani NK, Chung TF, Ni XJ, Kildishev AV, Chen YP et al. Electrically tunable damping of plasmonic resonances with graphene. *Nano Lett* **12**, 5202–5206 (2012).
317. Yao Y, Kats MA, Genevet P, Yu NF, Song Y et al. Broad electrical tuning of graphene-loaded plasmonic antennas. *Nano Lett* **13**, 1257–1264 (2013).
318. Smirnova DA, Miroshnichenko AE, Kivshar YS, Khanikaev AB. Tunable nonlinear graphene metasurfaces. *Phys Rev B* **92**, 161406 (2015).
319. Shi SF, Zeng B, Han HL, Hong X, Tsai HZ et al. Optimizing broadband terahertz modulation with hybrid graphene/metasurface structures. *Nano Lett* **15**, 372–377 (2015).
320. Li ZY, Yu NF. Modulation of mid-infrared light using graphene-metal plasmonic antennas. *Appl Phys Lett* **102**, 131108 (2013).
321. Liang GZ, Hu XN, Yu XC, Shen YD, Li LH et al. Integrated terahertz graphene modulator with 100% modulation depth. *ACS Photonics* **2**, 1559–1566 (2015).
322. Gao WL, Shu J, Reichel K, Nickel DV, He XW et al. High-contrast terahertz wave modulation by gated graphene enhanced by extraordinary transmission through ring apertures. *Nano Lett* **14**, 1242–1248 (2014).
323. Yao Y, Kats MA, Shankar R, Song Y, Kong J et al. Wide wavelength tuning of optical antennas on graphene with nanosecond response time. *Nano Lett* **14**, 214–219 (2014).
324. Degl'Innocenti R, Jessop DS, Shah YD, Sibik J, Zeitler JA et al. Low-bias terahertz amplitude modulator based on split-ring resonators and graphene. *ACS Nano* **8**, 2548–2554 (2014).
325. Degl'Innocenti R, Jessop DS, Sol CWO, Xiao L, Kindness SJ et al. Fast modulation of terahertz quantum cascade lasers using graphene loaded plasmonic antennas. *ACS Photonics* **3**, 464–470 (2016).
326. Emani NK, Kildishev AV, Shalaev VM, Boltasseva A. Graphene: a dynamic platform for electrical control of plasmonic resonance. *Nanophotonics* **4**, 214–223 (2015).
327. Gan XT, Shiue RJ, Gao YD, Mak KF, Yao XW et al. High-contrast electrooptic modulation of a photonic crystal nanocavity by electrical gating of graphene. *Nano Lett* **13**, 691–696 (2013).
328. Jung H, Jo H, Lee W, Kim B, Choi H et al. Electrical control of electromagnetically induced transparency by terahertz metamaterial funneling. *Adv Opt Mater* **7**, 1801205 (2019).
329. Zhu YB, Li ZY, Hao Z, Dimarco C, Maturavongsadit P et al. Optical conductivity-based ultrasensitive mid-infrared biosensing on a hybrid metasurface. *Light Sci Appl* **7**, 67 (2018).
330. Zhang J, Wei XZ, Rukhlenko ID, Chen HT, Zhu WR. Electrically tunable metasurface with independent frequency and amplitude modulations. *ACS Photonics* **7**, 265–271 (2020).
331. Chen XY, Tian Z, Lu YC, Xu YH, Zhang XQ et al. Electrically tunable perfect terahertz absorber based on a graphene salisbury screen hybrid metasurface. *Adv Opt Mater* **8**, 1900660 (2020).
332. Emani NK, Chung TF, Kildishev AV, Shalaev VM, Chen YP et al. Electrical modulation of Fano resonance in plasmonic nanostructures using graphene. *Nano Lett* **14**, 78–82 (2014).
333. Mousavi SH, Kholmanov I, Alici KB, Purtseladze D, Arju N et al. Inductive tuning of Fano-resonant metasurfaces using plasmonic response of graphene in the mid-infrared. *Nano Lett* **13**, 1111–1117 (2013).
334. Dabidian N, Kholmanov I, Khanikaev AB, Tatar K, Trendafilov S et al. Electrical switching of infrared light using graphene integration with plasmonic Fano resonant metasurfaces. *ACS Photonics* **2**, 216–227 (2015).
335. Kim TT, Kim HD, Zhao RK, Oh SS, Ha T et al. Electrically tunable slow light using graphene metamaterials. *ACS Photonics* **5**, 1800–1807 (2018).
336. Li Q, Cong LQ, Singh R, Xu NN, Cao W et al. Monolayer graphene sensing enabled by the strong Fano-resonant metasurface. *Nanoscale* **8**, 17278–17284 (2016).
337. Zeng BB, Huang ZQ, Singh A, Yao Y, Azad AK et al. Hybrid graphene metasurfaces for high-speed mid-infrared light modulation and single-pixel imaging. *Light Sci Appl* **7**, 51 (2018).
338. Miao ZQ, Wu Q, Li X, He Q, Ding K et al. Widely tunable terahertz phase modulation with gate-controlled graphene metasurfaces. *Phys Rev X* **5**, 041027 (2015).
339. Dabidian N, Dutta-Gupta S, Kholmanov I, Lai KF, Lu F et al. Experimental demonstration of phase modulation and motion sensing using graphene-integrated metasurfaces. *Nano Lett* **16**, 3607–3615 (2016).
340. Sherrott MC, Hon PWC, Fountaine KT, Garcia JC, Ponti SM et al. Experimental demonstration of >230° phase modulation in gate-tunable graphene-gold reconfigurable mid-infrared metasurfaces. *Nano Lett* **17**, 3027–3034 (2017).
341. Zhou JX, Liu YC, Ke YG, Luo HL, Wen SC. Generation of Airy vortex and Airy vector beams based on the modulation of dynamic and geometric phases. *Opt Lett* **40**, 3193–3196 (2015).
342. Khorasaninejad M, Capasso F. Metalenses: versatile multifunctional photonic components. *Science* **358**, eaam8100 (2017).
343. Kim TT, Kim H, Kenney M, Park HS, Kim HD et al. Amplitude modulation of anomalously refracted terahertz waves with gated-graphene metasurfaces. *Adv Opt Mater* **6**, 1700507 (2018).
344. Liu WG, Hu B, Huang ZD, Guan HY, Li HT et al. Graphene-enabled electrically controlled terahertz meta-lens. *Photonics Res* **6**, 703–708 (2018).
345. Jung M, Dutta-Gupta S, Dabidian N, Brener I, Shcherbakov M et al. Polarimetry using graphene-integrated anisotropic metasurfaces. *ACS Photonics* **5**, 4283–4288 (2018).
346. Kindness SJ, Almond NW, Michailow W, Wei BB, Jakob LA et al. Graphene-integrated metamaterial device for all-electrical polarization control of terahertz quantum cascade lasers. *ACS Photonics* **6**, 1547–1555 (2019).
347. Guan SN, Cheng J, Chen TH, Chang SJ. Bi-functional polarization conversion in hybrid graphene-dielectric metasurfaces. *Opt Lett* **44**, 5683–5686 (2019).
348. Li JX, Yu P, Cheng H, Liu WW, Li ZC et al. Optical polarization encoding using graphene-loaded plasmonic metasurfaces. *Adv Opt Mater* **4**, 91–98 (2016).
349. Kim TT, Oh SS, Kim HD, Park HS, Hess O et al. Electrical access to critical coupling of circularly polarized waves in graphene chiral metamaterials. *Sci Adv* **3**, e1701377 (2017).
350. Cui TJ, Qi MQ, Wan X, Zhao J, Cheng Q. Coding metamaterials, digital metamaterials and programmable metamaterials.

Light Sci Appl **3**, e218 (2014).
351. Wan X, Qi MQ, Chen TY, Cui TJ. Field-programmable beam reconfiguring based on digitally-controlled coding metasurface. *Sci Rep* **6**, 20663 (2016).
352. Li LL, Shuang Y, Ma Q, Li HY, Zhao HT et al. Intelligent metasurface imager and recognizer. *Light Sci Appl* **8**, 97 (2019).
353. Chen H, Lu WB, Liu ZG, Geng MY. Microwave programmable graphene metasurface. *ACS Photonics* **7**, 1425–1435 (2020).
354. Zhang J, Zhang H, Yang WX, Chen K, Wei XZ et al. Dynamic scattering steering with graphene-based coding metamirror. *Adv Opt Mater* **8**, 2000683 (2020).
355. Yao K, Unni R, Zheng YB. Intelligent nanophotonics: merging photonics and artificial intelligence at the nanoscale. *Nanophotonics* **8**, 339–366 (2019).
356. Chen YS, Zhu JF, Xie YN, Feng NX, Liu QH. Smart inverse design of graphene-based photonic metamaterials by an adaptive artificial neural network. *Nanoscale* **11**, 9749–9755 (2019).
357. Liu ZB, Li L, Xu YF, Liang JJ, Zhao X et al. Direct patterning on reduced graphene oxide nanosheets using femtosecond laser pulses. *J Opt* **13**, 085601 (2011).
358. Zou TT, Zhao B, Xin W, Wang Y, Wang B et al. High-speed femtosecond laser plasmonic lithography and reduction of graphene oxide for anisotropic photoresponse. *Light Sci Appl* **9**, 69 (2020).
359. Yang YY, Lin H, Zhang BY, Zhang YN, Zheng XR et al. Graphene-based multilayered metamaterials with phototunable architecture for on-chip photonic devices. *ACS Photonics* **6**, 1033–1040 (2019).
360. Wu JY, Jia LN, Zhang YN, Qu Y, Jia BH et al. Graphene oxide for integrated photonics and flat optics. *Adv Mater* **33**, 2006415 (2021).
361. Zheng XR, Jia BH, Lin H, Qiu L, Li D et al. Highly efficient and ultra-broadband graphene oxide ultrathin lenses with three-dimensional subwavelength focusing. *Nat Commun* **6**, 8433 (2015).
362. Zhou N, Zheng S, Cao XP, Zhao YF, Gao SQ et al. Ultra-compact broadband polarization diversity orbital angular momentum generator with 3.6 x 3.6 μm^2 footprint. *Sci Adv* **5**, eaau9593 (2019).
363. Wang Z, Li TT, Soman A, Mao D, Kananen T et al. On-chip wavefront shaping with dielectric metasurface. *Nat Commun* **10**, 3547 (2019).
364. Zhang YB, Li ZC, Liu WW, Li Z, Cheng H et al. Spin-selective and wavelength-selective demultiplexing based on waveguide-integrated all-dielectric metasurfaces. *Adv Opt Mater* **7**, 1801273 (2019).
365. Shcherbakov MR, Lemasters R, Fan ZY, Song J, Lian TQ et al. Time-variant metasurfaces enable tunable spectral bands of negative extinction. *Optica* **6**, 1441–1442 (2019).
366. Ono M, Hata M, Tsunekawa M, Nozaki K, Sumikura H et al. Ultrafast and energy-efficient all-optical switching with graphene-loaded deep-subwavelength plasmonic waveguides. *Nat Photonics* **14**, 37–43 (2020).
367. Peng RM, Khaliji K, Youngblood N, Grassi R, Low T et al. Midinfrared electro-optic modulation in few-layer black phosphorus. *Nano Lett* **17**, 6315–6320 (2017).
368. Arezoomandan S, Gopalan P, Tian K, Chanana A, Nahata A et al. Tunable terahertz metamaterials employing layered 2-D materials beyond graphene. *IEEE J Sel Top Quantum Electron* **23**, 8500307 (2017).
369. Tan C, Yue ZJ, Dai ZG, Bao QL, Wang XL et al. Nanograting-assisted generation of surface plasmon polaritons in Weyl semimetal WTe_2. *Opt Mater* **86**, 421–423 (2018).
370. Jha PK, Shitrit N, Ren XX, Wang Y, Zhang X. Spontaneous exciton valley coherence in transition metal dichalcogenide monolayers interfaced with an anisotropic metasurface. *Phys Rev Lett* **121**, 116102 (2018).
371. Yuan QC, Fang L, Fang HL, Li JT, Wang T et al. Second harmonic and sum-frequency generations from a silicon metasurface integrated with a two-dimensional material. *ACS Photonics* **6**, 2252–2259 (2019).
372. Lu H, Yue ZJ, Li YW, Zhang YA, Zhang MW et al. Magnetic plasmon resonances in nanostructured topological insulators for strongly enhanced light-MoS_2 interactions. *Light Sci Appl* **9**, 191 (2020).
373. Wen T, Zhang WD, Liu S, Hu AQ, Zhao JY et al. Steering valley-polarized emission of monolayer MoS2 sandwiched in plasmonic antennas. *Sci Adv* **6**, eaao0019 (2020).
374. Busschaert S, Flöry N, Papadopoulos S, Parzefall M, Heeg S et al. Beam steering with a nonlinear optical phased array antenna. *Nano Lett* **19**, 6097–6103 (2019).
375. Chen JW, Wang K, Long H, Han XB, Hu HB et al. Tungsten disulfide-gold nanohole hybrid metasurfaces for nonlinear metalenses in the visible region. *Nano Lett* **18**, 1344–1350 (2018).
376. Hu GW, Hong XM, Wang K, Wu J, Xu HX et al. Coherent steering of nonlinear chiral valley photons with a synthetic Au–WS_2 metasurface. *Nat Photonics* **13**, 467–472 (2019).
377. Hong XM, Hu GW, Zhao WC, Wang K, Sun S et al. Structuring nonlinear wavefront emitted from monolayer transition-metal dichalcogenides. *Research* **2020**, 9085782 (2020).
378. Spreyer F, Zhao RZ, Huang LL, Zentgraf T. Second harmonic imaging of plasmonic Pancharatnam-Berry phase metasurfaces coupled to monolayers of WS_2. *Nanophotonics* **9**, 351–360 (2020).

Acknowledgements

This work was supported by the National Key R&D Program of China (2017YFA0303800), the National Natural Science Foundation of China (61805277, 11634010, 91950207, 11974283, 11774290), the Fundamental Research Funds for the Central Universities (3102017AX009, 3102019PY002, 3102019JC008), and the Natural Science Basic Research Program of Shaanxi (2019JQ-447, 2020JM-130).

Competing interests

The authors declare no competing financial interests.